Dynamics of vibrated granular matter

by

Rohit Ajit Ingale

A Dissertation Submitted to the Graduate Faculty in Engineering in Partial Fulfillment of the Requirements for the Degree of Doctor of Philosophy

The City University of New York

2008

This manuscript has been read and accepted for the Graduate Faculty in Engineering in satisfaction of the dissertation requirement for the degree of Doctor of Philosophy.

Date	Prof. Mark Shattuck Chairman of Examining Committee
Date	Prof. Mumtaz Kassir Executive Officer

Prof. Mark Shattuck (Mentor)

Prof. Alexander Couzis

Prof. Jeffrey Morris

Prof. Hernan Makse

Prof. M. Lane Gilchrist

Supervisory Committee

THE CITY UNIVERSITY OF NEW YORK

Abstract

Dynamics of Vibrated Granular Matter

by

Rohit A. Ingale

Advisor: Prof. Mark Shattuck

We present novel experimental investigation of solid-fluid phase transition in a non-equilibrium system; a vertically vibrated quasi-2D granular fluid under isobaric and isochoric conditions. Under constant pressure (isobaric) conditions, a steady state transitions occur between a gas like phase and a crystalline phase as a function of the driving acceleration. The phase transition is first-order, characterized by a discontinuous change in both density and temperature. It shows rate dependent hysteresis. For constant volume (isochoric) conditions, we investigate the structural changes in the crystallization of a uniformly heated quasi-2D granular fluid, as a function of filling fraction. Our experimental results for quantitative characterization of the structural and topological changes at the particle level are nearly identical to those found in simulations of equilibrium hard disks. This direct mapping suggests that the study of equilibrium systems can be effectively applied to study homogeneous non-equilibrium steady states like those found in our driven and dissipative granular system. We further investigate the application and relevance of geometrical mechanisms for explaining solid-fluid phase transition in the isochoric geometry. We also measure the steady state velocity distribution for the uniformly heated case and quantify the deviations from the equilibrium Maxwell-Boltzmann distribution. In general, the results of our experimental study provide a much deeper understanding of the specifics of phase transition in granular fluids.

Preface

The study of granular matter has received a recent upsurge of interest in physics. This has been motivated by both the relevance of granular flows to a wide range of industrial and geological processes, and by the realization that granular materials provide an excellent test bed for a number of fundamental questions in the context of modern fluid dynamics and nonequilibrium statistical mechanics.

Granular media are ensembles of macroscopic, discrete solid particles, or grains. Granular materials are intrinsically dissipative in nature due to inelastic particle collisions and frictional contacts. Hence, any dynamical study of granular media requires energy injection through vibration, shear etc. The research work described in this thesis primarily comprises experimentally investigating dynamics of granular media, which are set into motion by external vibrations. Specifically we study phase transition behavior in granular materials under various experimental conditions. Current theories of granular media can explain fluidlike (gas or liquid) or solidlike behavior but cannot take into account the phase transition between the two states. Therefore, we focus on the solid-fluid phase transitions in vibrated granular materials and develop novel methodologies for quantifying the dynamics and structure in granular fluids. We also conduct experiments to directly test some of the predictions of granular kinetic theory, which is used to develop continuum models for granular flows.

This thesis is organized into six chapters: Chapter 1 provides an introduction to the fundamental properties of granular media and their relevance to industrial application and geological processes. We then present a brief overview of the dynamical behavior in granular media. Further, we focus on vibrated granular media, review previous investigations, and illustrate the important phase transition aspects

of vibrated granular matter.

In Chapter 2, we report experimental investigations of an isobaric granular system. A detailed descriptions of the experimental apparatus and technique is provided in the initial sections of Chapter 2. We then follow it up with sections illustrating the results of our investigation like the nature of the solid-fluid phase transition and it's characteristics. We also discuss the effect of various experimental parameters like driving frequency, number of particles, pressure etc., on the phase transition. At the end of Chapter 2, we summarize the main findings and discuss important issues related to the observed phase transition.

In Chapter 3, we experimentally investigate a uniformly heated quasi-2D granular fluid under constant volume (isochoric) conditions. We begin by describing the experimental apparatus and then specify the experimental parameters and procedure in detail in a later section. We then present the results of the crystallization transition using standard measures like Lindemann criterion, radial distribution function and bond-order parameter. The concept of shape factor is then introduced to quantify the phase transition followed by detailed discussion on the structural changes in the granular fluid. We also compare our experimental results with the simulation results of equilibrium hard disk systems. We then summarize the main results towards the end of the chapter.

In Chapter 4, we report a novel geometrical mechanism for solid-fluid phase transition in a uniformly heated quasi-2D granular system. In particular, we refer to the bond-order parameter, the bond length and bond angle distribution to identify the underlying topology of the granular fluid. The packing constraints in our quasi-2D granular fluid give rise to a geometrical structure resembling plane tilings composed of closed packed squares and triangles (ST Tilings). We further compare the experimental results with the theoretical predictions of the ST tiling model.

In Chapter 5, we present experimental results on the velocity statistics of a

granular fluid in a uniformly heated isochoric configurations. We measure the steady state velocity distribution as a function of various experimental parameters. We then quantify the deviation of the velocity distributions from equilibrium behavior. We then summarize the main findings from this chapter. Finally, conclusions arising from the overall study are made in Chapter 6. We establish connections between the main results from each Chapter and make final concluding remarks to complete the entire picture. We also present specific thoughts for future work towards the end of Chapter 6.

Acknowledgments

First and foremost, I would like to thank my advisor Prof. Mark Shattuck for his unflinching support and guidance throughout my PhD research work. He has been an excellent mentor and above all a good friend. I immensely enjoyed working with him and feel very fortunate to have him as my PhD advisor. I truly believe that he is the best mentor that any student could ever ask for.

Next, I would like to thank my PhD committee members Prof. Hernan Makse, Prof. Alexander Couzis, Prof. Jeffrey Morris and Prof. Lane Gilchrist for providing me valuable suggestions and feedback during the duration of my PhD. A special thanks goes to my research group colleague Dr. Pedro Reis for his generous assistance in my research activities and motivating me to do the best. I would also like to thank Prof. Morton Denn for all his help and advice during my stay at the Levich. He has been an inspirational figure and role model for me.

I thank my lab colleagues: Diego, Chris, Ping Wang, Hernan R, Chaoming, Shomeek, Kun Wang for their enthusiasm, support and motivation during my PhD. I big thank you goes to my huge group of Indian friends at CCNY: Anil Kumar, Nikhil K, Shyam, John, Manoj, Amar, Pandurang, Sandeep, Vikas, Prasad K/Y, Shripad, Nikhil B, Vilobh, Swapnil, Rajesh, Pradeep and many more, for making my life exciting and fun filled during the course of my four and half year stay at CCNY.

Finally, I would like to dedicate this thesis to my parents, Mr. Ajit Ingale and Mrs. Jayashree Ingale. It is the result of their enduring and continuous efforts, love and support that I have been able to undertake this task and do justice to it. They gave me the freedom to choose my career path and always encouraged me to achieve higher and higher goals in life.

Contents

List of Figures

Chapter 1

Introduction

1.1 Why Study Granular Matter?

Granular materials, i.e. ensembles of macroscopic discrete particles, are ubiquitous in our every day life, nature, and of crucial importance in industrial processes (Jaeger & Nagel 1992, Jaeger, Nagel & Behringer 1996). Examples of such materials include sand, gravel, grains, powders, pharmaceutical pills, and a variety of chemicals. Many industrial practices require efficient handling, processing and mixing of granular materials: food and agricultural industry, chemical industry, cement manufacturing, and the ever increasing pharmaceutical production (deGennes 1999). Thus understanding granular materials can provide important design and modeling information which can have significant technological and economic impact. Geological processes like landslides, avalanches, pyroclastic flows and motion of sand dunes involve large scale flows of particulate solids (Iverson 1997). These natural phenomena can cause wide scale damage to life and property. Thus any advances in understanding the flows of granular media can potentially help us in predicting the actual occurrence and evolution of such events.

However, there remains a poor understanding of granular systems occurring in both nature and industry. Industrial operations involving processing of granular media, like milling, mixing, conveying, tableting, granulation etc., are poorly un-

derstood and operate at low efficiency (Merrow 1985). Scale-up of particulate processes still remains a major challenge (Bell 2005). Most of the problems in particulate processing in industry are solved using empirical means, and there is no sound fundamental understanding of these systems. Equations like ideal gas law and Navier-Stokes equation which are routinely used for describing flow of liquids and gases are not yet verified for particulate systems. Thus there is a strong need to build a fundamental framework for granular systems and understand the physics of such materials.

As a result, along with engineers and geologists, the study of granular materials has been recently emerging as an active area of research among the physics community. Over the last decade, physicist have been probing the granular systems, which seem to exhibit rich, interesting, and only partially understood collective behavior (Kadanoff 1999, deGennes 1999, Goldhirsch 2003). Far from being simple materials with simple properties, they display an astounding range of complex behavior that defies their categorization as solid, liquid, or gas. Examples of such behavior include the ability to de-mix when poured (Makse, Havlin, King & Stanley 1997), to form waves or ripples when shaken (Melo, Umbanhowar & Swinney 1995) or blown (Bagnold 1941), and to expand when squeezed (Reynolds 1885).

Some important aspects set granular materials apart from more traditional many-particle systems like dense gases or suspensions. First, ordinary temperature has no effect on grain motion, because external forces such as gravity dominate the materials behavior. Second, frictional interactions between individual grains are highly nonlinear, and even discontinuous for static friction. Third, there is no convenient large separation of scales as in liquids or solids: patterns such as waves or failure zones occur on scales only 1-100 times that of the smallest building block, the individual grain. These aspects not only make it very difficult to predict and control the behavior of granular materials but also pose fundamental conceptual challenges for

their description (Jaeger, Shrinbot & Umbanhowar 2000, Goldhirsch, Noskowicz1 & Bar-Lev 2005). Thus the study of granular materials is a challenge to engineers and physicists and is developing as a fast growing and fascinating field of research.

1.2 Fundamental microscopic interactions

The most fundamental microscopic property of granular materials is irreversible energy dissipation in the course of interaction (collision) between the particles. For the case of so-called dry granular materials, (i.e. when the interaction with interstitial fluid such as air or water is negligible) the encounter between grains results in dissipation of energy while total mechanical momentum is conserved. In contrast to the elastic interaction of particles in molecular gases, the collisions of macroscopic grains are generally inelastic. The coefficient of restitution, $0 < e < 1$, characterizes the energy lost in the collision. The relation between the velocities after the collisions ($\vec{v}'_{1,2}$) and before the collision ($\vec{v}_{1,2}$) for two identical spherical particles is given by

$$\vec{v}'_{1,2} = \vec{v}_{1,2} \mp \frac{1+e}{2}[\hat{n}_{12} \cdot (\vec{v}_1 - \vec{v}_2)]\hat{n}_{12} \tag{1.1}$$

Here $\hat{n}_{12}$ is the unit vector pointed from the center of particle 1 to the center of particle 2 at the moment of collision. The case of $e = 1$ corresponds to the elastic collisions and $e = 0$ characterizes fully inelastic collisions.

Energy can also be lost by rubbing or sliding, characterized by a coefficient of friction, μ. The dissipation of energy through inelasticity and friction raises the temperature of the atoms that constitute the grains but the associated thermal energy is approximately 18 order of magnitude smaller than the potential energy needed to lift one typical grain (of size 1mm) over another, in a gravitational field. Therefore, Brownian motion is irrelevant in the collective behavior and grains remain locked in place once they come to rest. Hence, this dissipation of energy in inter-particle contacts and collisions requires that energy be continuously input into the

system to induce or maintain motion.

1.3 Dynamic behavior in granular matter

As discussed in Section 1.2, thermodynamic fluctuations do not play a role in granular systems. Hence for granular systems to remain active, they have to gain energy from sources like gravity, shear, vibration etc., and are thus far from equilibrium systems. We may also use external volume forces like electric and magnetic fields (Chen, Hou, k. Lu, Jiang & Lam 2001, Aranson & Olafsen 2002) and flows of interstitial fluids such as water or air (Bocquet, Losert, Schalk, Lubensky & Gollub 2001*a*) to fluidize the grains.

1.3.1 Gravity

Gravity driven flow of granular materials is of interest within the contexts of both industrial processing of powders and geophysical instabilities like landslides and avalanches. Thus gravity driven flows like the chute flow and avalanches have been extensively studied in the granular research community. The gravity driven systems have been found to be complex, exhibiting several different flow regimes (Augenstein & Hogg 1978, Savage 1979, Silbert, Ertas, Grest, Halsey, Levine & Plimpton 2001) as well as particle segregation effect (Savage & Lun 1988, Drahun & Bridgewater 1983, Makse et al. 1997) and instabilities (Pouliquen, Delour & Savage 1997, Forterre & Pouliquen 2001, Forterre & Pouliquen 2003, Daerr, Lee, Lanuza & Clment 2003).

Gravity flow of granular materials in chutes and channels primarily depend on the particle properties and the nature of the surface over which they flow (Augenstein & Hogg 1978, Savage 1979, Makse et al. 1997). For smooth surfaces, flow occurs primarily by sliding at the surface, and little or no shear is introduced into the stream. In the case of highly roughened surfaces consisting of a stationary layer of the same particles, there appears to be no slip at the surface, and flow occurs entirely

by shear within the flowing stream. Surfaces of intermediate roughness lead to flow in which both slip at the surface and shear within the bed contribute significantly. The salient features are the existence in both 2D and 3D flows of three principal regions, corresponding to no flow, stable flow, and unstable flow (Silbert et al. 2001). These three regions are separated by two angles: θ_r, the angle of repose, and θ_{max}, the maximum stability angle, the largest angle for which stable flow is obtained. For $\theta < \theta_r$, granular flow cannot be sustained. In the region $\theta_r < \theta < \theta_{max}$, a steady-state flow is obtained. For $\theta > \theta_{max}$, the development of a shear thinning layer at the bottom of the pile results in lift-off and unstable acceleration of the entire pile. Velocity profiles have been measured experimentally under a variety of conditions, and the effects of such variables as roughness and inclination of the surface, depth of the flowing stream and particle size have been evaluated quantitatively.

Particle segregation is commonly observed during the heap formation process. When a heap is formed by pouring, free surface segregation is the process by which free flowing particles separate. Drahun & Bridgewater (1983) studied the mechanism of free surface segregation and found that particle diameter and density had a significant effect on the segregation process. Grains larger than the bulk or less dense are more likely to be found near the base of the pile whereas those smaller than the bulk or more dense would sink are more likely to be near the top and close to the pouring point. When a binary mixture of particles is poured on a horizontal plate, sometimes spontaneous stratification appears, with alternating layers of small and large particles, parallel to the surface of the sand pile. Makse et al. (1997) have suggested a possible mechanism for this mode of segregation based on the difference in the angles of repose for the two particles. Another example of segregation occurs when binary mixture of particles of two different sizes is made to flow down an inclined chute and the larger particles are found to preferentially migrate to the surface shear layer of the flow (Savage & Lun 1988).

Gravity-driven granular flows are also prone to a variety of nontrivial secondary instabilities in granular chute flow: fingering (Pouliquen et al. 1997), longitudinal vortices in rapid chute flows (Forterre & Pouliquen 2001), long modulation waves (Forterre & Pouliquen 2003), and others. A rich variety of patterns and instabilities has also been found in underwater flows of granular matter: transverse instability of avalanche fronts, fingering, pattern formation in the sediment behind the avalanche, etc (Daerr et al. 2003).

1.3.2 Shear

Energy is often supplied to a granular system through the shear which is driven by the moving walls of the container. Some of the most commonly used geometries for this class of systems are a) horizontal cylinder rotated around its axis, or rotating drum geometry and b) the Couette cell geometry.

Partially filled rotating drums which also show behavior similar to chute flow described in Section 1.3.1, are often used in chemical engineering for mixing and separation of particles. Flows in rotating drums have recently become a subject of active research in the physics community. For not too high rotating rates the flow regime in the drum is separated into an almost solid-body rotation in the bulk of the drum and a localized fluidized layer near the free surface. Slowly rotating drums exhibit oscillations related to the gradual increase of the free-surface angle to the static angle of repose and subsequent fast relaxation to a lower dynamic angle of repose via avalanche. Transition to steady flow is observed for the higher rotation rate (Rajchenbach 1990). The scaling of various flow parameters with the rotation speed e.g., the width of the fluidized layer, etc. and the development of correlations in dry and wet granular matter were recently studied by Tegzes, Vicsek & Schiffer (2002), (Tegzes, Vicsek & Schiffer 2003).

Rotating drums are typically used to study size segregation in binary mixtures

of granular materials. Two types of segregation are distinguished: radial and axial. Radial segregation is a relatively fast process and occurs after a few revolutions of the drum. As a result of radial segregation, larger particles are expelled to the periphery and a core of smaller particles is formed in the bulk (Metcalfe, Shinbrot, McCarthy & Ottino 1995, Khakhar, McCarthy & Ottino 1997, Ottino & Khakhar 2000). Axial segregation, occurring in the long drums, happens on a much longer time scale hundreds of revolutions. As a result of axial segregation, bands of segregated materials are formed along the drum axis (Hill & Kakalios 1994, Hill & Kakalios 1995). Segregated bands exhibit slow coarsening behavior. Even more surprisingly, under certain conditions axial segregation patterns show oscillatory behavior and travelling waves (Choo, Molteno & Morris 1997, Fiodor & Ottino 2003).

Granular matter sheared by confining the material in a Couette cell arrangement was first investigated in the pioneering work of Bagnold (1954), (Bagnold 1966). In this arrangement the granular media was placed between two vertical co-axial cylinders involving rotating inner cylinder at constant velocity and stationary outer cylinder. The observed response of granular media to shear stress was very different from ordinary fluids. Rather than deforming uniformly, materials such as dry sand or cohesionless powders develop shear bands i.e. narrow zones of large relative particle motion, with essentially rigid adjacent regions. Several recent experiments and simulations investigated individual particle motion in the same geometry (Schllmann 1999, Mueth, Debregeas, Karczmar, Eng, Nagel & Jaeger 2000). Experimental results reported by Mueth et al. (2000) on three-dimensional Couette cells indicate that the granular microstructure plays an important role in determining the velocity and density profiles within the cell. Losert *et al.* (Losert, Bocquet, Lubensky & Gollub 2000, Bocquet, Losert, Schalk, Lubensky & Gollub 2001*b*) also experimentally determined the particle dynamics and shear forces in a modified Couette geometry. In this geometry, the granular media is fluidized by an upward

flow of air and sheared by rotation of the inner cylinder. Measurements were made for the mean particle velocities and the velocity fluctuations on the upper surface of granular media. The experimental results were then quantitatively described using a locally newtonian hydrodynamic model. The main features of shear flow experiments in two and three dimensions are that the particle velocity decreases strongly away from the moving boundary, the velocity profile normalized by shear velocity is independent of shear rate and shear dynamics and the shear force is approximately independent of shear velocity if the granular material is allowed to dilate.

1.3.3 Vibration

Vibration of granular materials is also of interest for more practical reasons. In industry, vibration is commonly used as an aid to handling and transporting particulate materials such as foodstuffs, coal, and pharmaceuticals. Examples of devices that often utilize vibration include conveyor belts, hoppers, sorting tables, packing tables, drying plates, and fluidized bed reactors. Vibration of a granular material may also play an important role in natural events such as earthquakes and avalanches. Clearly, understanding how a granular material responds when subjected to vibration can provide valuable design information.

Experiments have shown that a number of interesting phenomena appear when beds of granular materials are subjected to external, vertical oscillations. Early scientific investigations of granular materials date back to Coulomb (1773) who studied inter-particle friction and its effect on granular piles. Chladni (1787) was perhaps the first to systematically study the behavior of vibrated beds of particles. He observed that when sand is scattered on a vibrating membrane, the sand particles migrated to the vibration anti-nodes inducing a wide range of patterns on the layer's surface. Faraday (1831) showed that these patterns were due to induced motions of the air surrounding the vibrating membrane. In subsequent years the focus of

attention was diverted from dynamical properties of thin layers of vibrated sand, and only in the last third of the 20^{th} century physicists returned to this old problem equipped with new experimental capabilities. The current interest in these problems was initiated by Thomas, Mason, Liu & Squires (1989) who studied different states in shallow vibrated beds, and by Douady, Fauve & Laroche (1989) who studied heaping phenomena in vibrated beds with and without interstitial gas. Eventually, after more careful analysis, Pak & Behringer (1995) concluded that heaping indeed disappears as the pressure of the ambient gas tends to zero or the particle size increases. Melo *et al.* (Melo et al. 1995, Melo, Umbanhowar & Swinney 1994) further carried out experimental studies on thin vibrated granular layers in evacuated containers. They reported a phase diagram describing the various standing wave patterns observed under vibration. This was followed with studies by Umbanhowar, Melo & Swinney (1996) on localized excitations in a vertically vibrated granular layer. In general, the research focus during the 90's was on studying pattern formation in vibrated granular materials. During the last few years researchers have started developing interest in investigating the field of phase transitions in vibrated granular media, which remains largely unexplored. In our study, we are primarily interested in the dynamics of granular materials, which are set into motion by external vertical vibrations and the accompanying phase transition phenomena.

1.4 Solid-Fluid transitions in vibrated granular matter

An extensive discussion of recent investigations on granular materials can be found in the review articles by Jaeger & Nagel (1992, 1996), Jaeger et al. (1996), Shinbrot & Muzzio (2000, 2001) and Goldhirsch (2003). These investigations show that granular materials can exist in solid like and fluid like states. Physical understanding of the flow of granular materials has thus developed along two major themes based on

the flow regime (Jackson 1986). In the *rapid flow*- fluidlike regime, both theory and experimental analysis are generally cast in the framework of kinetic theory (Campbell 1990, Goldhirsch 2003). This work was led by Savage & Jeffery (1981), Lun, Savage, Jeffery & Chepurniy (1983) and Jenkins & Richman (1984), who built upon the classic work on non-uniform gases by Chapman & Cowling (1952). A brief review of the kinetic theory concepts and the relevant literature is provided in Section 5.1 and Section 5.4. In contrast, the *slow flow* -solidlike regime is most commonly described using the tools of soil mechanics and plasticity theory (Nedderman 1992) and recently by analogy to glasses (Kurchan 2000, D'Anna & Gremaud 2001, Barrat, Loreto & Sellitto 2001). These two approaches have no well understood region of overlap. This has given rise to questions related to the criterion for transition between fluid like and solid like states of granular materials.

There are few studies which focus on the solid to fluid transition. Metcalfe, Tennakoon, Kondic, D.G.Schaeffer & Behringer (2002) studied solid to fluid transition in a horizontally vibrated container of beads. They observed hysteresis in the transition which was well predicted by a dry friction model in which the friction coefficient varies smoothly between a dynamic and static value. A fluid-solid transition was also observed by D'Anna & Gremaud (2001) for vertically vibrated particles. Olafsen & Urbach (1998) carried out experiments with sub-monolayers of particles subject to vertical vibration at very low amplitude. Their studies revealed a surprising phenomenon: formation of a dense closely-packed cluster co-existing with dilute granular gas. The phenomenon bears a strong resemblance to the first-order solid/liquid phase transition in equilibrium systems. Similar experiments by Losert, Cooper & Gollub (1999) discovered propagating fronts between gas like and solid like phases in vertically vibrated sub-monolayers. Prevost, Melby, Egolf & Urbach (2004) performed experiments with vibrated granular gas confined between two plates and observed qualitatively similar phase coexistence. Daniels & Behringer

(2005) studied the order (crystallization)-disorder transition in a 3D annular shear cell vibrated from below and sheared from above. Under sufficient vibration the granular system (monodispersed polypropylene spheres) exhibits a crystallized state, which can be melted by sufficient shear. Recently Gtzendorfer, Tai, Kruelle, Rehberg & Hsiau (2006) investigated the fluidization transition in vertically vibrated two-dimensional granular packings. An initially closed packed granular bed upon subject to increasing vertical sinusoidal excitation shows surface fluidization followed by complete fluidization of the entire bed of particles. The fluidization transition transition leads to discontinuous changes in the density distribution and in the root mean square displacement of the individual particles.

The objective of our present work is to gain further insight into the solid-fluid transitions in granular flows focussing on vibrated granular systems subjected to constant pressure (isobaric) and constant volume (isochoric) conditions.

Chapter 2

First-order phase transition in isobaric granular fluid

In this chapter, we present experimental results on the phase transition characteristics of an isobaric 2D granular fluid. We begin by describing the experimental apparatus and technique followed by illustrating in detail the observed features of the phase transition. We find the phase transition to be first-order in nature characterized by discontinuous changes in density and temperature. The transition also shows rate dependent hysteresis and entropic/free energy like features analogous to those developed for equilibrium fluids. We further explore the phase transition dependence on a variety of system parameters. Finally, we present a brief summary of the results along with some concluding remarks.

2.1 First order Phase transition

First order phase transition is a phase transition involving sudden change in one or more physical properties of the system such as density, temperature, pressure or any other thermodynamic variable. First order phase transitions exhibit a discontinuity in their first derivative of the free energy with a thermodynamic variable. The various solid/liquid/gas transitions are classified as first order phase transitions because they involve discontinuous change in density (which is the first derivative of the free energy with respect to the chemical potential).

The elastic hard sphere system is the simplest system, which undergoes a first-order phase transition (Alder & Wainwright 1962, Hoover & Ree 1968). This transition has been seen in simulation (Alder, Hoover & Young 1968) and experiments with colloids (Rutgers, Dunsmuir, Xue, Russel & Chaikin 1996). However, in these systems energy is conserved, and the concept of free energy is well defined. In dissipative systems, such as granular systems or inelastic hard spheres, the concept of free energy is not established (Kadanoff 1999). Granular systems are far from equilibrium systems, which require continuous energy input to remain in motion. The balance between energy injection and dissipation creates a nonequilibrium steady state (NESS). We experimentally examine this NESS in our granular system for phase transition studies.

2.2 Experimental apparatus

A schematic diagram of the experimental setup is shown in Fig. 2.1. The experimental apparatus consisted of a vertical container of dimensions $17.5D$ wide, by $20D$ tall, by $1.1D$ deep, where $D = 3.175mm$ is the diameter of the grains used. The spherical stainless steel ball bearings (grains) were placed in the container confined between two vertical, parallel glass plates separated by a gap measuring $1.1D$. The lateral walls of the container define the $2D$ volume in which the particles move. A thin plunger slid through a slot in the bottom of the cell and was connected to an electromechanical shaker using a rigid shaft. The plunger provided vertical sinusoidal excitation to excite(heat) the particles. A freely floating weight confined the particles from the top allowing the volume to fluctuate, but providing constant pressure boundary conditions.

The electromechanical shaker ($VG100-6$ Vibration Test System) was anchored firmly to a solid aluminium base with heavy weights placed on the base to damp out any unwanted vibrations. Levelling of the apparatus was crucial to ensure

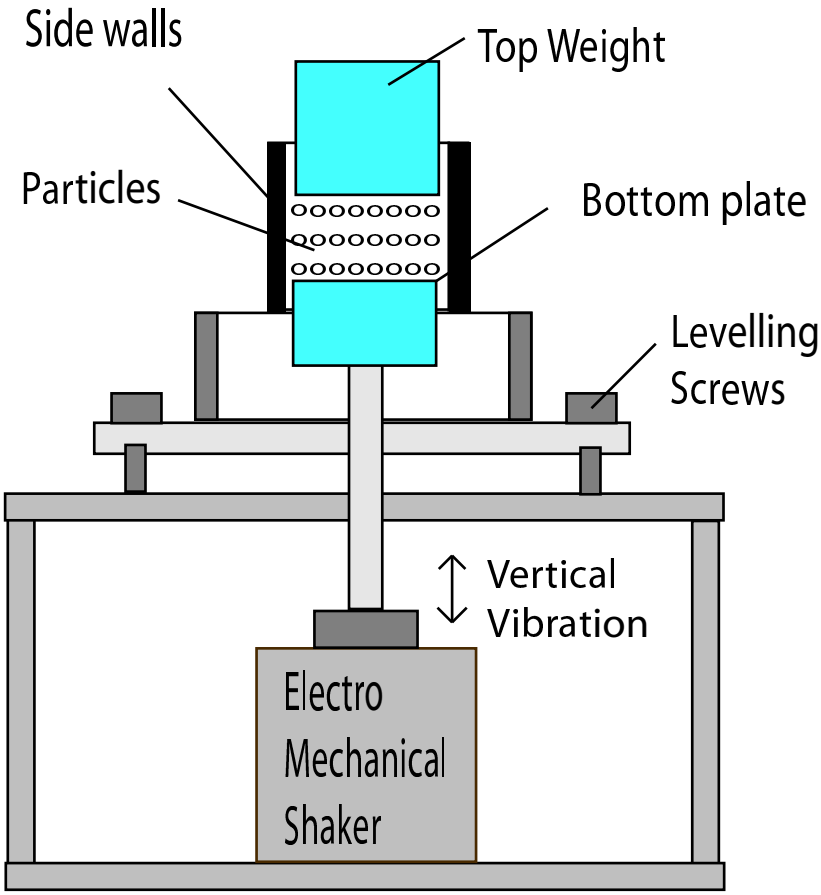

Figure 2.1: Schematic diagram of the experimental setup: Front view showing the details of vertical cell and driving arrangement.

homogeneous forcing, as slight inclinations of the shaking surface or the cell could strongly bias the motion of the particles. We thus used high precision micrometer screws for levelling purpose. The shaker was driven sinusoidally using a stable function generator whose output was first amplified by a high quality DC coupled power amplifier. An oscilloscope was used to monitor the input signal fed to the amplifier. An accelerometer attached to the shaker provided real time accurate measurements of the driving acceleration. A feedback control loop was established

to set the acceleration to a desired value.

The dynamics of the system was imaged from the front by digital photography using a gray-scale DALSA CA-D6 fast camera at 840 frames per second. A custom made Light emitting diode (LED) array light source located behind the cell was used for illumination purpose. The LED's were mounted in a 16 by 8 array on an printed circuit board (PCB) and provided a highly directional and intense light source. A plastic diffuser attached to one of the vertical Plexiglass walls of the cell was used to provide homogeneous illumination. The particles as well as the top and bottom plate appear dark in front of a bright background. We have developed a custom made tracking software to extract the particle positions and the position of top and bottom plates from the acquired images (260×260 pixels) to subpixel accuracy (approximately $6\mu m$). We track the particles from frame to frame and assign a velocity to each one, typically $\sim D/5$ per frame.

2.2.1 Experimental parameters and procedure

We define the number of rows $R = N/17$, where N is the number of particles in the cell, and 17 is the number of particles to fill an entire row. The driving is characterized by the nondimensional maximum acceleration $\Gamma = A(2\pi f)^2/g$, where A is the maximum amplitude of the plunger, f is the driving frequency and g is the acceleration of gravity.

The experimental parameters of our system are: a) the applied pressure as defined by the top weight (W), b) the driving frequency (f), c) dimensionless acceleration (Γ), d) the number of particles in the cell N and e) particle material type. We have performed experiments to explore the effect of these parameters on the first-order phase transition phenomena. The majority of the experiments were performed using stainless steel ball bearings, but we also plan to use aluminium, teflon, acrylic and glass spheres for future investigation.

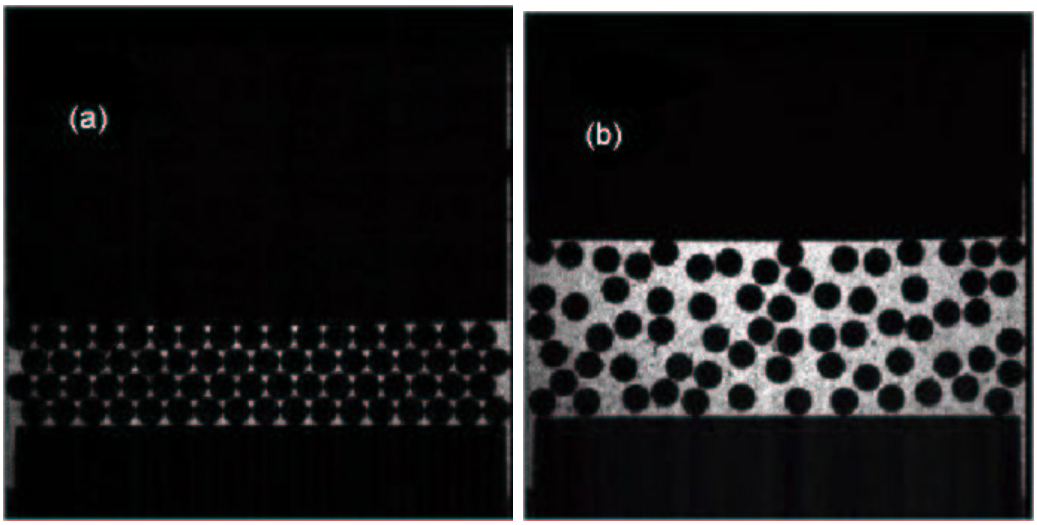

Figure 2.2: Typical experimental images of $2D$ granular layer in (a) crystalline phase and (b) gas phase.

To prepare the system initially in the densest state, we increase Γ to 16 and then slowly lower the acceleration to zero. Then we alternate taking 1024 pictures with a small increase in Γ and variable time delay (typically $1, 2$ or 11 seconds) until $\Gamma = \Gamma_{max}$. Then we repeat the same process while decreasing Γ to zero.

2.3 Discontinuity in density

We observe a first order hysteretic phase transition for integer number of rows, R=4 (N=68), and under constant pressure conditions (top weight $W = 4.5g$) as we vary the driving acceleration Γ. When Γ is low and R is an integer, a crystalline state develops [see Fig. 2.2a]. When Γ is high the granular system acts like a gas, as shown in Fig. 2.2b. In the crystal phase the particles vibrate about their lattice sites and do not undergo any rearrangement, while in the gas phase particles are fluidized and rapidly diffuse around the cell similar to gas molecules.

Fig. 2.3(a) shows a typical example of the behavior of the system for $R = 4$. We plot the volume fraction ν of the particles as a function of the driving acceleration Γ. We find that below $\Gamma = 1$ the system is essentially stationary and the volume

fraction, ν is nearly constant. As we increase Γ further in small increments (≈ 0.2), we observe gradual decrease in the volume fraction up to $\Gamma = 8.8$. At this point there is a sharp drop in the volume fraction (ν), ν drops by $\approx 15\%$. Further increase in Γ results in continuous decrease in ν and no discontinuity is observed. As Γ is lowered, the process is reversed, but the transition point shows a 25% hysteresis, occurring at $\Gamma = 7.4$. Thus we observe features of first order phase transition showing discontinuity in density (volume fraction ν) at the transition point as well as hysteresis. The hysteretic behavior will be discussed later in detail in Section 2.5.

2.4 Discontinuity in temperature during phase transition

We measure the granular temperature or average fluctuational kinetic energy of the particles from the collected data. In a normal gas, the temperature is isotropic and the kinetic energy in vertical velocity is same as that in horizontal velocity. In a granular system due to dissipation, at least two temperatures are needed in two dimensions, a horizontal temperature $T_{HH} = 1/2m < (v_x - < v_x >)^2 >$ and a vertical temperature $T_{VV} = 1/2m < (v_y - < v_y >)^2 >$, where m is the mass of the particles and v_x and v_y are the horizontal and vertical velocities respectively. We want to assign a single value to each temperature, so we take the averages over all particles and time (≈ 1.22sec). A non-trivial issue in the measuring of the temperature is the choice of the frame of reference. The most obvious implementation of the averages $< ... >$ is in the inertial lab frame; however this produces a finite temperature even if the plunger, particles, and weight all move with the same velocity. Taking the averages in the center of mass frame of the particles solves the problem, but the velocities are no longer simply related to the collision velocities with the top weight. Thus we have chosen to evaluate the averages in the frame of the top weight, which solves both the problems.

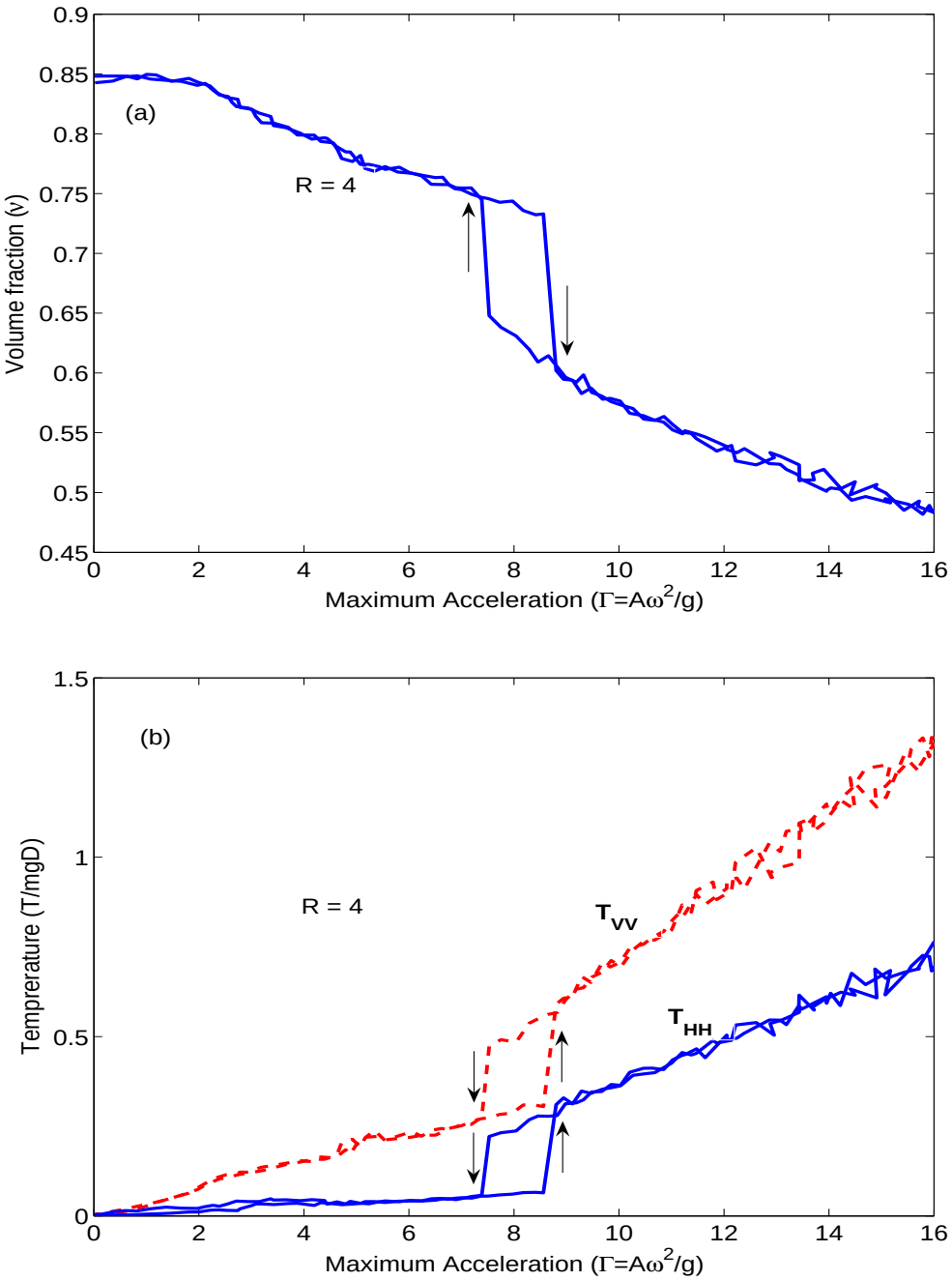

Figure 2.3: (a) Plot of volume fraction as a function of increasing and decreasing maximum acceleration (Γ), as indicated by the arrows, at R=4 and 50 Hz, under isobaric conditions (top weight, W=4.5g). (b) Plot of average vertical (dashed) and horizontal (solid) temperature as a function of Γ at 50 Hz, under isobaric conditions (R=4, W=4.5g)

.

The results for the temperature dependence of the system as function of increasing and decreasing Γ is shown in Fig. 2.3(b). As we increase Γ, for $1 < \Gamma < 8.8$, T_{VV} and T_{HH} show a linear increase with Γ. Initially, $T_{HH} \simeq T_{VV}/3$, but around $\Gamma = 5$ the ratio drops and stays around 20%, as shown in Fig. 2.4. At $\Gamma = 8.8$, T_{VV} and T_{HH} rise by factors of 3 and 5 respectively, and the ratio (T_{HH}/T_{VV}) reaches 50%. For $\Gamma > 8.8$, T_{VV} and T_{HH} continue to rise and the ratio reaches 55% by $\Gamma = 16$. As Γ is lowered the transition point is shifted to $\Gamma = 7.4$ showing a well defined hysteresis loop.

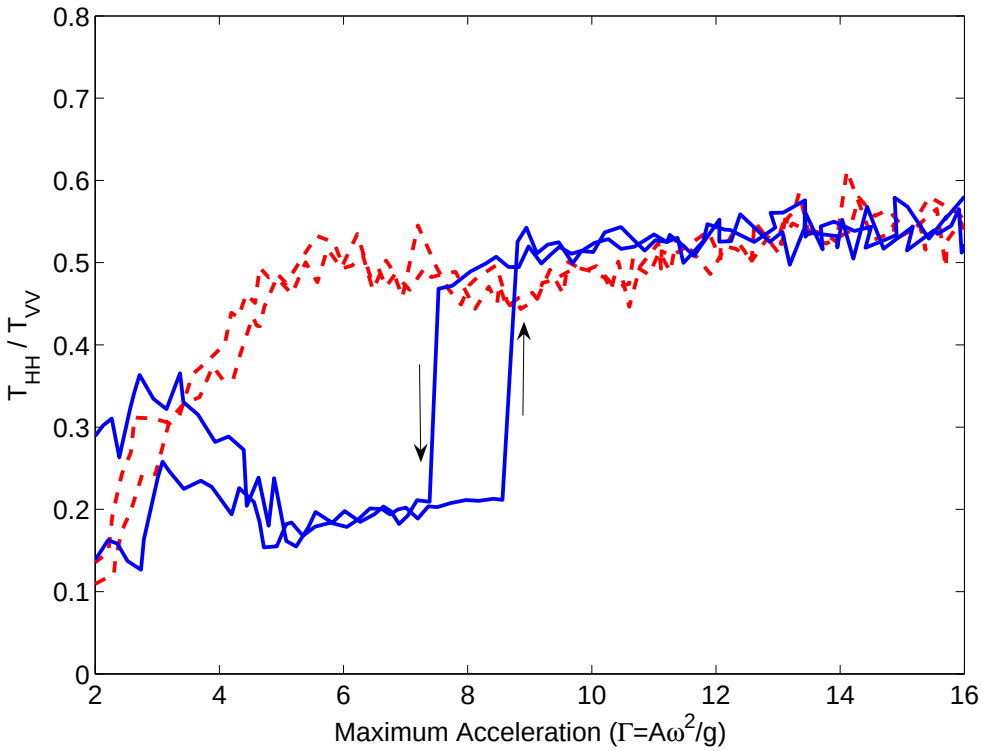

Figure 2.4: Plot of the horizontal to vertical temperature ratio for $R = 4$ (solid) and $R = 3.5$ (dashed) as a function of Γ, at 50Hz and under isobaric conditions (W=4.5g).

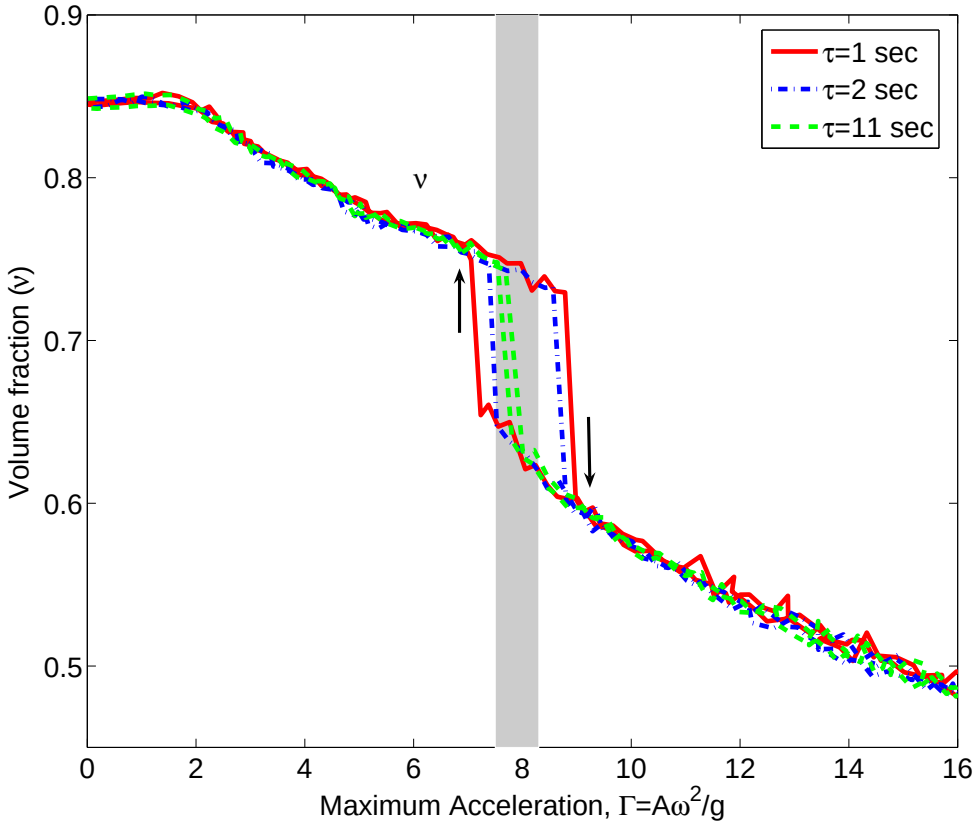

Figure 2.5: Plot of volume fraction as a function of increasing and decreasing maximum acceleration (Γ) at 50 Hz, under isobaric conditions (W=4.5g) for three different time delays (τ); 1 second (solid), 2 second (dotted) and 11 seconds (dashed). The shaded region (transition region) is investigated in detail in section 2.6

2.5 Hysteretic Phase Transition

The first order phase transition seen in integer number of rows (R) exhibits hysteretic behavior. Now we investigate the rate dependence of the hysteresis loop. To study this behavior we carry out runs for different time delays (τ =1 , 2 , 11 seconds) and investigate the effect on the width/size of hysteresis loop. Here time delay (τ) is the time between increments of Γ. As shown in Fig. 2.5, for τ =1 second delay we get the outermost hysteresis loop, which shows 25% hysteresis (difference between the Γ values corresponding to the two transition points normalized by the Γ value for

crystal to gas transition point) . For τ =2 second, we get the first inner loop showing about 15% hysteresis. Finally for τ =11 second, we get the innermost loop showing only 3% hysteresis and remarkably close to a reversible transition. We notice from Fig. 2.5 that, as the time delay between increments is increased (i.e. decreasing the heating rate) the size of the hysteresis loop shrinks and gives hint of reversible phase transition.

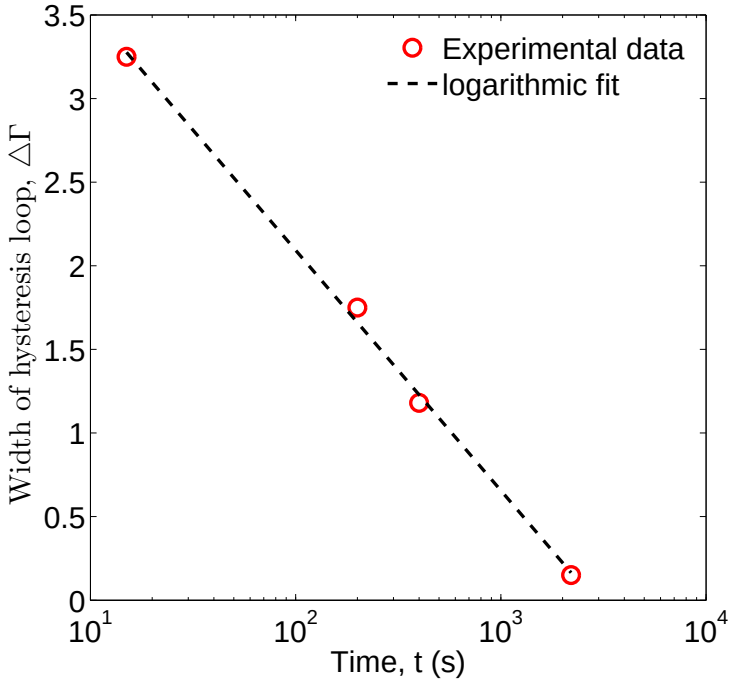

Figure 2.6: Plot of width of hysteresis loop ($\triangle\Gamma$) as a function of the total acquisition time (t) for the experimental runs. The dashed line represents logarithmic fit to the data.

To quantify the hysteretic behavior, we plot the width or size of the hysteresis loop ($\triangle\Gamma$) as a function of the total acquisition time as shown in Fig. 2.6. The size of the loop shows a logarithmic dependence on the time span of the run as given by the following equation,

$$\triangle\Gamma = -1.4364 log(t) + 4.9659. \tag{2.1}$$

The logarithmic decrease in the width of hysteresis loop with time suggests that the

hysteretic behavior is not an obligatory condition on the system and may disappear for sufficiently slow heating rate producing a reversible phase transition.

2.6 Phenomenological free energy/entropy model

We now specifically focus on the region in the vicinity of the hysteretic phase transition (the shaded region as shown in Fig. 2.5). We pick a Γ value which lies in the transition region and hold it constant for a period of approximately 15 minutes. During this interval we record the dynamics of the system by taking 8192 pictures at 10 frames per second. We repeat this procedure for several different Γ values in the transition (shaded) region. From the acquired images we extract the density of the system and plot it as a function of acquisition time. Fig. 2.7 shows the density plots for 3 different Γ's in the transition region and accompanying the probability distribution function of density at the respective driving accelerations. We clearly find that the density of the system fluctuates widely near the transition within our experimental acquisition window. The probability distributions of density also shows bimodal distribution suggesting two different prominent states/densities.

Further, in Fig. 2.8(a), we present a surface plot of the probability distribution of volume fraction $P(\nu, \Gamma)$ (for $R = 4$ and $\tau = 900$ second) in the vicinity of the hysteretic transition region. The vertical cross sections of $P(\nu, \Gamma)$ for fixed Γ are presented in Fig. 2.8(b)-(d). Below $\Gamma = 8.0$, we observe a sharp peak centered at $\nu = 0.725$. As we increase Γ and start approaching $\Gamma = 8.0$, we observe the emergence of secondary peak at low density ν (see Fig. 2.8(b)). For $\Gamma = 8.0$, we observe two peaks of approximately the same height located at $\nu = 0.625$ and $\nu = 0.725$ (see Fig. 2.8(c)). Above $\Gamma = 8.0$, we see the disappearance of the high ν maxima and the low density peak sharply rises (see Fig. 2.8(d)). We can interpret the above result with analogy to the entropy maximization argument usually presented for equilibrium phase transition between two states (e.g transition between a crystal

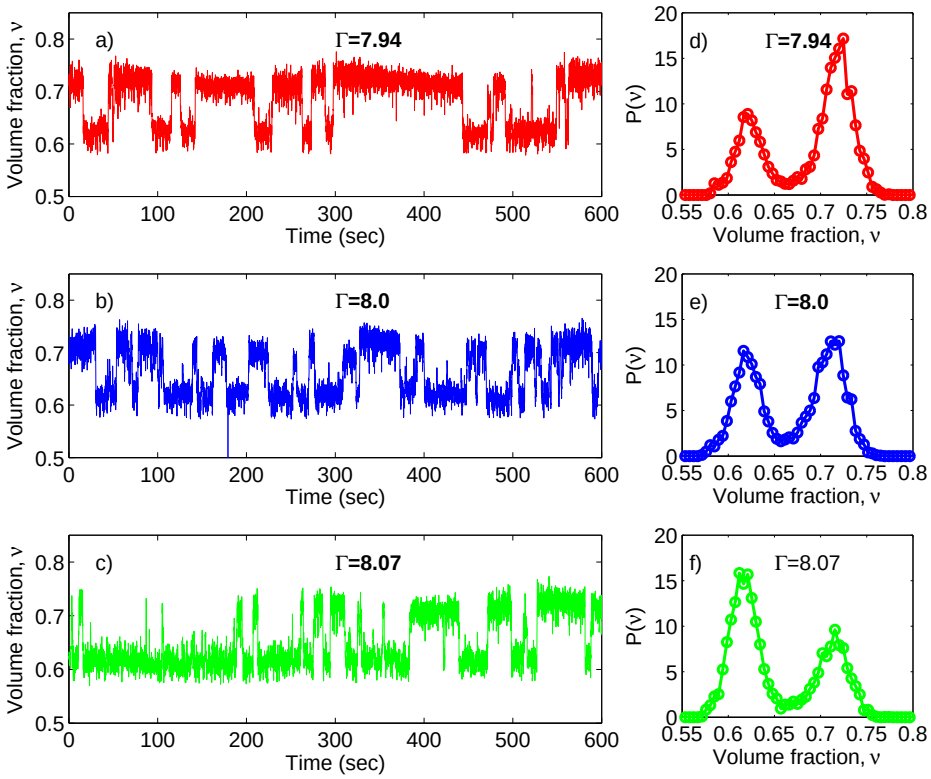

Figure 2.7: (a)-(c) Plots of volume fraction (ν) as a function of acquisition time (t) for three different Γ's (7.94,8.0,8.07) in the vicinity of the phase transition region. (d)-(f) Probability distribution of volume fraction for $\Gamma = 7.94$, $\Gamma = 8.0$ and $\Gamma = 8.07$. The system parameters are: $R = 4$, $N = 68$, $f = 50$Hz, $\tau = 900$s and $W = 4.5g$.

and a gas). At low Γ, our system is more likely to be in a crystalline phase (high density region) as seen from the $P(\nu, \Gamma)$ plot. As we approach the transition point, the system oscillates between a crystal and a gas but the probability of occurrence of the crystal state is higher (for $\Gamma < 8.0$). At the exact transition point we expect both the phases to be equally probable (for e.g. $\Gamma = 8.0$). As we cross the transition point, the probability of occurrence of the gas state is much higher (for $\Gamma > 8.0$) as compared to the crystal phase. Thus at a particular Γ, our system achieves a state corresponding to maximum $P(\nu)$, analogous to maximum entropy phenomena for the case of equilibrium phase transitions. Further, we can accurately model the

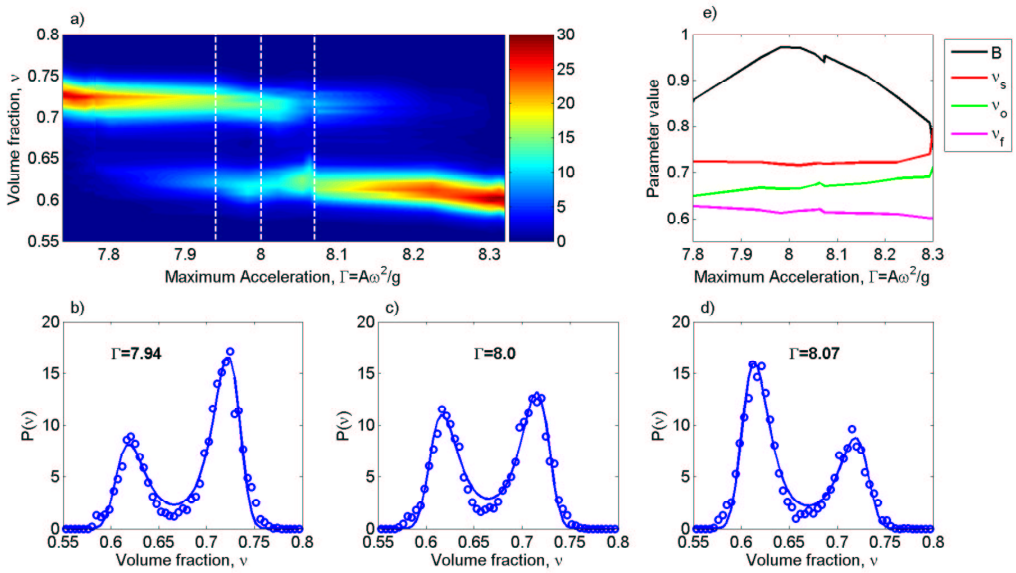

Figure 2.8: (a) Surface plot for the probability distribution of volume fraction $P(\nu, \Gamma)$, for $R = 4$ and $\tau = 900$ second. The value of $P(\nu, \Gamma)$ is given by the adjacent color bar. The vertical dashed lines are located at $\Gamma = 7.94$, $\Gamma = 8.0$ and $\Gamma = 8.07$. (b)-(d) Plots of $P(\nu)$ (vertical cross-section of $P(\nu, \Gamma)$ distribution) for three different values of Γ. The solid curves represent the fits provided by the functional form as given by Eqn. (2.3). (e) Dependence of the fitting parameters B, ν_f, ν_s and ν_o on Γ.

behavior of experimental $P(\nu)$ by the following functional form,

$$P(\nu) = A \exp[-F(\nu)] \tag{2.2}$$

and $F(\nu)$ is defined by

$$F(\nu) = B(\frac{\nu^4}{4} - C\nu^3 + \frac{D}{2}\nu^2 - E\nu) \tag{2.3}$$

where, A is the integration constant and B, C, D and E are the fitting parameters. The parameters C, D and E take the following form: $C = \nu_f + \nu_o + \nu_s$, $D = \nu_f\nu_s + \nu_s\nu_o + \nu_f\nu_o$ and $E = \nu_f\nu_o\nu_s$ where, ν_f, ν_s, ν_o are the locations of the maxima corresponding to fluidlike state (*fluidus point*) and solidlike state (*solidus point*) and the location of the minima respectively. In Fig. 2.8(b)-(d) we plot the experimental $P(\nu)$ along with the description provided by Eqn. (2.3), for three

representative values of Γ. The proposed functional form of $P(\nu)$ (solid curve) clearly describes the behavior of experimental $P(\nu)$ at various Γ. The values of the fitting parameters B, ν_f, ν_s and ν_o depend on the control parameter Γ as shown in Fig. 2.8(e). The proposed phenomenological model (Eq. (2.3) is identical to the Ginzburg-Landau free energy functional (Ginzburg & Landau 1950, Gracheva, Rickman & Gunton 2000), widely used to model phase transitions in superconductors, ferromagnets, alloys, superfluids and crystalline solids. The strong resemblance observed between the behavior of $P(\nu)$ and the equilibrium entropy/free energy at the phase transition shows that the same mechanism may be at work for non-equilibrium phase transitions as well.

2.7 Pressure dependence

The phase transition experiments were carried our under isobaric conditions, hence the pressure exerted by the top weight becomes a very crucial system parameter affecting the phase transition. We thus study the effect of pressure as set by the top weight on the phase transition. We define the applied pressure as follows:

$$\bar{P} = \frac{W + W + m_T}{2L} = \frac{W + m_T/2}{L} = \frac{m_T\,(M_R + 1/2)}{L}, \tag{2.4}$$

where the mass ratio $M_R = W/m_T$ is the mass of the top weight W divided by the total mass of the particles $m_T(\approx 9\ g)$ and L is the width of the cell. The pressure is directly proportional to M_R. Thus to change the pressure we change the mass ratio M_R keeping other parameters (m_T and L) constant. Fig. 2.9 shows the first-order phase transition for four different values of M_R. As the pressure is increased, the transition point is shifted to higher values of Γ. This dependence is not linear since it appears that the shift on critical value of Γ is smaller and smaller as we increase the pressure. For $M_R = 0.25$ the critical value is around $\Gamma_c \approx 6.0$, for $M_R = 0.5 : \Gamma_c \approx 8.2$, $M_R = 0.75 : \Gamma_c \approx 11.5$ and $M_R = 1 : \Gamma_c \approx 12$. Thus,

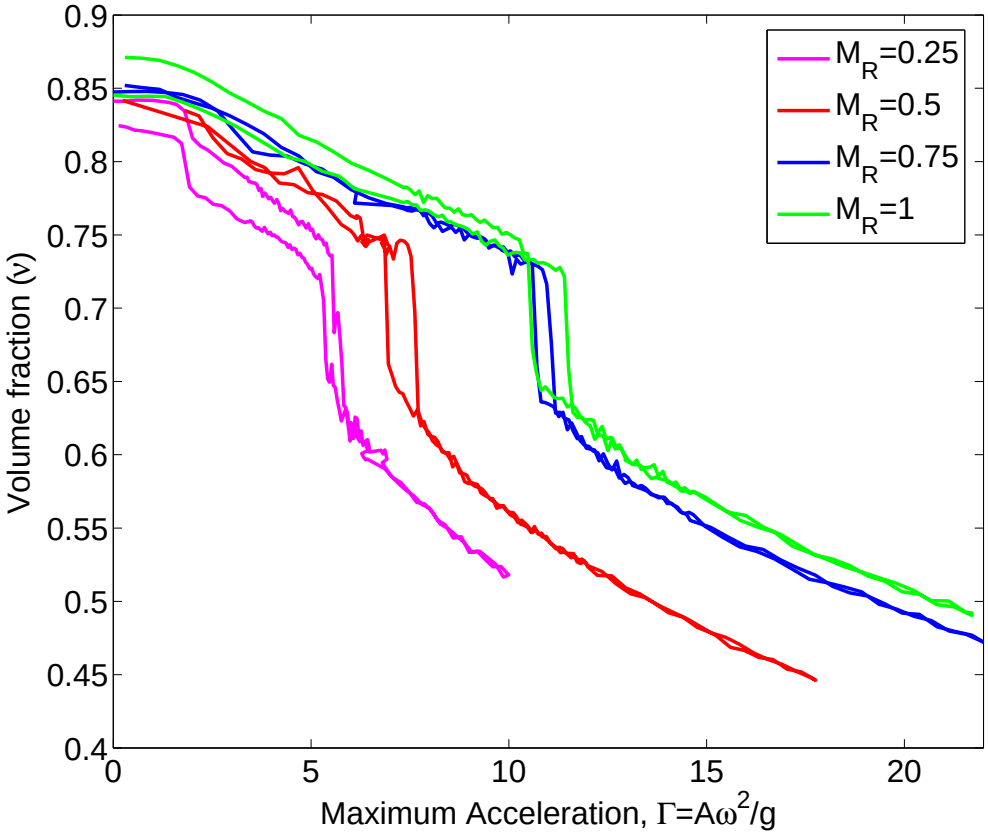

Figure 2.9: Plot of volume fraction as a function of increasing and decreasing maximum acceleration (Γ) at 50 Hz and for time delay τ=10s, under isobaric conditions for four different different values of mass ratio (pressure), M_R =0.25, 0.5, 0.75 and 1.

higher pressure require a larger energy input to bring about the phase transition. We always start the experiment with a perfect crystalline arrangement of particles. However, at the end of the run we sometimes observe defects in the final crystal. This effect was found to be more pronounced for low pressures as can be seen from the $M_R = 0.25$ result, where the system has a different ending volume fraction/density.

2.8 Frequency dependence

Fig. 2.10 shows the effect of driving frequency on the phase transition. The vibration frequency is varied from low (20Hz) to high values (90Hz) keeping the mass ratio

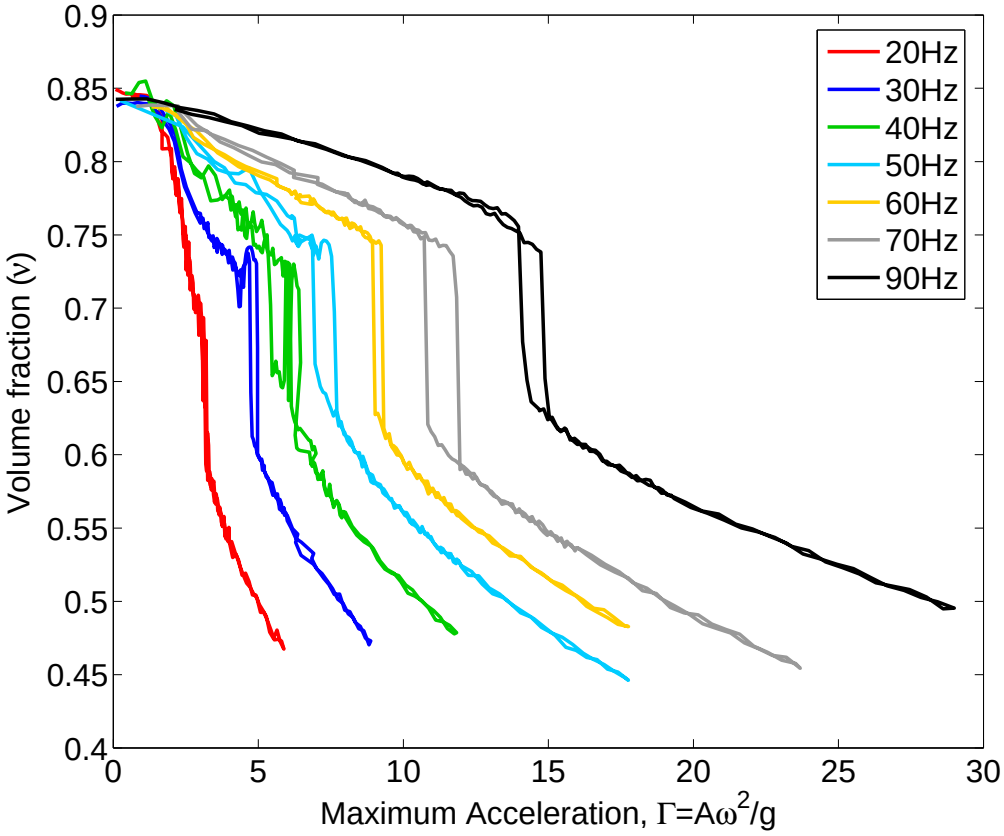

Figure 2.10: Plot of volume fraction as a function of increasing and decreasing maximum acceleration (Γ) for various driving frequencies, under isobaric conditions (W=4.5g, M_R=0.5) for $R = 4$ and time delay, τ=10s

constant at $M_R = 0.5$. The transition point Γ_c is shifted to higher values as we increase the frequency. Thus the transition point Γ_c is linearly dependent on the frequency. All the experimental curves more or less show a sharp discontinuity in the density along with the presence of hysteresis loop. The hysteresis loop seems to shrinks with decrease in frequency but no specific trend is observed.

At low frequencies, we observe higher fluctuations in density in the crystal regime as compared to the high frequency data set. This can be explained as follows: For low frequencies there is a regime where Γ is a relevant parameter. At the very beginning of the run, the limit $\Gamma = 1$ determines if the spheres are bouncing or not

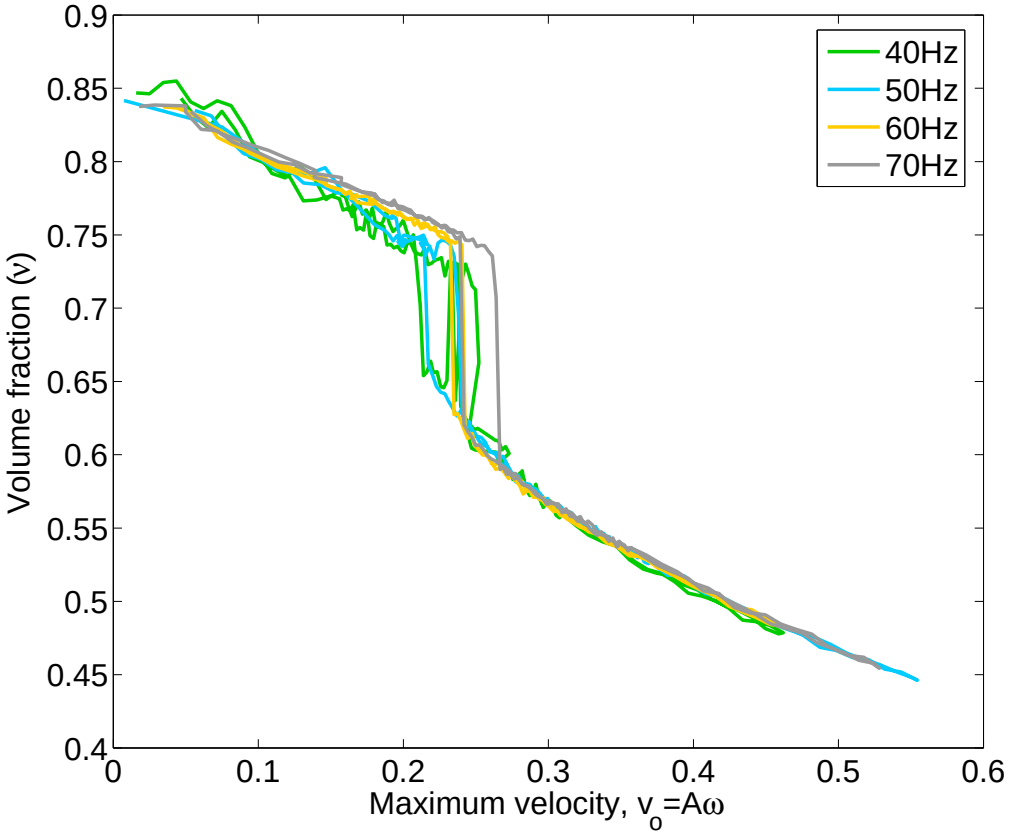

Figure 2.11: Plot of volume fraction as a function of maximum bottom plate velocity, $v_o = A\omega$ for various driving frequencies, under isobaric conditions (W=4.5g, M_R=0.5) for $R = 4$ and time delay, τ=10s

on the bottom plate. Moreover for low frequencies, the period of vibration becomes very long compared to the relaxation time of the particles, which may induce those discrepancies. Another aspect is that for low frequencies, the amplitude of vibration A is much more bigger than for high frequencies for a given Γ ($\Gamma \propto A\,(2\pi f)^2$). Therefore for low frequencies, the system suffers a larger compression which may cause the observed discrepancies in the crystal state.

It is interesting to note that the frequency data collapse reasonably well when plotted against the bottom plate maximum velocity $v_o = A\omega$ (as shown in Fig. 2.11). The maximum bottom plate velocity seems to be more relevant parameter than Γ

to quantify the phase transition. The phase transition occurs when the bottom plate approximately reaches a maximum velocity of $v_o = 0.25m.s^{-1}$ over a range of driving frequencies employed.

2.9 Preliminary Investigations

In this section we review some of the ongoing investigations and preliminary results and also present some ideas for future investigations on the first-order phase transition study. For further details please refer the Future Work section in Chapter 6.

2.9.1 System size dependence in 2D

The phase transition results in previous sections were reported for an isobaric system with four rows ($R = 4$) of particles. We now vary the system size to investigate the effect on the phase transition properties. We can vary the system size in two ways: first, by varying the number of particle rows from 2 to 4 and secondly, by increasing the system dimension in the horizontal direction (increase the width of the cell) while keeping the number of rows constant. We would like the pressure gradient between the top and bottom of the cell to be as small as possible. This limits the maximum number of rows one can use to five rows of particles. However we can double the system size in the horizontal direction and study the system size effect keeping the pressure gradient small and same as that for a small cell.

For integer values of R ($R = 2, 3$ and 5), we observe a behavior similar to that for $R = 4$ rows. For $R = 3.5$ rows the behavior of the system is qualitatively different and typical plots for density/volume fraction (ν) and temperature (T) are shown in Fig. 2.12(a)-(b) respectively . In contrast to the behavior of the system for integer number of rows (R), we observe that all the properties of the system (density and temperature) change gradually and no discontinuity is observed. The

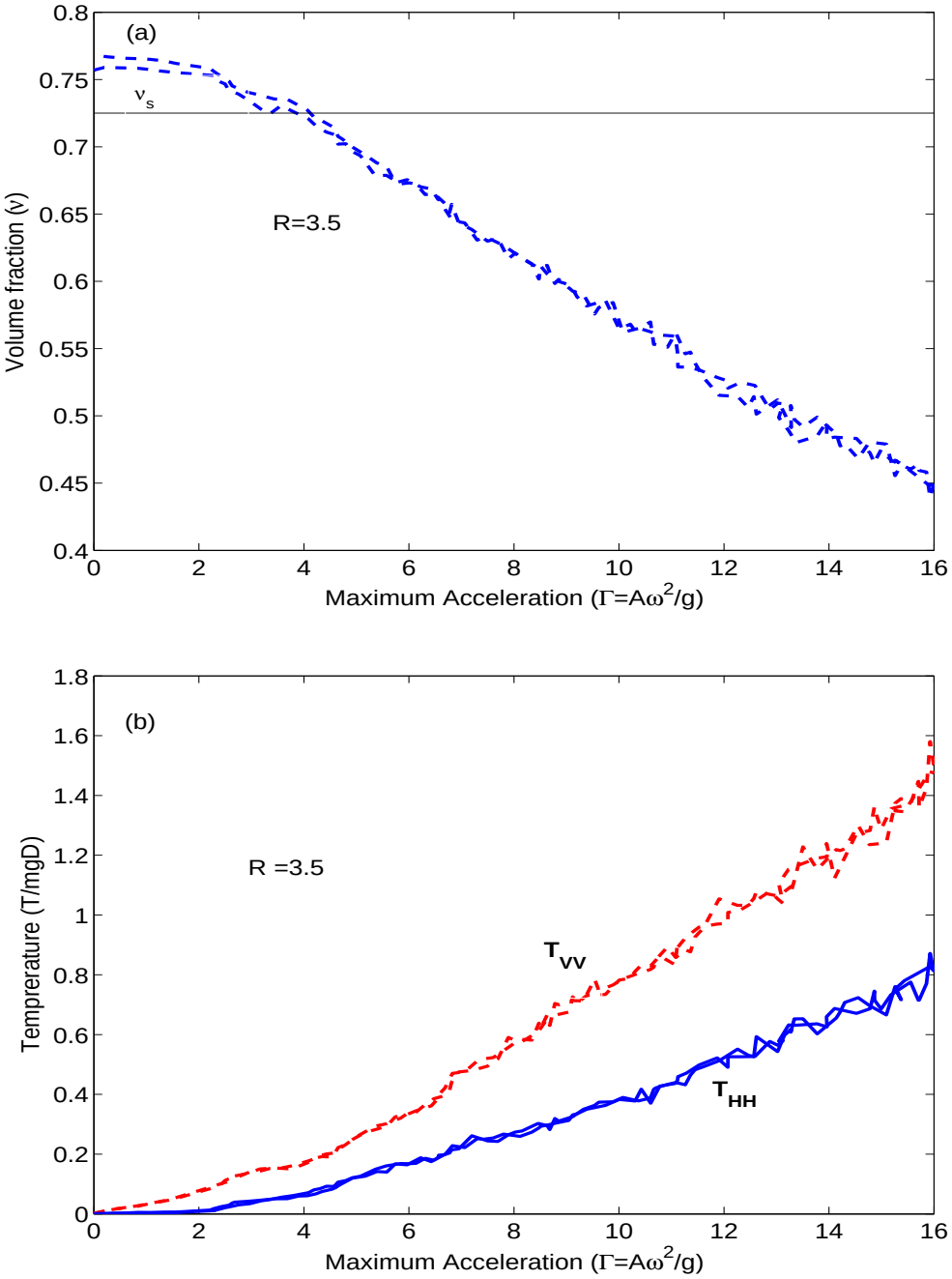

Figure 2.12: (a)Plot of volume fraction as a function of increasing and decreasing maximum acceleration (Γ) at 50 Hz, under isobaric conditions (W=4.5g) for $R = 3.5$. The horizontal solid line corresponds to the solidus point, $\nu_s = 0.725$. (b)Plot of average vertical (dashed) and horizontal (solid) temperature as a function of increasing and decreasing maximum acceleration (Γ) at 50 Hz, under isobaric conditions (W=4.5g) for $R = 3.5$

ratio of horizontal to vertical temperature (T_{HH}/T_{VV}) stays constant close to 50% above $\Gamma = 5$ [see Fig. 2.4]. This is in contrast to behavior of system at R=4, which shows clear evidence of first order phase transition.

We also perform experiments in which we gradually increase the number of particles from $R = 3$ to $R = 4$ rows. Typical plots are shown in Figs. 2.13(a)-(c) to illustrate the effect the number of particles on phase transition. For $R = 3$ rows we observe a first order phase transition with hysteresis. When we increase the number of rows to $R = 3.2$ or $R = 3.5$ the transition disappears and the density changes gradually with Γ. This behavior persists till $R < 3.7$. For $R = 3.7$ we observed a hint of discontinuity in the density, which tells us about the onset of phase transition. For $R = 3.8$, we see a small discontinuity with hysteresis. For $R = 4$ rows, as expected the system recovered the hysteretic phase transition behavior. For non integer number of rows R, we no longer have isobaric conditions across the cell in the crystalline phase. This is the result of few particles in the top row supporting the top weight and other particles experiencing no pressure of the weight. Also for non integer number of rows, sometimes the system just cannot get dense enough to reach the solidus point (ν_s). Thus for the hysteretic phase transition to occur, the number of particles should be commensurate with the cell size.

Another way to increase the system size is by keeping the number of rows constant but increasing the cell width. We now double the cell width to $L = 34.5D$ while keeping four rows of particles. This way, we maintain the same pressure conditions for both the small and big cell. In Fig. 2.14 we plot the volume fraction as a function of maximum acceleration for the big cell and small cell at 70Hz and under same pressure conditions ($M_R = 0.5$). The characteristic features of the first-order

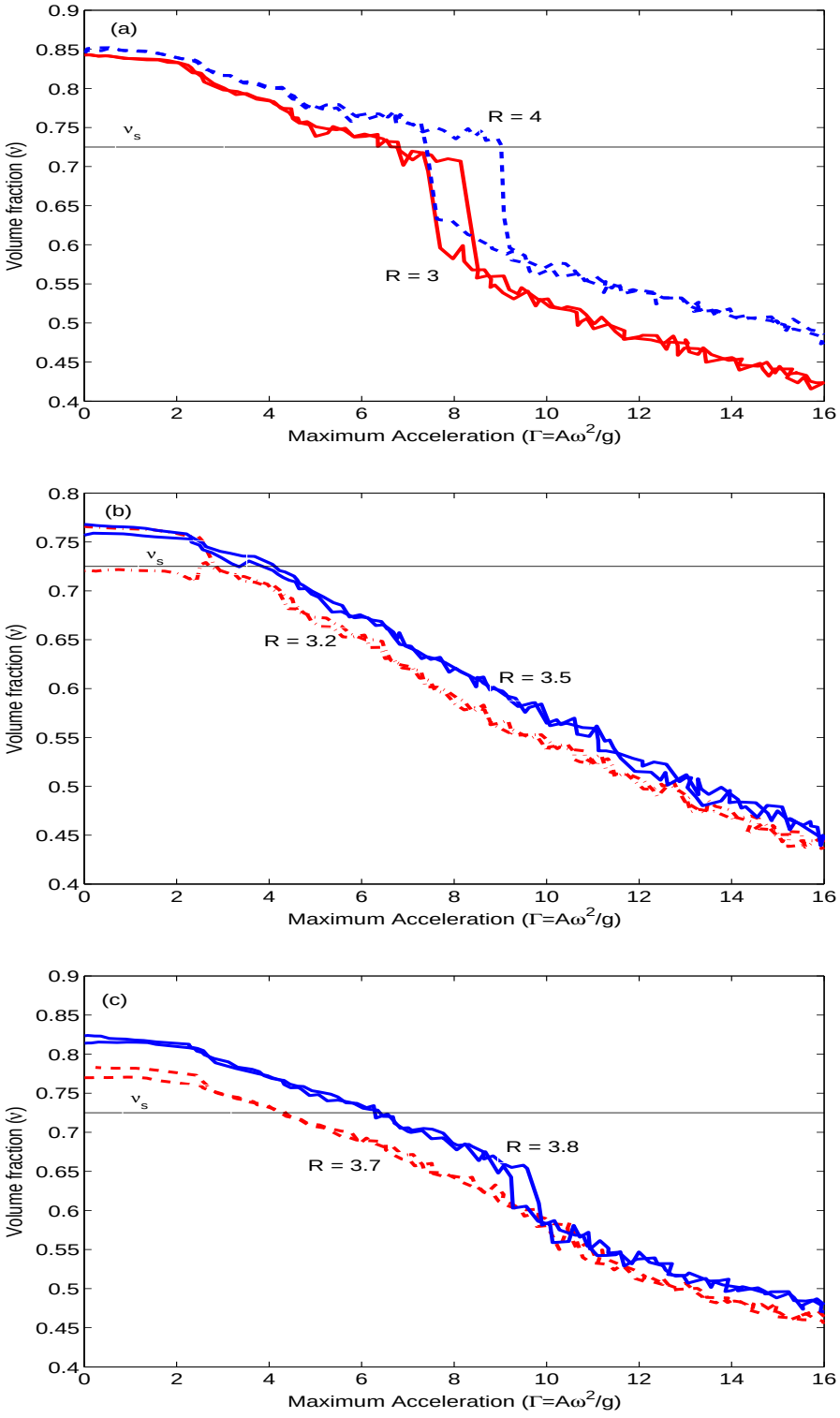

Figure 2.13: (a)Plot of volume fraction as a function of increasing and decreasing maximum acceleration (Γ) at 50 Hz, under isobaric conditions (top weight,W=4.5g) for (a) $R = 3$(thick) and $R = 4$ (dashed) ,(b) $R = 3.2$ (dashed) and $R = 3.5$ (thick) and (c) $R = 3.7$(dashed) and $R = 3.8$ (solid). The horizontal solid line in (a), (b) and (c) corresponds to the solidus point, $\nu_s = 0.725$.

phase transition are retained and are similar for both the systems. However, the transition point is shifted to higher Γ for the large cell and hysteresis loop is substantially bigger for the large cell as compared with the small cell loop. The increase in hysteresis loop on doubling the system size can be explained by the fact that the large cell system has a higher potential barrier for cross over between crystal and gas phases. This results in system getting locked in one of the phases contributing to the widening of the hysteresis loop.

Overall, the volume fraction is higher in the big cell. The difference in density between the two cells in the crystal phase is due to the empty spaces at the edges of the cell. Indeed, we chose to build the cell with a semi-integer length ($L = 17.5D$ or $34.5D$) which allows to create a triangular lattice. However, this arrangement leaves empty spaces of $0.5D$ at the edges of each row. These empty spaces are the same size for the big and small cell, so they represent a lower volume fraction for the big cell. We also observe that the gas phase density is significantly different for the big and small cell under similar conditions of driving. This is a surprising results since we expect the gas phase density to be the same for identical conditions of driving (energy injection).

We can account for the difference between the gas like steady state for the big and small cell in the following way: The primary reason for the variation is the difference in number of dissipative particle collisions for the two systems. Since we have a boundary heating system the energy is injected through the bottom boundary of the cell. The ratio between the number of heating events and the particle collision events is an important parameter governing the dynamics for such systems (van Zon & MacKintosh 2004). For the large system with boundary heating we expect a higher particle-particle collision event as compared to the small cell under similar conditions of energy injection. The higher number of dissipative particle collisions in the big cell lead to a gas like steady state with lower temperature or higher density

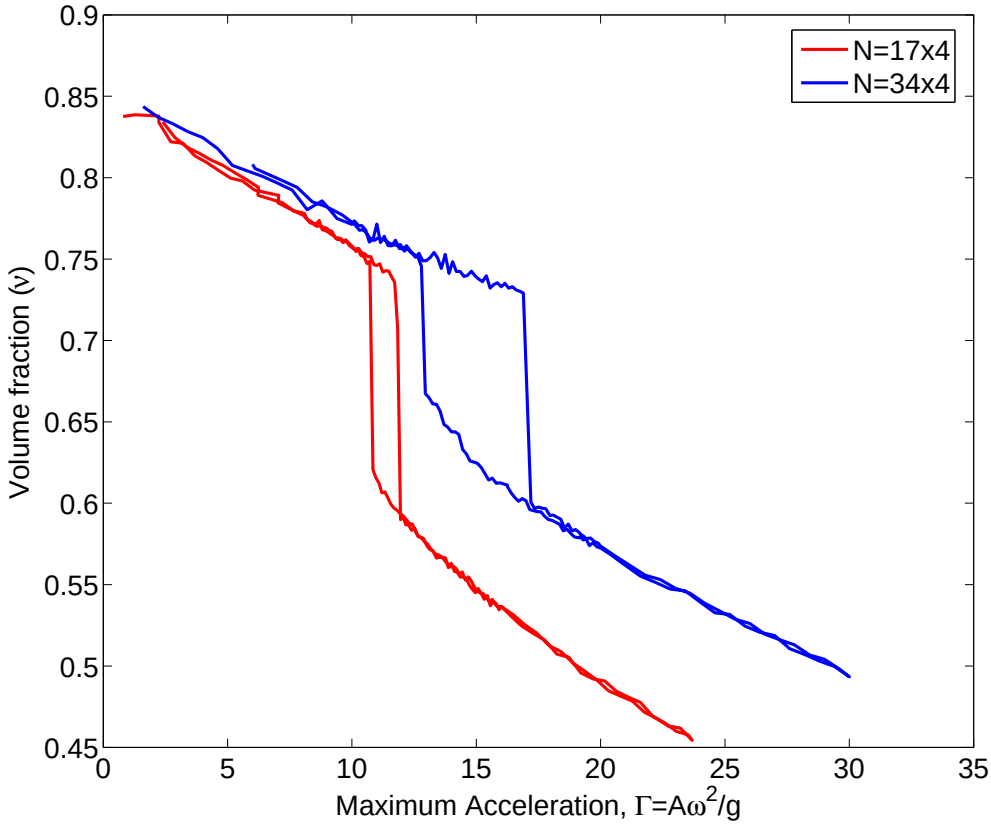

Figure 2.14: Plot of volume fraction as a function of increasing and decreasing maximum acceleration (Γ) for two different cell sizes: (a) $N = 68$, $R = 4$, M_R=0.5, $L = 17.5D$; (b) $N = 136$, $R = 4$, M_R=0.5, $L = 34.5D$. The driving frequency is set to, f=70Hz and the time delay is, τ=10s for both the data sets.

as compared to the small cell dynamics.

2.9.2 Phase transition in 3D isobaric system

Next, we explore the phase transition behavior in a three-dimensional isobaric system. We place spherical stainless steel ball bearing ($D = 3.175mm$) in a three-dimensional (3D) cell of dimensions 1"x 1"x 2". The walls of the container are made from plexiglass. We begin with a crystalline arrangement of three rows ($R = 3$) of particles. The bottom layer has 68 particles which are arranged in a hexagonal closed pack manner. The second is built upon the first layer of particles and is

composed of 56 particles, while the 3rd layer has 68 particles. The bottom plunger is rectangular in shape with dimensions 0.989"x 0.989"x 0.5", and is connected to the shaker with a rigid rod arrangement. The plunger oscillates sinusoidally and provides the necessary vibrational excitation to the system. The top weight is rectangular in shape (dimensions: 0.989"x 0.989"x 0.5", weight $M = 21$g) and floats on top of the particles in the 3D cell. Again, the top weight is free to move in the vertical direction and allows for the volume/density fluctuations. The camera is positioned to capture the side view of the cell. In quasi-two dimensional system we can use direct imaging to track all the particles. In the 3D set up we cannot track all the individual particles trajectories. However, with our current arrangement we can find the position of the top and bottom of the cell and hence determine the density/volume of the system.

In Fig. 2.15, we plot the volume fraction for the 3D isobaric system as a function of the driving acceleration. We clearly find a discontinuity in density and hysteresis analogous to that found for experiments with two-dimensional system. The crystal to gas transition takes place around $\Gamma = 10$, while the gas to crystal transition is at $\Gamma = 8.3$. The system does not completely return back to its initial crystalline arrangement which may be attributed to the defects in the final crystal at the end of the crystallization process. Due to the limitations of the current set up we cannot say anything definitive about the particle-particle arrangement during the phase transition process. Nevertheless, this is clearly an important result because it shows that the phase transition characteristics observed and quantified for 2D system do persist in 3D arrangement and are very robust in nature. In future, we would like to carry out extensive experiments with the 3D set up to look into the phase transition phenomena in more detail.

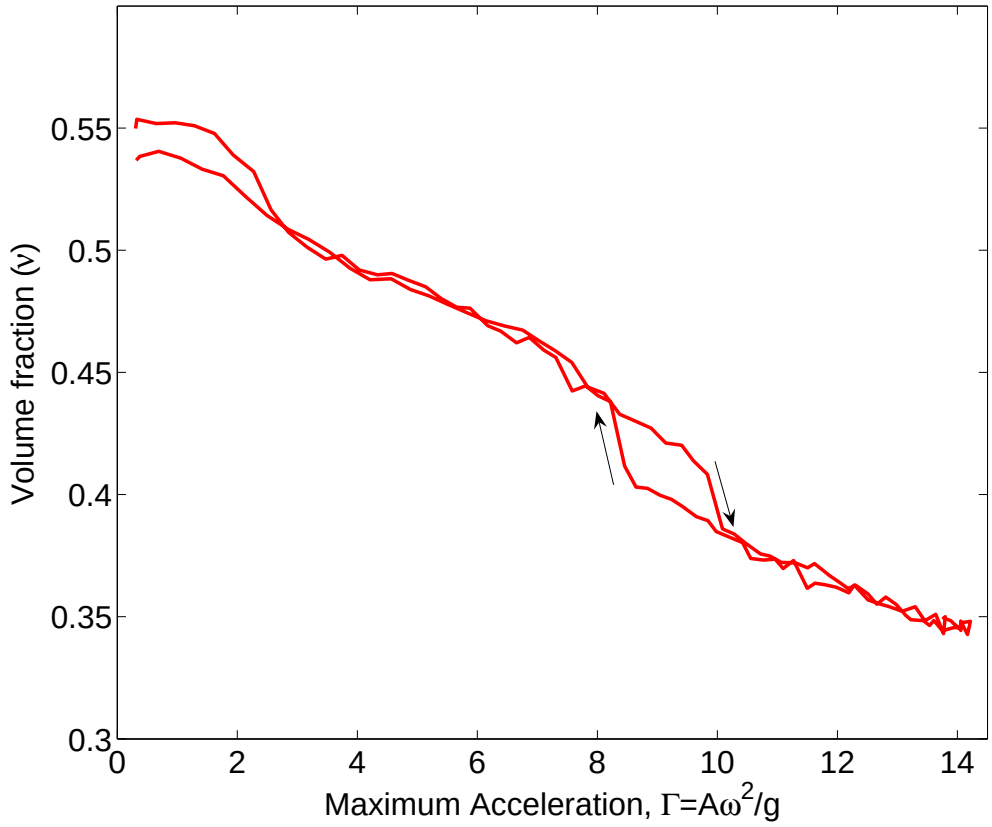

Figure 2.15: Plot of volume fraction as a function of increasing and decreasing maximum acceleration (Γ) for $R = 3$, using the three-dimensional isobaric arrangement. We use a total of $N = 192$ particles (total mass of particles is 25.4g) in the 3D cell and the mass of top weight is approximately $M = 21$g which gives mass ratio M_R=0.83.

2.10 Summary

In this chapter, we have presented experimental evidence of a first order freezing/melting phase transition in a non-equilibrium system. The first-order phase transition seen here in the two-dimensional dissipative granular system is qualitatively different from that of an elastic hard sphere system. In such a system, just as in an ordinary gas, at the phase transition there is a discontinuous change in the density, but the temperature would be unchanged. This is a unique feature in granular systems since it suggests that there is the possibility of steady states

in which two phases co-exist, but at different nonzero temperatures. We also observe that higher pressures and higher driving frequencies delay the onset of phase transition from crystalline to a gas phase. In addition the phase transition also exhibits hysteretic behavior (history dependence). This indicates that the system properties are sensitive to rate of change of control parameter, Γ. We also find that the observed phase transition shows system size dependence. For non integer R, the system properties show gradual change with no evidence of discontinuity/phase transition, which contrasts the behavior of the system for integer number of rows. However, on doubling the system size with integer number of rows, we observe the characteristic features of a first-order phase transition are retained. Our preliminary investigations in a 3D cell arrangement further support the robustness of the observed phenomena.

Further, phase transitions in equilibrium systems are usually explained by entropy maximization or free energy minimization concepts. However, such formalism is absent for non-equilibrium phase transition studies which seriously undermines their fundamental understanding. Despite these limitations, our phenomenological model results strongly suggest that the observed phase transition can be explained by entropiclike arguments, which is a crucial step towards advancing our current understanding of non-equilibrium phase transitions.

Chapter 3

Crystallization of an isochoric granular fluid

In this chapter we report experimental investigation of the crystallization transition of a uniformly heated quasi-2D granular fluid as a function of filling fraction. We employ a variety of measures to quantify the dynamics and structure of our non-equilibrium granular fluid. Our experimental results for the Lindemann criterion for melting, the radial distribution function, the bond order parameter and the statistics of topological changes at the particle level show remarkably good agreement with the behavior of equilibrium hard disks (Reis, Ingale & Shattuck 2006).

3.1 Introduction

Equilibrium statistical mechanics is generally not applicable to systems where both energy input and dissipation mechanisms are present. Identifying relevant tools for understanding far from equilibrium systems poses a serious challenge to the scientific community (Egolf 2000). Granular materials have become a canonical system to explore such ideas since they are inherently dissipative due to inter-particle frictional contacts and inelastic collisions. In addition to being of fundamental interest, granular materials have also far reaching practical importance since they are routinely produced and processed in a number of industries where, however, accumulated

ad-hoc knowledge is often the most used tool (Ennis, Green & Davies 1994). The dissipative nature of grains means that any dynamical study requires energy injection, typically involving vibration or shear (Melo et al. 1994, Prevost, Egolf & Urbach 1996). An important feature of this class of systems is that the driving and dissipation mechanisms can be made to balance such that a steady state is achieved. Recent investigation of such *Non-equilibrium Steady States* have shown that connections with equilibrium statistical mechanics may provide an useful analogy. For example, a single particle on a turbulent air flow has been shown to exhibit equilibrium-like dynamics (Ojha, Lemieux, Dixon, Liu & Durian 2004) and the nature of the melting phase transition in two-dimensional granular system appears to be consistent with the Kosterlitz-Thouless- Halperin-Nelson-Young (KTHNY) scenario for melting of equilibrium 2D crystals (Olafsen & Urbach 2005).

In our study we have developed an experimental system to generate a vibrated quasi-two dimensional granular fluid of stainless steel spheres that is *uniformly heated*, i.e. energy is injected into the granular layer in a spatially homogeneous manner. At low filling fraction we observe a disordered dense fluid regime; where there is a high collisional rate and at long times the particles randomly diffuse across the cell. At high filling fraction the behavior of the system is quite different as each sphere orders into an hexagonally packed arrangement, becoming locked by its six neighbors, and the system is said to be *crystallized*. In this chapter we analyze this fluid-to-crystal transition as the filling fraction of our quasi-2D granular fluid is increased. The aim of our study is two-fold. Firstly, we make a quantitative characterization of the structural changes in the granular layer across this transition using a number of classic measures, namely the Lindemann criterion for melting, the radial distribution function and the bond order parameter. Moreover, we apply the novel concept of *shape factor*, recently introduced by Moucka and Nezbeda (Moucka & Nezbeda 2005), to measure in detail the topology of the Voronoi cells across the

crystallization transition. In parallel, we establish a direct comparison between the behavior of our system and that of equilibrium hard disks and test the extent to which the above quantities, commonly used in equilibrium systems, can can be used to study a non-equilibrium system such as ours.

3.2 Experimental apparatus

The experimental apparatus is analogous to that discussed in Section 2.2. The main difference is the geometry of the cell employed for the study. A schematic diagram of the front view of the apparatus is presented in Fig. 3.1. The cell was cylindrical in shape with $10.16cm$ diameter. The experimental technique consisted of vertically vibrating an ensemble of steel spheres of diameter, $D = 1.191mm$, confined in a gap sandwiched between two horizontal glass plates. The gap between the two plates was made to be $1.6D$ in order to constrain the system to be quasi-two dimensional. As a result of the gap the two-dimensional projection of the spheres may overlap even if they are not touching. The maximum overlap of any two spheres is 20% as shown in Fig. 3.1. The spheres were confined from the sides by a $1.6D$ thick stainless steel annulus. For the top plate, we used on optically flat glass plate whose surface was coated with a thin and transparent, conducting layer of ITO to eliminate electrostatic effects. The surface of the bottom glass plate was made rough by sand-blasting with structures on length scales of the order of $100\mu m$ to $500\mu m$.

The horizontal experimental cell was vertically vibrated, sinusoidally, via an electromagnetic shaker (VG100-6 Vibration Test System). The connection of the shaker to the cell was done via a robust rectangular linear air-bearing which constrained the motion to be unidirectional. The air-bearing ensured filtering of undesirable harmonics and non-vertical vibrations due to its high stiffness provided by high-pressure air flow in between the bearing surfaces. Moreover, the coupling between the air-bearing and the shaker consisted of a thin brass rod ($25.4mm$ long and $1.6mm$

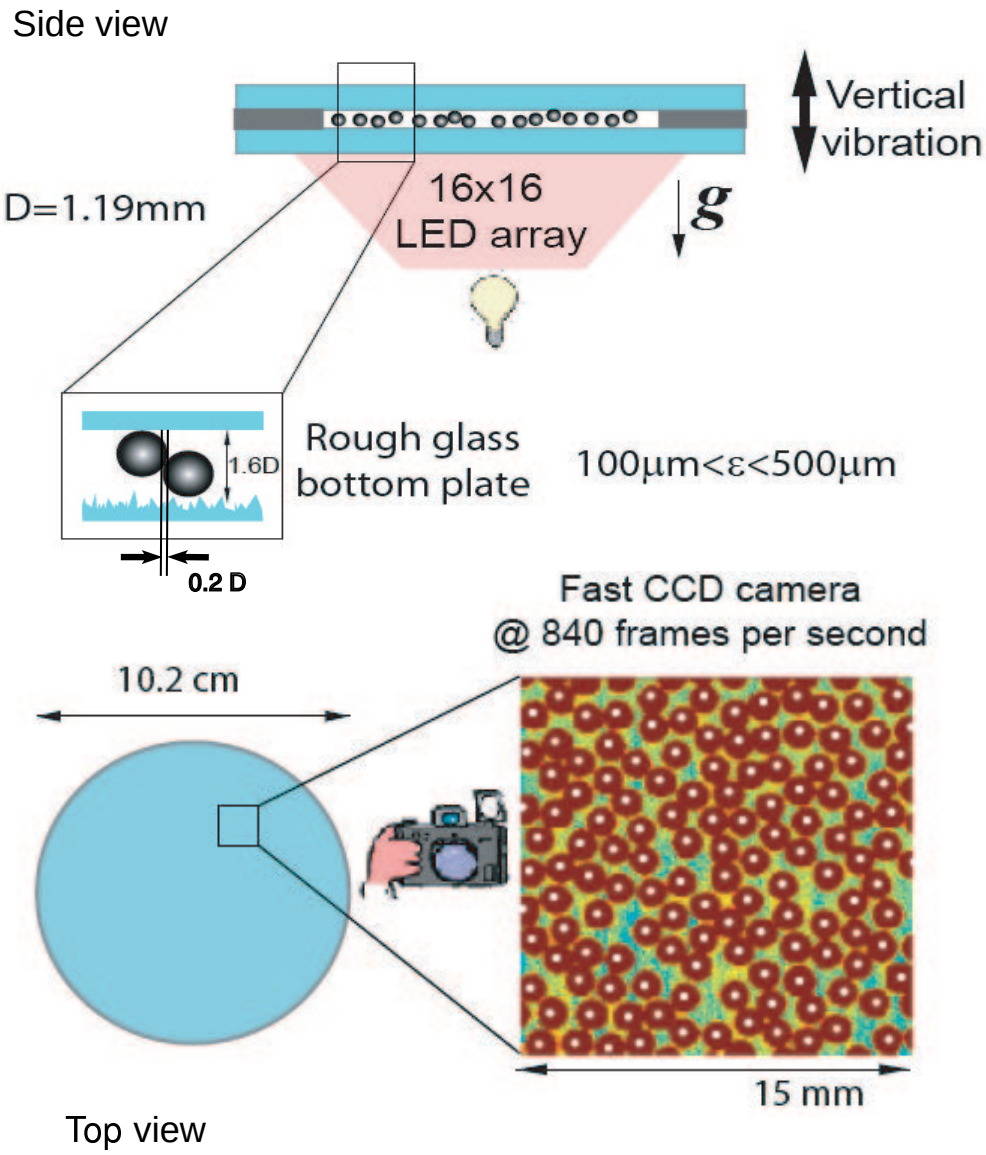

Figure 3.1: Schematic diagram of the experimental setup: side view and top view

diameter). This rod could slightly flex to correct any misalignment present in the shaker/bearing system, while being sufficiently rigid in the vertical direction to fully transmit the motion. This ensemble – shaker/brass rod/air-bearing – ensured a high precision vertical oscillatory driving.

Using this arrangement, at each cycle of the driving, the velocity of each particle was randomized as it collided with the various peaks and valleys of the rough glass plate thereby achieving homogeneous random heating. Moreover the randomization due to the rough plate minimized gravity induced rolling making our system less prone to effects due to gravity. The system was set to be horizontal using precision micrometer levelling screws in order to eliminate density inhomogeneity effects. In addition, we used an air bearing arrangement to damp out unwanted mechanical vibration.

We focused on a small imaging window, $15mm \times 15mm$, of the full cell and acquired digital videos with a fast Charged Coupled Device (CCD) camera at 840 or 480 frames per second [see top view of Fig. 3.1] . We used a high intensity Light emitting diode (LED) light source for providing the necessary illumination. The LED's were mounted on an printed circuit board (PCB) in a 16 x 16 array configuration and placed below the cell. This arrangement allowed us to capture all the images in transmission mode, where particles obstruct the light emitted by the light source and appear as dark circles in a bright background.

3.3 Experimental parameters and procedure

The experimental parameters of our system are: the driving frequency f, the dimensionless acceleration $\Gamma = A(2\pi f^2)/g$, the filling fraction ϕ of particles and the cell gap height (H) . For the results presented in this chapter we kept the driving frequency $(f = 50Hz)$ and dimensionless acceleration constant, $(\Gamma = 4)$, but varied the filling fraction, ϕ, i.e., the density of the particles. For each filling fraction (ϕ),

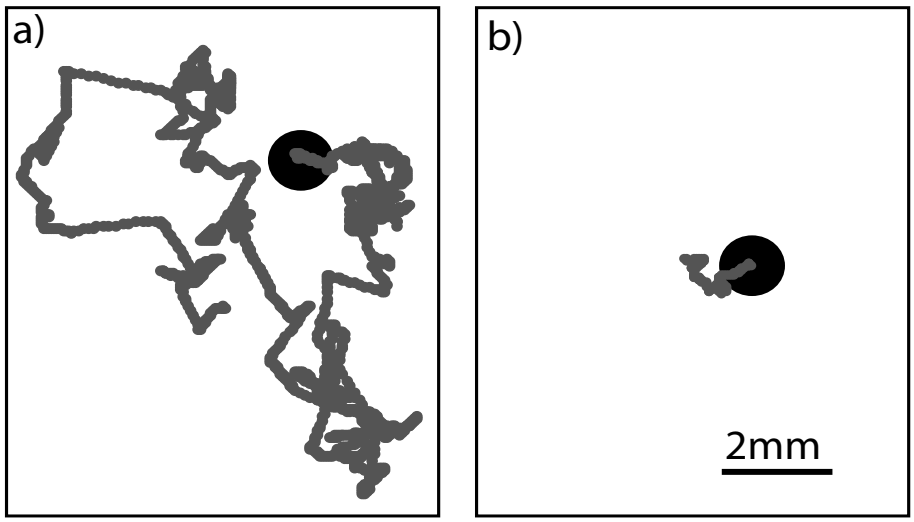

Figure 3.2: Experimental frames showing single particle trajectories using (a) Rough bottom plate and (b) Flat bottom plate for driving, at fixed forcing of $\Gamma = 4$ and $f = 50Hz$.

we start by placing appropriate amount of particles in the cell. For every run, we begin by compacting the particles to form a nice hexagonal lattice structure with more or less no defects. Thus we ensure the same starting arrangement of the particles for all ϕ. Then, we mount the cell on the shaker and ensure proper levelling of the apparatus. We then start vibrating the cell at desired Γ (an accelerometer is mounted on the cell to measure the driving acceleration). We wait till the system reaches a steady state before taking pictures (typically 4 minutes). Once the system is in steady state we capture an image sequence (8192 frames) at frame rates of 480 or 840 frames per second. The image sequence is recorded and stored for image analysis using custom made Matlab programs.

Fig. 3.2 shows a typical trajectory of a single particle in the cell using a rough bottom plate and a flat bottom plate for driving. We see that the motion of the particle is clearly randomized (random walk) by the the rough bottom plate and is considerably more effective than the flat bottom plate driving. Thus we perform our experiments using a rough bottom plate to uniformly heat the granular particles. In Fig. 3.3 we present typical experimental frames at three different filling fractions

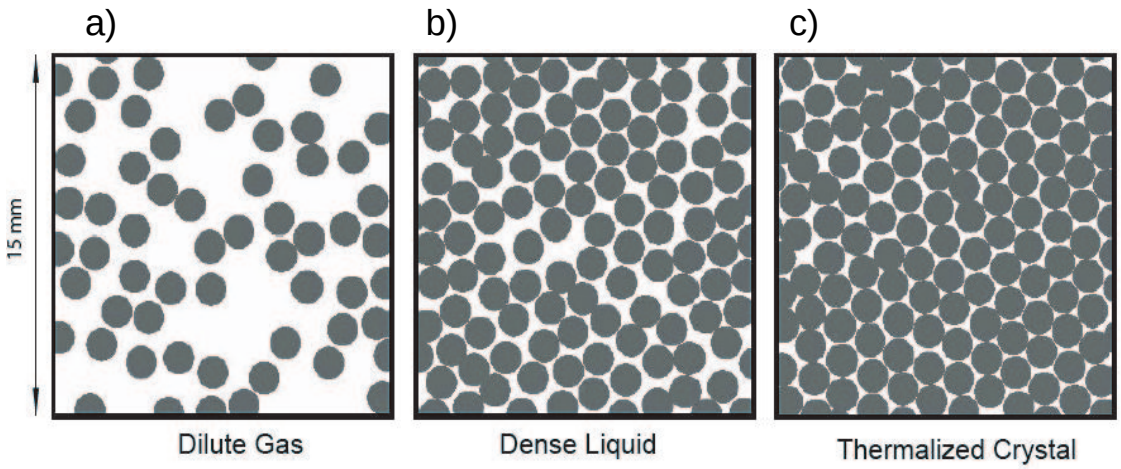

Figure 3.3: Experimental frames for three different filling fractions(ϕ): (a) Dilute gas ($\phi = 34$) (b) Dense fluid ($\phi = 0.67$) (c) Thermalized crystal ($\phi = 0.8$), at fixed forcing of $\Gamma = 4$ and $f = 50Hz$.

(ϕ) of 0.34, 0.67 and 0.80. For $\phi = 0.34$ we observe a dilute gas phase, in which particles move randomly and undergo instantaneous collisions. For $\phi = 0.67$, we get a dense fluid like phase, in which the particle motion is severely restricted. For still higher filling fractions of $\phi = 0.8$, we obtain a thermalized crystal, where the particles vibrate energetically about their hexagonal lattice sites.

3.4 Lindemann Criterion

The first measure that we employ to address the qualitative change in behavior between dense fluid and crystalized phases, as ϕ is increased, is the the Lindemann criterion. Lindemann criterion is one of the classical measure for melting of solids (Lindemann 1910). Lindemann put forward an idea that a solid melts when the vibrational amplitude of its constituent atoms reached some critical magnitude, such as 10% to 15% of its interatomic spacing. Lindemann criterion is based on empirical rules and presents a simplified picture of melting of a solid at the atomic level. The Lindemann ratio,γ_m is defined as follows,

$$\gamma_m = \frac{\sqrt{< (\overrightarrow{r} - < \overrightarrow{r} >)^2 >}}{L} \tag{3.1}$$

where $\overrightarrow{r}$ is the positional vector of the particles and L is the bond length, i.e. the average lattice spacing. Thus the value of γ_m gives the ratio of average root mean squared particle displacements to the average separation distance between the particles, L.

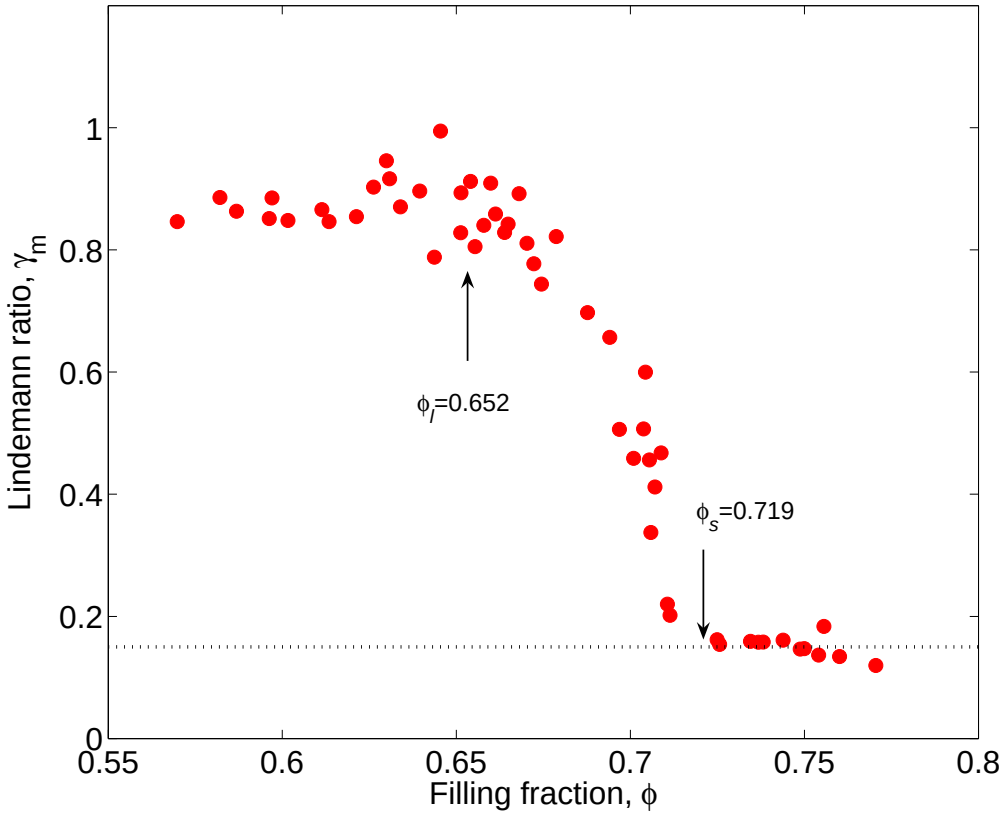

Figure 3.4: Lindemanmn ratio, γ_m, v.s. filling fraction, ϕ, for a granular layer vibrated at $f = 50Hz$ and $\Gamma = 4$. The dotted horizontal line is located at $\gamma_m = 0.15$. Crystallization occurs at $\phi_s = 0.719$.

In Fig. 3.4 the Lindemann ratio, γ_m, is plotted at high values of ϕ. In the range $0.652 < \phi < 0.719$ a sharp drop in γ_m is observed and above $\phi > 0.719$, the Lindemann ratio becomes approximately constant below $\gamma_c \sim 0.15$. Following the above definition, this suggests that at $\phi_s = 0.719$ the system freezes, which is in excellent agreement with the crystallization point, also known as *solidus point*, for

equilibrium hard disks: $\phi_s^{sim} = 0.716$ (Alder & Wainwright 1962)(Mitus, Weber & Marx 1997).

The Lindemann criterion is, however, empirical and says little about the corresponding structural configuration. To address this issue we use another measure, the radial distribution function, to study the structure of the system in the following section.

3.5 Radial Distribution function

The radial distribution function, $g(r)$, is an example of a pair correlation function, which is the most common and effective way of describing the average structure of molecular systems (Chaikin 1995). $g(r)$ is the normalized probability of finding a particle as a function of distance from the center of a test particle. Hence, $g(r)dr$ yields the number of particles to be found in the shell bound by r and $r+dr$, normalized by the number of particles that would be expected for a uniform distribution of particle positions.

In Fig. 3.5(a) we plot curves of $g(r)$ for various representative values of ϕ. For low filling fractions, *e.g.* $\phi = 0.5$, we observe fluid-like behavior and $g(r)$ is peaked at r/D =1, 2 and 3, as is commonly seen in hard sphere fluids (Bernal 1964, Chaikin 1995). With increasing ϕ, *e.g.* $\phi = 0.65$, $g(r)$ develops an additional shoulder below the $r/D = 2$ peak, which eventually evolves into a distinct peak located at $r/D = \sqrt{3}$. The location of this secondary peak is significant of hexagonally packed arrangements (as seen in the curves for $\phi = 0.7$ and $\phi = 0.72$). To each $g(r)$ experimental curve in Fig. 3.5(a), we have superposed a corresponding (dashed) curve from a Monte Carlo simulation of equilibrium hard disks recently reported by Moucka and Nezbeda (Moucka & Nezbeda 2005), for identical values of ϕ. The agreement between the experimental and numerical curves is remarkable, implying

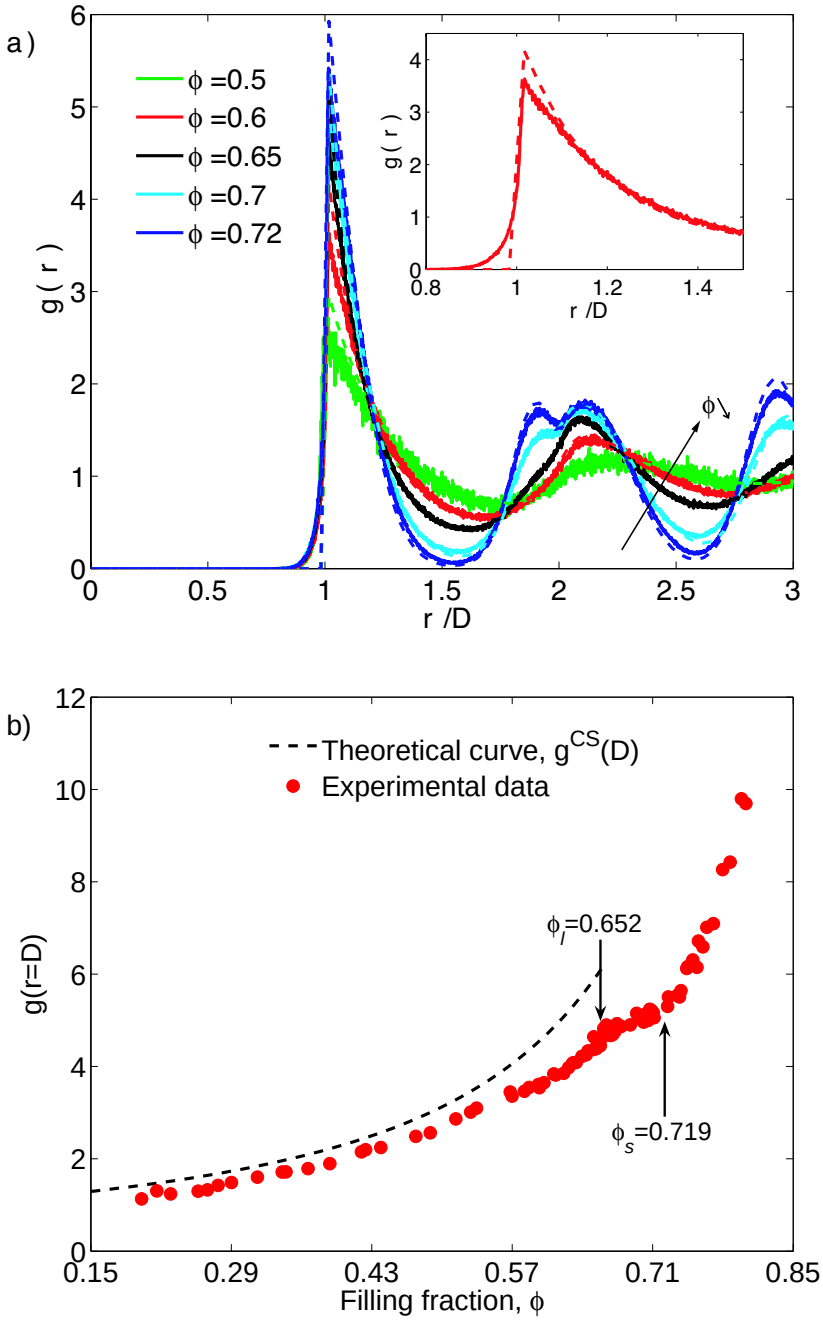

Figure 3.5: (a) Experimental (solid) and numerical (dashed, extracted from Moucka and Nezbeda (2005)) curves of the radial distribution functions for 5 values of ϕ. The arrow points in the direction of decreasing ϕ. Inset: Section of $g(r)$ curve for $\phi = 0.6$. (b) Radial distribution function at contact, $g(r = D)$ v.s. filling fraction. The dashed line corresponds to the theoretical Carnahan-Starling equation. ϕ_l and ϕ_s are the fluidus and solidus points, respectively.

that our experimental non-equilibrium granular fluid is adopting structural configurations identical to those one would expect for hard disks. Some deviations exist but mostly near $r/D = 1$, where the system is most sensitive. To look at these in detail we have plotted the value of $g(r = D)$, i.e. at contact, which corresponds to the absolute maximum of $g(r)$. For low filling fractions and up to $\phi \sim 0.57$, $g(D)$ follows the theoretical curve of Carnahan-Starling, $g^{CS}(D) = [16 - 7\phi]/[16(1 - \phi)^2]$, which is usually assumed in the kinetic theory equation of state for granular gases (Carnahan & Starling 1969). Within this region, the fact that g(D) is systematically lower than $g^{CS}(D)$ by $\sim$ %14 may be attributed to the fact that our experimental system is quasi-2D (rather than perfectly 2D as assumed in both the theory and simulations). This can be clearly observed in the inset of Fig. 3.5(a). Note that for perfect hard disks $g(0 < r < D) = 0$, which is the case for the simulations curves. For $\phi > 0.57$ the deviations from $g^{cs}(D)$ increase up to $\phi = 0.652$ where there is a discontinuity in the curve's slope. For $0.652 < \phi < 0.719$ there is a period of slower growth of $g(D)$ with ϕ. This is consistent with the scenario of the existence of a fluid phase ($\phi < 0.652$), intermediate/transition phase ($0.652 < \phi < 0.719$) and crystal phase ($\phi > 0.719$).

3.6 Bond order parameter

In addition to the development of correlations in the particle positions, angular correlations also arise as ϕ is increased (Nelson & Halperin 1979, Jaster 1999). These can be measured by the (global) bond-orientational order parameter defined as $\psi_6^{global} = |1/M \sum_{i=1}^{M} 1/N_i \sum_{j=1}^{N_i} e^{i6\theta_{ij}}|$, where M is the number of particles in the observation window, θ_{ij} is the angle between the particles i and j and an arbitrary but fixed reference axis and N_i is the number of nearest neighbors of particle i, found using the Voronoi construction (Fraser, Zuckerman & Mouritzen 1990). In Fig. 3.6 we plot the dependence of ψ_6^{global} on ϕ. The value of the bond orientational

order parameter should tend to unity in the crystal phase since $n\pi/3$ angles prevail, where $n = 1, 2, ..., 5, 6$. On the other hand, $\psi_6^{global} \ll 1$ for a disordered phase.

In Fig. 3.6 three different regions can be identified based on (the slope of) the values of ψ_6 , as was the case with $g(D)$, and with the same *phase boundaries*: $\phi_l = 0.652$ (fluidus point) and $\phi_s = 0.719$ (solidus point). The observed behavior is consistent with the two-step continuous phase transition observed during equilibrium $2D$ crystallization (Nelson & Halperin 1979, Jaster 1999), where the first transition transforms the isotropic fluid phase into an hexatic phase with long range orientational ordering but no positional ordering and the second transforms the hexatic phase into a crystal with both long range orientational and positional order.

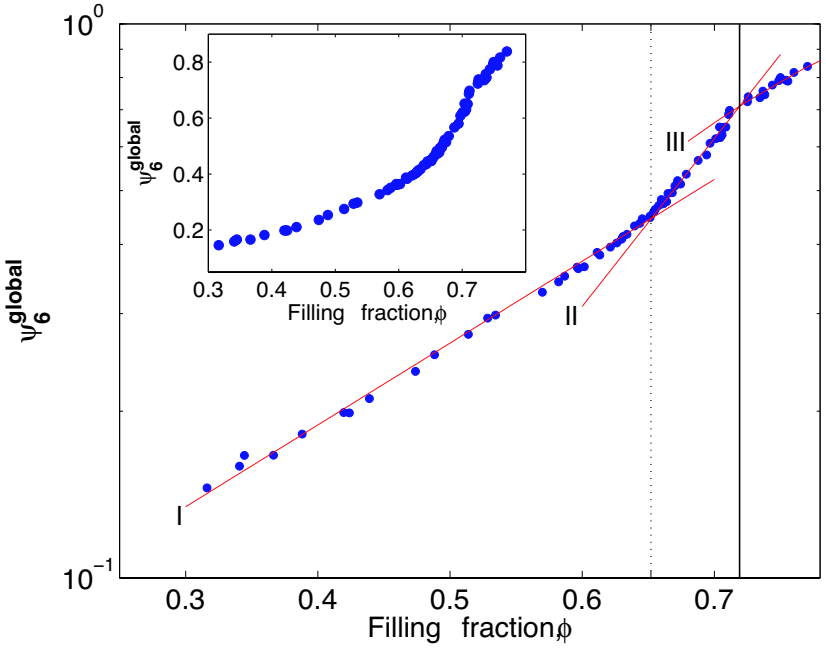

Figure 3.6: Semi-logarithmic plot of the bond-orientational order parameter, ψ_6. The first two lines, I and II, are least squares fits of the form $\psi \sim \exp[A\phi]$ and line III is a linear fit of the form $\psi \sim A\phi$. The dashed and solid vertical lines are located at $\phi_l = 0.652$ and $\phi_s = 0.719$, respectively. Inset: Linear version of the plot.

3.7 Shape factor concept

For quantitative characterization of the structural changes in the transition to crystalline phase; a novel concept using shape factor was recently put forward by Moucka & Nezbeda (2005). This method employs Voronoi tessellation accompanied by a certain shape factor of Voronoi polygons denoted by ζ. Details about the Voronoi tessellation are given in Appendix A. To characterize the Voronoi cells we define the shape factor as

$$\zeta = \frac{C^2}{4\pi S} \tag{3.2}$$

where C is the circumference of the Voronoi cell, i.e., total length of its edges, and S is the surface area of the Voronoi cell. For circles $\zeta = 1$ and for all other shapes $\zeta > 1$. For a square $\zeta = 1.273$, for regular pentagons $\zeta = 1.156$, and for regular hexagons $\zeta = 1.103$. We note that, the Voronoi cell of each particle has an associated numerical value of ζ.

In Fig. 3.7(a) we present a surface plot of the distribution of shape factor, $P(\zeta, \phi)$. At low ϕ, P(ζ) exhibits a broad and flat maximum; the particles are randomly distributed and no specific type of cells are formed. As ϕ is increased, P(ζ) becomes increasingly localized around the maximum which progressively moves towards lower values of ζ. Eventually, for $\phi > 0.65$ the distribution becomes bimodal and a distinct second maximum appears. In the vicinity of the crystallization point $\phi_s = 0.719$ the original maximum for high ζ values disappears while the low ζ maximum, centered at $\zeta \approx 1.1$, rises sharply. Note that for a perfect hexagonal packing, one would expect a delta function located at $\zeta = 6/\sqrt{3\pi^2}$ (the value for regular hexagons). Vertical cross-sections of the experimental $P(\zeta, \phi)$ distribution along representative values of ϕ are presented in Fig. 3.7(b). We have also superposed the corresponding numerical (dashed lines) data of Monte Carlo of equilibrium hard disks (Moucka & Nezbeda 2005), for the same values of ϕ, and find that our

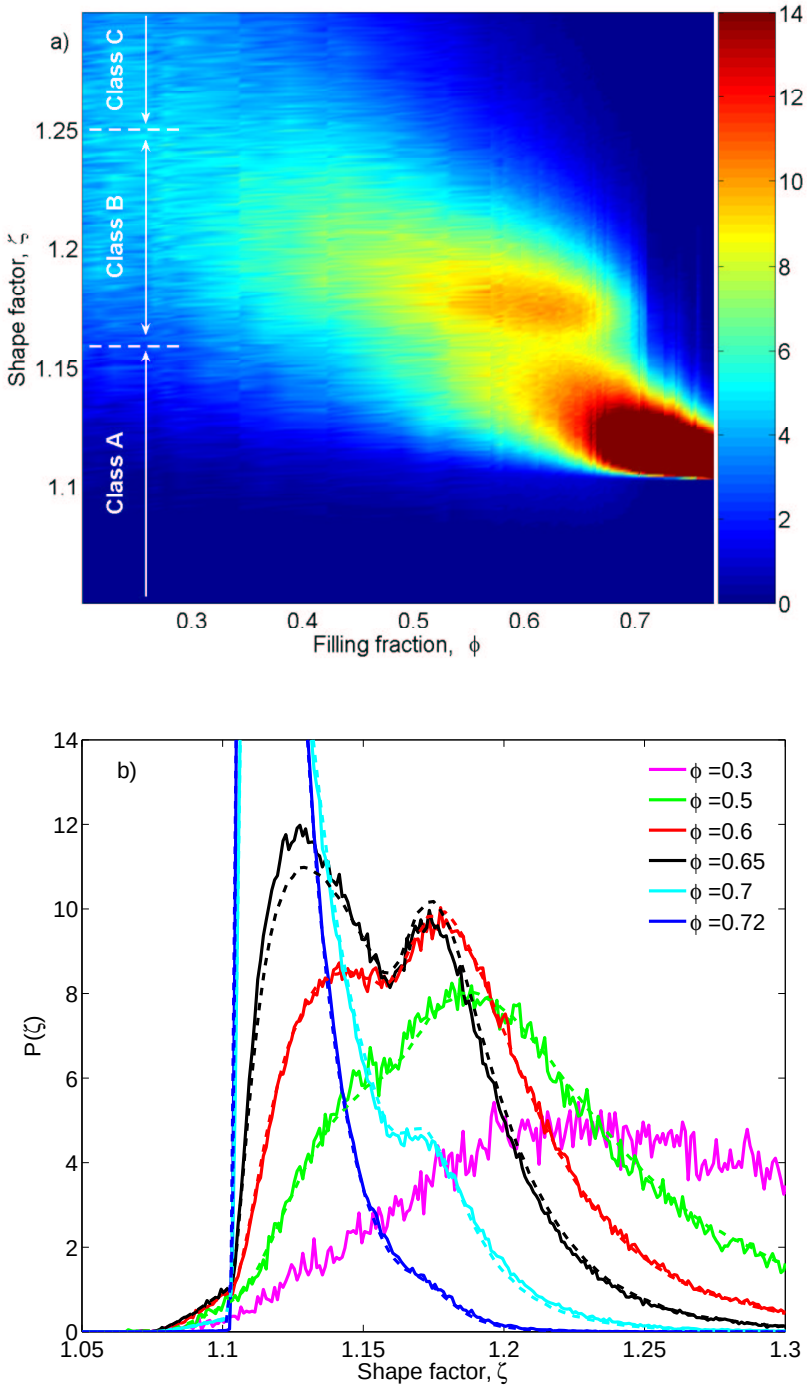

Figure 3.7: (a) Surface plot for the probability distribution functions of shape factor, $P(\zeta, \phi)$. The value PDF is given by the adjacent color bar. The two horizontal dashed lines located at $\zeta = 1.159$ and $\zeta = 1.25$ are the boundaries of classes, A, B and C of the Voronoi cells, as defined in the text. (b) Experimental (solid) and numerical (dashed, extracted from Moucka and Nezbeda (2005)) vertical cross-sections of the $P(\zeta, \phi)$ distribution along 5 values of ϕ The arrow points in the direction of decreasing ϕ.

experimental results are in excellent agreement with the numerical simulations.

We now follow the classification scheme of the Voronoi cells proposed by Moucka and Nezbeda, as follows. An important point to note is that the location of the minimum of $P(\zeta)$, where it exists, is only marginally dependent on ϕ and hence we set $\zeta_{min} = 1.159$. *Class A* consists of particles with $\zeta < \zeta_{min}$. *Class B* particles have $\zeta_{min} < \zeta < \zeta_u$ and *Class C* have $\zeta > \zeta_u$ where $\zeta_u = 1.25$. The value for the upper bound, ζ_u, is set such that at the filling fraction for which both maxima of $P(\zeta)$ have equal heights ($\phi \approx 0.65$), the number of particles in classes A and B are the same. These boundaries of cell classes have also been plotted in the surface plot of Fig. 3.7(a).

In Fig. 3.7(c) we present the ϕ-dependence of the fraction of particles belonging to each of the Classes A, B and C. The nature of the previously mentioned special filling fraction values of ϕ_l and ϕ_s, that separate the disordered fluid, the intermediate/transition phase and the crystal phases, becomes remarkably clear under this classification. ϕ_l is the point at which Class A and Class B occurs in the same proportions (the fraction of Class C is negligible at this point). ϕ_s is the point for which the fraction of Class B has sharply dropped to zero and the granular layer consists almost entirely of particle whose Voronoi cells are regular hexagons, i.e. crystallization occurs. It remains to be shown if the intermediate phase between ϕ_l and ϕ_s is simply a coexistence regions as suggested by the lever-like dependence of the fraction of Classes A and B or, instead, this is an hexatic phase with algebraically decaying orientational order (Olafsen & Urbach 2005). One would need to perform the experiments with a considerably larger imaging window to have sufficient spacial extension to properly test such scalings.

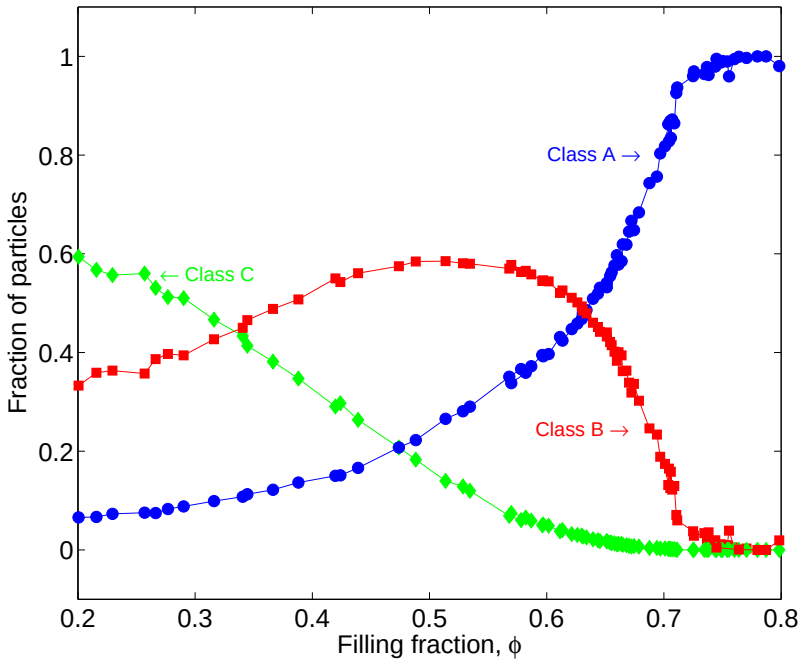

Figure 3.8: Fraction of particles in the A, B and C classes, as defined in the text, as a function of filling fraction.

3.8 Summary

In summary, we have reported detailed experimental measures of structural changes during the crystallization transition in a homogeneously heated granular fluid. Our results are in excellent quantitative agreement with Monte Carlo simulations for the crystallization of equilibrium hard disks. It is surprising that the particles in our granular layer adopt equilibrium like structural configurations even though the system is both driven and dissipative, i.e., far from equilibrium. We believe that the principal ingredients that allow us to establish such a direct analogy are the homogeneity and uniformity of the energy injection along with the importance of geometrical effects. The equilibrium structural configurations for hard disks are usually determined by an entropy maximization argument (Kawamura 1979). Whether we are able to explain the observed phase transitions in our system with entropiclike

arguments similar to those used in hard sphere systems is an important question which arises from our study and needs further investigation.

Chapter 4

Geometrical mechanism for solid-fluid transition

In this chapter we report a novel geometrical mechanism for solid-fluid phase transition in a uniformly heated quasi-2D granular system. In particular, we refer to the bond-order parameter, the bond length and bond angle distribution to identify the underlying topology of the granular fluid. The packing constraints in our quasi-2D granular fluid give rise to a geometrical structure resembling plane tilings composed of closed packed squares and triangles (ST Tilings).

4.1 Introduction

The experimental results from Chapter 3 suggest that the study of equilibrium systems can be effectively applied to study nonequilibrium steady states such as those found in our driven and dissipative granular system. An important question which arises from the analysis in Chapter 3 is, can we explain the observed phase transition in our uniformly heated isochoric non-equilibrium system with entropic/free energy like arguments similar to those used in equilibrium hard sphere/disk systems (Kawamura 1979). In this chapter we attempt to answer this question and investigate what other results from statistical study of equilibrium liquids and dense gases may be of relevance for studying the mechanics of granular materials.

4.2 Geometrical models for $2D$ melting

A variety of theoretical models have been proposed in the literature for explaining the $2D$ melting transition based on simple geometrical arguments (Collins 1964, Kawamura 1979, Kawamura 1983). A geometrical theory was first proposed by Bernal (1964) for simple monoatomic liquids. Bernal (1964) suggested that the important difference between the solid and the fluid state is the intrinsic irregularity of the fluid. Specifically, a fluid has only short range order and no long range order. The fluid state has no lattice order at any range. This irregularity of a fluid is considered most difficult to specify and yet the most fundamental property of a fluid.

Based on Bernal's idea Collins (1964) presented a simplified two-dimensional model for the melting transition. In this model, the 2D topology is composed of closed-packed squares and equilateral triangles in various proportions. This gives a good picture for both the liquid and the solid state if the ratio between the number of squares and equilateral triangles in properly chosen. If all the polygons in the topology are triangles, then the lattice is a usual triangular lattice with hexagonal closed packed configuration and corresponds to a solid state (e.g Fig. 4.1(a)). When squares are mixed in some finite proportion, the lattice loses its long range order without changing the nearest neighbor distance which corresponds to a fluid state as observed in Fig, 4.1(b).

Subsequent work by Kawamura (1979) resulted in further refinement of the Collin's model. Kawamura (1979) proposed a square-triangular tiling model which takes into account the intrinsic (local/global geometric) constraints of the $2D$ system which play an important role in determining the phase transition aspects for such systems. After the pioneering work of Collins and Kawamura, very few studies have focussed on developing or testing the theoretical ideas of the proposed geo-

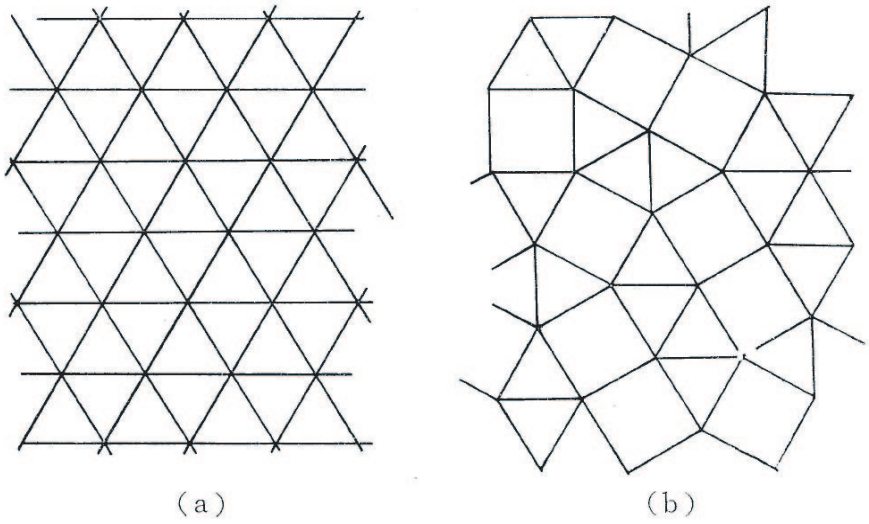

Figure 4.1: Depiction of a simplified Bernal lattice(Collin's model). (a) corresponds to a solid state and (b) corresponds to a fluid state. (Ref: Kawamura (1979))

metrical models. Recently, molecular-dynamics simulation study by Glaser & Clark (1990) demonstrated that packing constraints in $2D$ dense liquids give rise to geometrical structure resembling square-triangular tilings. Jenkins & Satake (1983) have suggested the relevance of these geometrical models for explaining phase transition in analogous macroscopic granular system. However, no generally accepted understanding has emerged yet. We thus focus on studying the applicability of these geometrical models for studying phase transition ideas in granular systems.

4.3 Square-triangular tiling model

In this section, we briefly review some of the main aspects of the square-triangular tiling model proposed by Collins (1964) and Kawamura (1979) and discuss its possible adaptation for understanding macroscopic granular systems.

In the ST tiling lattice model, each lattice point has four possible local configurations as shown in Fig. 4.2. A particular lattice site is categorized as 6-atom if it is surrounded by six triangles and has six nearest neighbors. If a lattice site

is surrounded by three triangles and two squares, it is classified as 5α or 5β atom depending upon the arrangement of squares and triangles. This arrangement of 5α or 5β structure involves five nearest neighbors. The fourth possible configuration involves a lattice site surrounded by four squares and has four nearest neighbors.

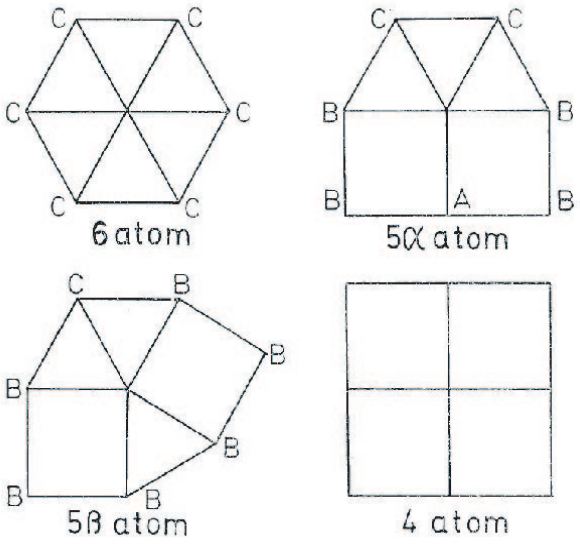

Figure 4.2: Local atomic configurations in the ST tiling lattice model. (Ref: Kawamura (1979)

Consider a system of N disks of which N_r are r disks (r = 4, 5α, 5β, 6). Then we can write,

$$N = N_4 + N_{5\alpha} + N_{5\beta} + N_6. \tag{4.1}$$

If a_r is an area of the voronoi cell associated with an r disk, the total area of the system A is given by

$$N_4 a_4 + N_{5\alpha} a_{5\alpha} + N_{5\beta} a_{5\beta} + N_6 a_6 = A \tag{4.2}$$

where, $a_4 = b^2$, $a_5 = a_{5\alpha} = a_{5\beta} = b^2(2+\sqrt{3})/4$ and $a_6 = b^2\sqrt{3}/2$. Here b is the average bond length (lattice spacing).

For simplicity, we neglect N_4 and set it to zero assuming that this co-ordination is comparatively rare in the solid and fluid phases at high density. In terms of the

fraction $n_r = N_r/N$ of r-disks, equations 4.1 and 4.2 may be written as,

$$n_{5\alpha} + n_{5\beta} + n_6 = 1, \tag{4.3}$$

and

$$(n_{5\alpha} + n_{5\beta})a_5 + n_6 a_6 = A/N. \tag{4.4}$$

Equations 4.3 and 4.4 are constraints on the relative fractions of the types of disks.

For hard core systems, the Helmholtz free energy has only the entropy term. According to Kawamura (1979) the entropy can be divided into two parts: 1) Configurational entropy and 2) vibrational entropy,

$$S = S_{config} + S_{vib}. \tag{4.5}$$

In order to obtain an expression for the configurational entropy it is necessary to determine the number of possible ways to arrange the N_6, $N_{5\alpha}$, and $N_{5\beta}$ disks in the plane. If there were no geometrical constraints this number would be $N!/N_6!N_{5\alpha}!N_{5\beta}!$; this is the number of ways to choose N of the distinguishable r-disks completely at random. However these r-disks must be arranged in such a way that their local configurations fit together to cover the plane. Kawamura provided a possible solution to this problem that takes into account the intrinsic constraints on the configurations.

From inspecting the local atomic configurations in Fig. 4.2 it is clear that an A-site must be the center of a 5α-disk while B-site may be center of either a 5α or a 5β-disk. A C-site imposes no restriction on neighboring configurations. Consequently, for each 5α-disk there must be one 5α disk and four 5α or 5β-disks and for each 5β-disk there must be six 5α or 5β-disks. The number W of possible ways to choose the r-disks in order to satisfy these constraints is given by

$$W \equiv \frac{N!}{N_6!N_{5\alpha}!N_{5\beta}!}(n_{5\alpha} + n_{5\beta})^{(4N_{5\alpha}+6N_{5\beta})/2}(n_{5\alpha})^{(N_{5\alpha})/2}. \tag{4.6}$$

The configurational entropy (S_{config}) is then given by

$$S_{config} = lnW \tag{4.7}$$

After introducing the variables x and t so that

$$n_{5\alpha} + n_{5\beta} = x, n_6 = 1 - x, \tag{4.8}$$

$$n_{5\alpha} = tx, n_{5\beta} = (1-t)x, \tag{4.9}$$

with $0 \leq x \leq 1$ and $0 \leq t \leq 1$, the configurational entropy may be written as,

$$S_{config}/N = -(1-x)ln(1-x) - \frac{tx}{2}ln(tx) - (1-t)xln[(1-t)x] + (3-t)xlnx. \tag{4.10}$$

Next, the vibrational entropy S_{vib} introduced is the one associated with the thermal fluctuations of the centers of the disks about their mean position. This calculation assumes that an r-disk can wander freely in the area available to it in its local configuration when the centers of its neighbors are fixed at their mean positions. We define $\alpha = (b/\sigma) - 1$ where, b = bond length and σ= hard core diameter. When α is small, the free areas v_r of the r-disks are

$$v_5 \equiv v_{5\alpha} = v_{5\beta} = (2 + \sqrt{3})\alpha^2\sigma^2, \tag{4.11}$$

$$v_6 = 2\sqrt{3}\alpha^2\sigma^2. \tag{4.12}$$

The mean free area $\bar{v}$ is then given by,

$$\bar{v} = (1-x)v_6 + xv_5 = v_6(1 + Cx), \tag{4.13}$$

where $C = (2\sqrt{3} - 3)/6$. Then

$$S_{vib}/N \equiv ln\bar{v} \tag{4.14}$$

$$S_{vib}/N = ln(2\sqrt{3}\alpha^2\sigma^2) + ln(1 + Cx). \tag{4.15}$$

Using equations 4.5, 4.7 and 4.15, the expression for total entropy is

$$S = -(1-x)ln(1-x) - \frac{tx}{2}ln(tx) - (1-t)xln[(1-t)x] + (3-t)xlnx + ln(2\sqrt{3}\alpha^2\sigma^2) + ln(1 + Cx). \tag{4.16}$$

The relevant thermodynamic potential for an isochoric hard core system is the Helmholtz free energy which has only the entropy contribution term.

$$F = -TS \tag{4.17}$$

$$F/T = -S \tag{4.18}$$

The temperature T is the mean kinetic energy associated with the fluctuations in position of the centers of the disks. This is the same interpretation of the temperature as in the theories for granular materials. For hard disk system the only internal energy is the total kinetic energy. Because it is proportional to T and independent of x and t, it does not influence the phase transition and hence can be ignored.

From equations 4.16 and 4.18, we can obtain F in terms of three independent variables x, t and α,

$$F/T = (1-x)ln(1-x) + \frac{tx}{2}ln(tx) + (1-t)xln[(1-t)x] - (3-t)xlnx \\ -ln(2\sqrt{3}\alpha^2) - ln(1+Cx). \tag{4.19}$$

If the first partial of F with respect to t is calculated and set to zero, t may be expressed as a function of x,

$$t(x) = \frac{1}{2}(2 + \frac{x}{e} - \sqrt{(2 + (\frac{x}{e})^2} - 4). \tag{4.20}$$

Next, we would like to express α in terms of x to obtain an expression for F as a function of x which can then be minimized. Using equations 4.4 and 4.9 we obtain,

$$xa_5 + (1-x)a_6 = A/N. \tag{4.21}$$

After substituting the expression for a_5 and a_6 in 4.21 we get

$$x\frac{2+\sqrt{3}}{4}b^2 + (1-x)\frac{\sqrt{3}}{2}b^2 = A/N. \tag{4.22}$$

For a constant volume system (isochoric), A will be fixed and the filling fraction ϕ is given by,

$$\phi = \frac{\pi/4\sigma^2 N}{A}. \tag{4.23}$$

Thus we can write,

$$\frac{A}{N} = \frac{\pi/4\sigma^2}{\phi}. \tag{4.24}$$

Substituting 4.24 in 4.22, and solving for b we obtain,

$$b = \frac{\sigma}{2}\sqrt{\frac{\pi}{\phi}}\frac{1}{\sqrt{\frac{\sqrt{3}}{2} + \frac{x}{4}(2-\sqrt{3})}}. \tag{4.25}$$

Since, $\alpha = (b/\sigma) - 1$, we get,

$$\alpha = \frac{1}{2}\sqrt{\frac{\pi}{\phi}}\frac{1}{\sqrt{\frac{\sqrt{3}}{2} + \frac{x}{4}(2-\sqrt{3})}} - 1. \tag{4.26}$$

For constant density (ϕ), Eq. 4.26 is basically an expression for α in terms of x. Using 4.19, 4.20 and 4.26 we get an expression for F in terms of x only,

$$\begin{aligned} f(x) = (1-x)ln(1-x) + \frac{t(x)x}{2}ln(t(x)x) + (1-t(x))xln[(1-t(x))x] \\ -(3-t(x))xlnx - 2ln(\alpha(x)/\alpha(0)) - ln(1+Cx), \end{aligned} \tag{4.27}$$

where, $f(x) = F(x)/T$. Thus Eq. 4.27 can now be minimized to yield $x = x_{min}$, corresponding to the minima in f. The filling fraction (ϕ) dependence of f is implicitly taken into account by the expression for α (Eq. 4.26). For each ϕ we can determine $f(x)$ curve and the corresponding value for x_{min}. Further, it would be interesting to compare the predictions of the geometrical model with the experimental results to determine the applicability of the model.

4.4 Structural signature of square-triangular tilings in granular fluid

For experimental validation of the square-triangular tiling models, we first need to verify the presence of these structures in the granular system. We thus analyze the uniformly heated isochoric granular system using variety of standard measures.

4.4.1 Bond order distribution

We first look at the bond-orientational order parameter ψ_6 introduced by Nelson and Halperin to characterize the structural order in a two-dimensional system (Nelson & Halperin 1979). The local value of ψ_6 for a particle i is given by (Jaster 1999)

$$\psi_6^{local} \equiv \psi_{6,i} = 1/N_i \sum_{j=1}^{N_i} e^{i6\theta_{ij}} \tag{4.28}$$

where θ_{ij} is the angle between the particles i and j and an arbitrary but fixed reference axis and N_i is the number of nearest neighbors of particle i. We obtain the neighbors by using the Voronoi construction (Fraser et al. 1990). We can thus monitor the fluid-to-solid transition on the basis of detecting local structures in the fluid using ψ_6 (Reis et al. 2006). As discussed in detail in Chapter 3 (Section 3.6), our system exhibits three phases: an isotropic fluid phase $\phi < \phi_l = 0.652$, a crystalline solid phase $\phi > \phi_s = 0.719$, and an intermediate phase $\phi_l < \phi < \phi_s$ consistent with a hexatic phase (Reis et al. 2006, Jaster 2004).

Fig. 4.3 shows the distribution of local bond order parameter magnitude $|\psi_6|$ for a range of filling fractions, ϕ. At low filling fractions, $\phi = 0.57$ we get a very broad maximum. For low filling fractions the particles are distributed randomly and no specific ordered structures are formed, and thus a broad maximum is found. As the filling fraction is increased, the distribution becomes increasingly localized around the maximum which spontaneously moves to a higher value of $|\psi_6|$. The distribution shows occurrence of a shoulder around $\phi = 0.62$. This shoulder further

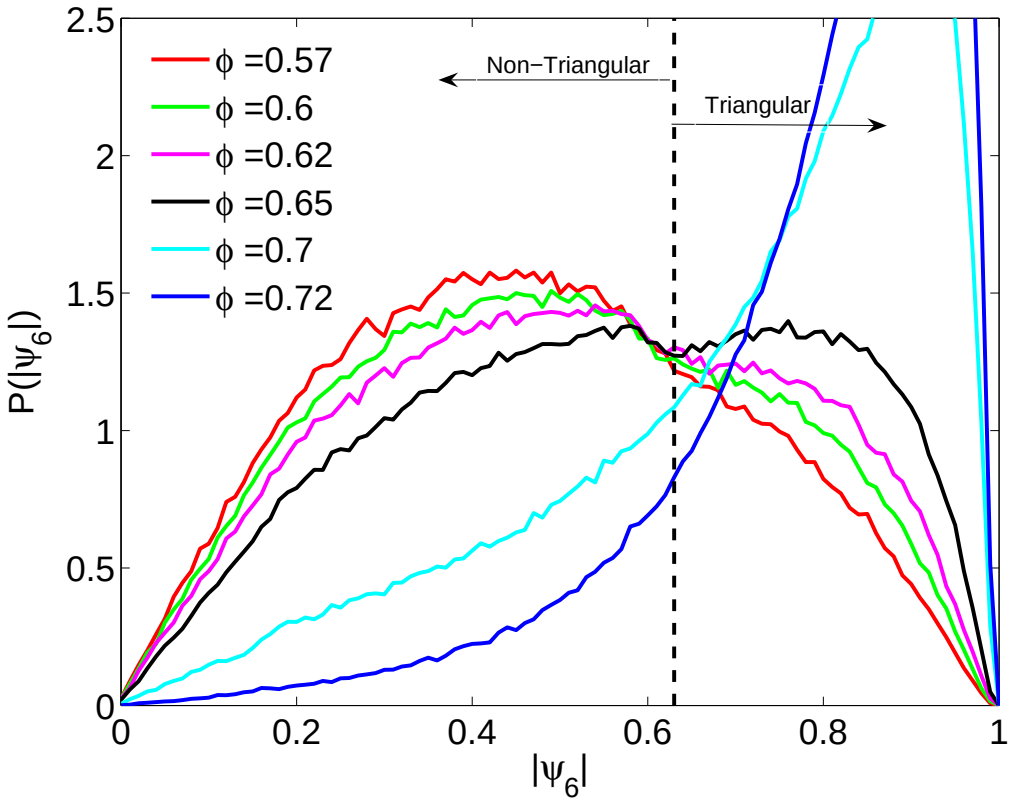

Figure 4.3: Probability distribution of the local order parameter magnitude $|\psi_6|$ for specific values of filling fraction ϕ. Triangular order is assumed for $|\psi_6| \geq 0.63$ as shown by the dotted line in the figure.

develops with increasing filling fraction and evolves to a distinct second maximum ($\phi \approx 0.65$). For filling fractions near $\phi \approx 0.7$, i.e., in the vicinity of the melting filling fraction, ($\phi = 0.716$) (Mitus et al. 1997) and higher, the original maximum for low $|\psi_6|$ values disappears, on the other hand, the high $|\psi_6|$ maximum sharply rises, which is centered close to $|\psi_6| \approx 1.0$. For perfectly hexagonal packing, we would expect a delta function located at $|\psi_6| = 1$, which is value for regular hexagonal arrangement of particles.

We identify regions with local solid like orientational order (triangular ordered clusters, or TOC's) in the fluid phase on the basis of the value of local bond order parameter. The location of the minimum in the distribution of the local bond order

parameter is at $|\psi_6| = 0.63$ which is roughly independent of the filling fraction, ϕ. Particles with value of local bond order parameter, $|\psi_6| \geq 0.63$ are assigned to triangular ordered clusters (TOCs) while those with $|\psi_6| < 0.63$ are assigned to non-triangular ordered clusters (nTOCs). Now, having partitioned the fluid into triangular ordered clusters and disordered regions we can probe the structural properties independently.

4.4.2 Bond length and Bond angle distribution

Next, we look at the bond length and bond angle distribution for our uniformly heated granular system.

Fig. 4.4a shows distribution of nearest neighbor bond lengths (r), while Fig. 4.4b shows the distribution $P(\Phi)$ of nearest neighbor bond angles given by $\Phi \equiv \Phi_{i,j} = \theta_{i,j+1} - \theta_{i,j}$, both at $\phi = 0.654$. In each case we show the distribution for particles in TOC's, for particles not in TOC's (i.e. nTOC's) and the combined sum for all the particles. For particles in TOC's, the distributions have single peaks located approximately at $r = 1$ and $\Phi = 58$. For particle not in TOC's, the distribution is multipeaked, with peaks at $r = 1$ and 1.4 and $\Phi = 45$, 58, and 90. The extra peaks strongly suggest the presence of square lattice in the topology of the granular fluid having the same lattice parameter as TOC's: $\Phi = 45$ and 90, and $r = \sqrt{2} = 1.414$.

4.4.3 Dilution of Voronoi network

Simulation studies (Glaser & Clark 1990) of dense two dimensional hard disk fluids indicate the presence of regions with local "square" particle arrangement along with the regular hexagonal lattice. We use the Glaser and Clark (Glaser & Clark 1990) methodology for characterizing the structure of the $2D$ hard disk fluid that incorporates more information about the geometry than the Voronoi construction. The network of bonds formed by connecting each particle to the set of nearest neighbors

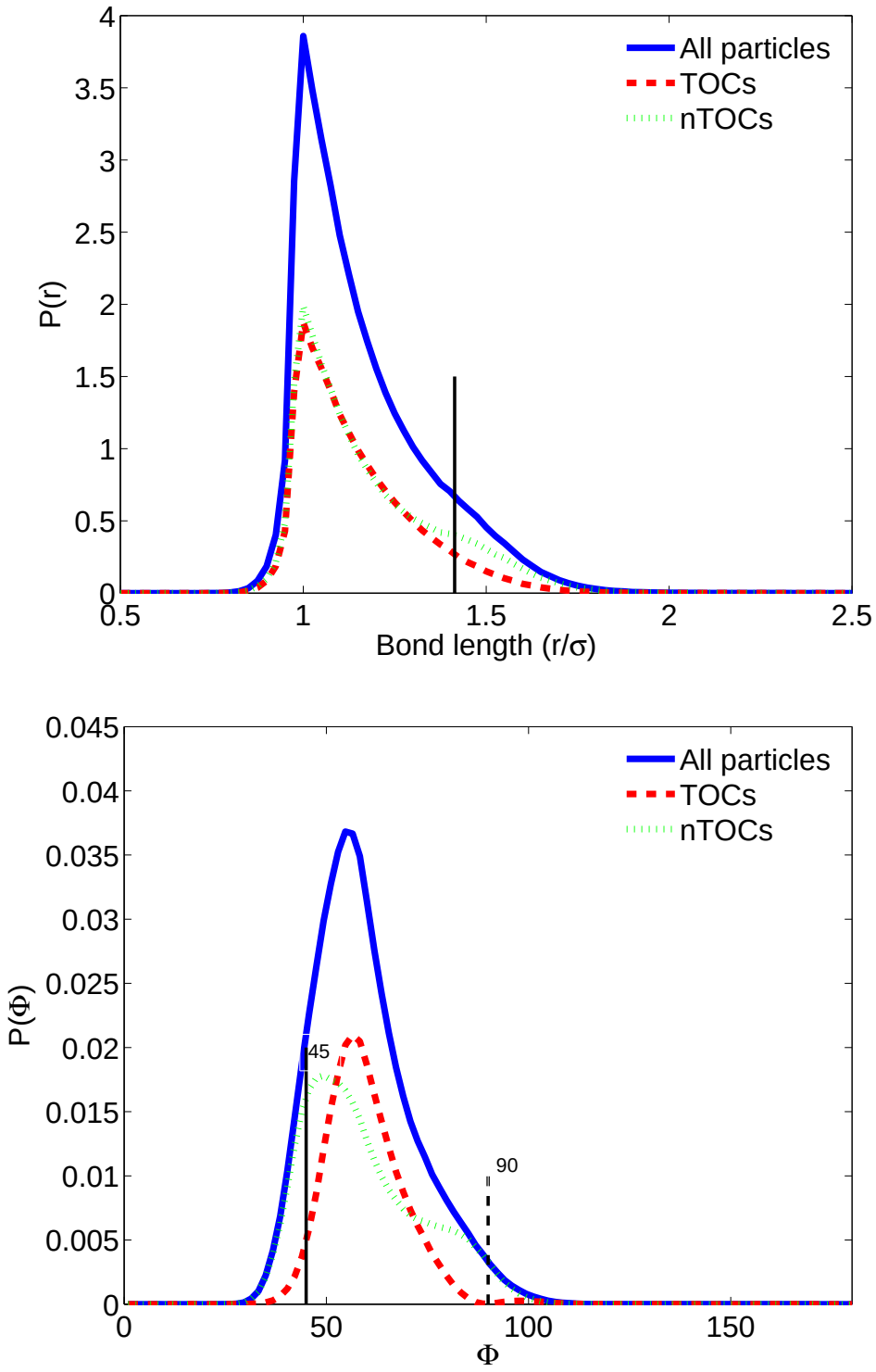

Figure 4.4: Probability distributions of (a) nearest neighbor bond lengths r and (b) nearest neighbor bond angles Φ, for particles in TOC's (–), particles not in TOC's $(\cdots)$, and all particles (-). The filling fraction was kept constant at $\phi = 0.654$. The vertical solid line in (a) corresponds to bond length, $r = \sqrt{2}$ and in (b) corresponds to bond angle, $\Phi = 45$. The vertical dashed line in (b) corresponds to bond angle, $\Phi = 90$.

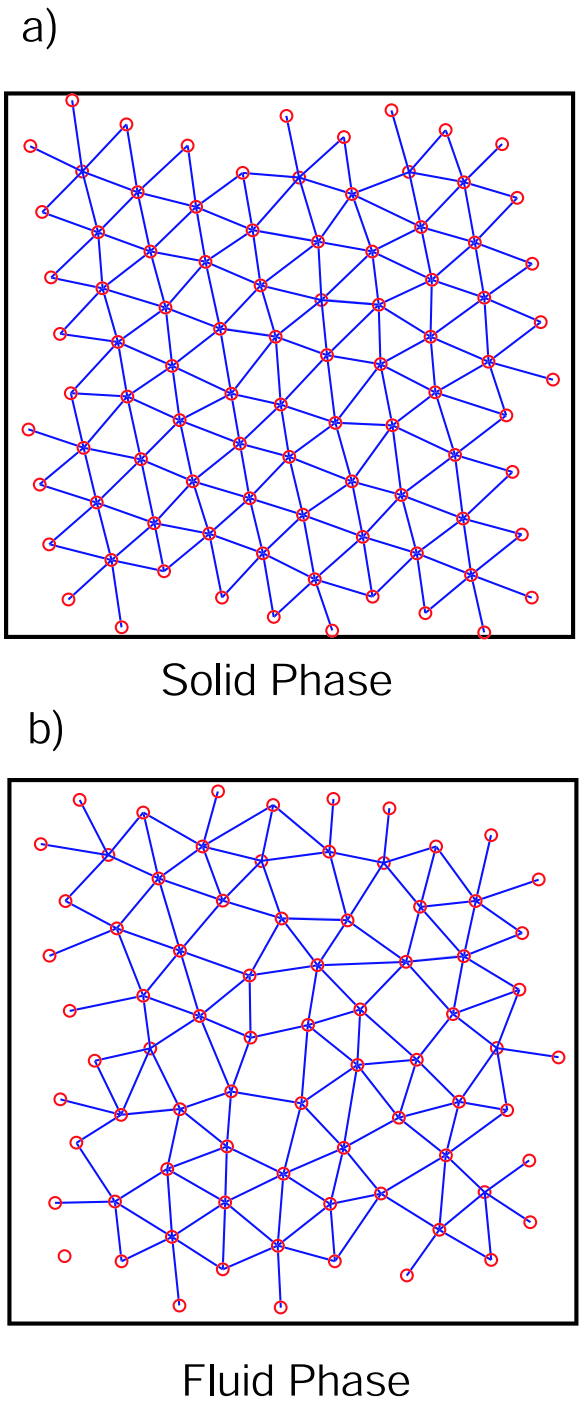

Figure 4.5: Examples of experimentally determined Square-triangular (ST) tiling lattice structure at two different filling fractions, (a) $\phi = 0.75$ (solidlike phase) and (b) $\phi = 0.654$ (fluidlike phase).

found from the Voronoi construction divides the plane into triangular regions. We systematically dilute this network by removing bonds associated with the secondary peaks in the $P(r)$ or $P(\Phi)$ distributions, arriving at a geometrical-neighbor network, which partitions the topological plane into areas having three or more sides.

Figure 4.5(a-b) shows the resulting topological structures obtained after systematic dilution of bonds at two different filling fractions. At high filling fraction, $\phi = 0.75$ we observe that the lattice is composed of only close packed triangles with a regular hexagonal arrangement of particles [see Figure 4.5a]. However at low filling fractions ($\phi = 0.654$) we observe patches of closed packed squares and triangles. The local structure observed in Figure 4.5b resembles plane tilings composed of squares and equilateral triangles of equal edge length (ST tilings).

4.5 Local particle configuration

Since our experimental results point out the presence of square-triangular tiling structure in the quasi-2D granular fluid, we would like to take the analysis one step further. We would now like to identify and quantify the presence of local particle configuration as 6-atom, 5α, 5β or 4-atom. We can look at the systematic variation of each class of particle type as a function of the filling fraction. This will provide a clear physical picture of the underlying topology and also allow for comparison with theoretical predictions of the ST tiling models.

For identifying the local particle configuration we use the following strategy. First, we update the nearest neighbor list of each particle after removing the bonds associated with the secondary peaks in the $P(r)$ or $P(\Phi)$ distributions. This results in a topological landscape where every particle has either 6, 5 or 4 neighbors. Particle with five neighbors are then analyzed for classification as 5α or 5β type. For ideal 5α structure the maximum value of the sum of adjacent bond angles is 180, while that for ideal 5β structure is 150 (see Fig. 4.2). Thus we can specify a cut-off value

between 150 and 180 for the maximum value of the sum of adjacent bond angles and distinguish between 5α and 5β structures. For example, we can choose the cut-off to be 165 (mean of 150 and 180) and then classify 5 neighbor particles with the maximum value of the sum of adjacent bond angles greater than 165 as 5α type and those lower than 165 as 5β type structure. This would be appropriate for an idealized 5-atom structure where the (maximum sum of adjacent) angles would be exactly 150 or 180, which is not the case for our experimental non-ideal ST tiling lattice. Thus in our classification scheme, we determine the optimum cut-off by analyzing the distribution of sum of adjacent bond angles for 5 atom structures at every particular filling fraction. This distribution will have peaks located at ≈ 120, 150 and 180. We then pick the minima value of the distribution (between 150 and 180) as a cut-off value for the classification between 5α and 5β type structures for that particular filling fraction.

Using the above mentioned classification scheme, we plot in Fig. 4.6, the systematic variation of each lattice configuration as a function of filling fraction. At low filling fraction the lattice configuration is primarily composed of 5α, 5β and 6-atom lattice sites. As we increase ϕ, the fraction of 6-atom sites increases substantially accompanied by equally sharp decrease in 5α and 5β sites. The 4-atom lattice sites are in negligible proportion through out the range of ϕs investigated. Above $\phi = 0.719$, the lattice configuration is almost entirely composed of 6-atom sites, while all other lattice sites have a very minor presence in the lattice.

4.6 Comparison with Theory

We now compare the experimental findings with the theoretical predictions of the ST tiling model. As illustrated in Section 4.3, we can predict the fraction of each particle type based on the geometrical model. In particular we refer to equations 4.9 and 4.20, which allow us to predict the fraction of 5α and 5β sites based on the

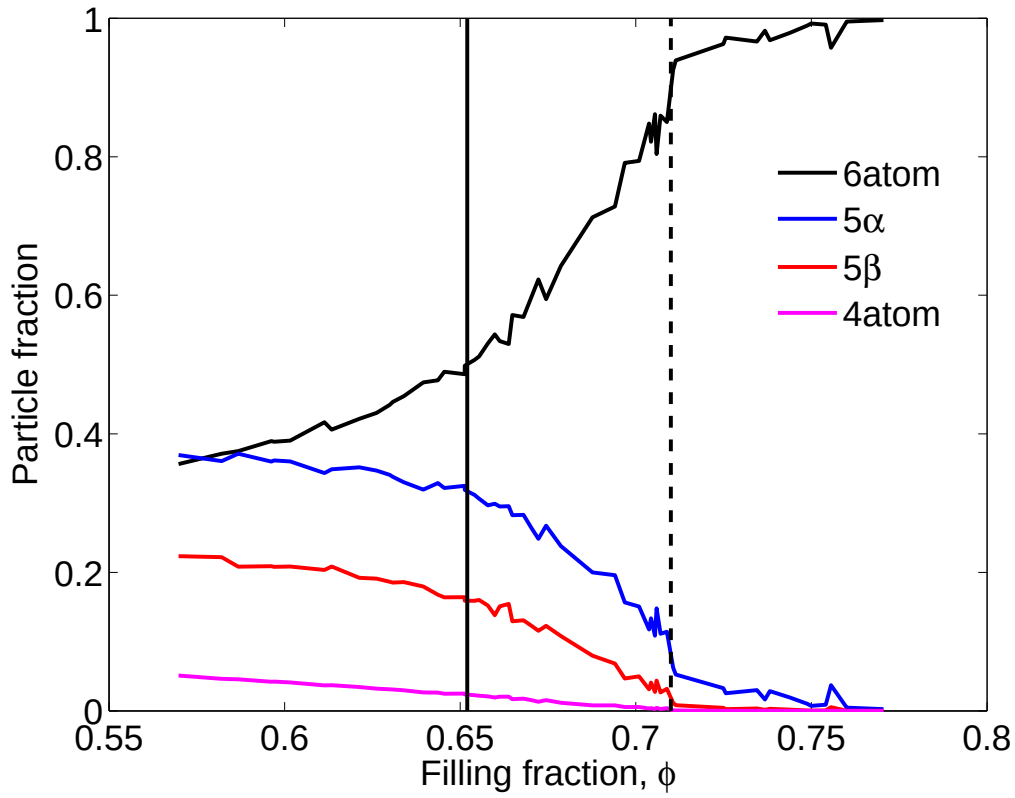

Figure 4.6: Fraction of each particle type as a function of filling fraction. The solid and dashed vertical lines are located at $\phi_l = 0.652$ (fluidus point) and $\phi_s = 0.719$ (solidus point), respectively.

specified value for x. We input the experimentally determined value for x for each filling fraction in equations 4.9 and 4.20, and then arrive at the predicted value for 5α and 5β fraction.

Fig. 4.7 shows the comparison between the experimental results and the theoretical predictions of the ST tiling model for the fraction of 5α and 5β sites. We find an excellent agreement between the experiment and the theory over a wide range of filling fractions. We also observe that the fraction of 5α sites is always dominant and higher than the 5β fraction over the investigated range of filling fractions. This is due to the fact that the 5β site imposes higher constraints on the lattice geometry as compared to the 5α sites (Fig. 4.2) as per the ST tiling model. Our experimental

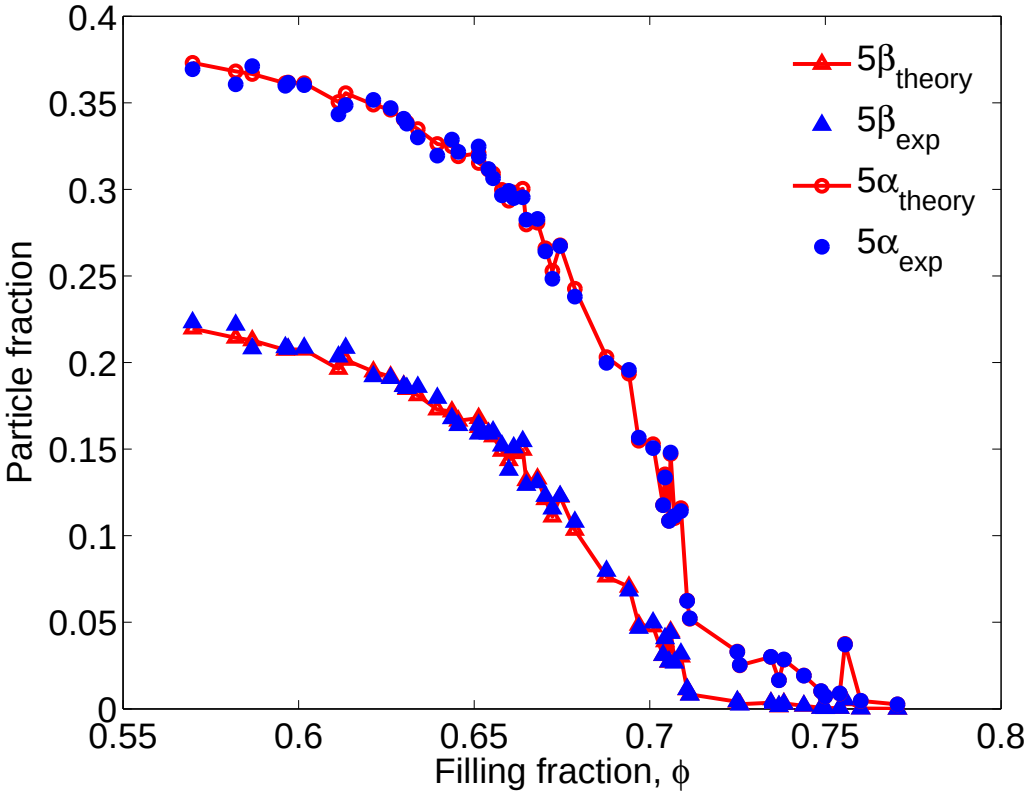

Figure 4.7: Fraction of 5α and 5β sites for a range of filling fractions, ϕ for both cases of experiments and theory.

results are consistent with this observation.

Next, we study the comparison between the experimentally determined bond lengths and the predicted bond lengths from the geometrical model. Using Eq. 4.26, we predict the bond length at a particular values of filling fraction (ϕ) and combined fraction of 5α and 5β sites, x. We plot these values against the experimentally determined average bond length corresponding to each x as shown in Fig. 4.8. We again find a good agreement between the experimental values and the theoretical prediction.

Finally, in Fig. 4.9 we plot the expression for the free energy ($f(x)$) as given by Eq. 4.27 for various filling fractions. The expression is normalized to zero at $x = 0$

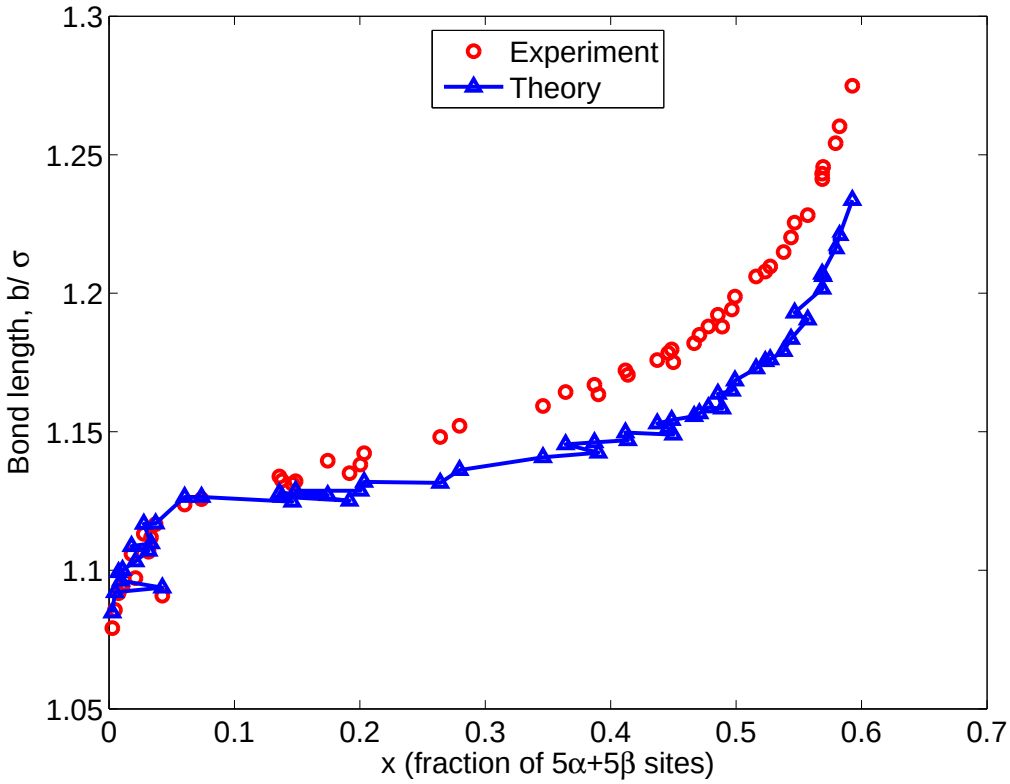

Figure 4.8: Dependence of average bond length (b) on the combined fraction of 5α and 5β sites, x.

for any given value of filling fraction, ϕ. At $x = 0$, the lattice is usual hexagonal lattice and corresponds to a solid state. $f(x)$ has one minima at $x = 0$ and the other at $x = x^* \neq 0$. At $x = x^*$, the lattice contains squares as well as triangles and this corresponds to a fluid state. By comparing these two minima we get three different situations. When $\phi < 0.69$, the fluid state has a lower free energy. When $\phi > 0.69$, the solid state has a lower free energy. When $\phi = 0.69$, the solid and fluid state have equal free energy and the solid-fluid transition is predicted to occur. Thus the free energy expression predicts a first-order like transition for the $2D$ hard disk system. Early computer simulations of hard disks (Alder & Wainwright 1962) have always shown evidence of strong first-order transition. However in our experiments the

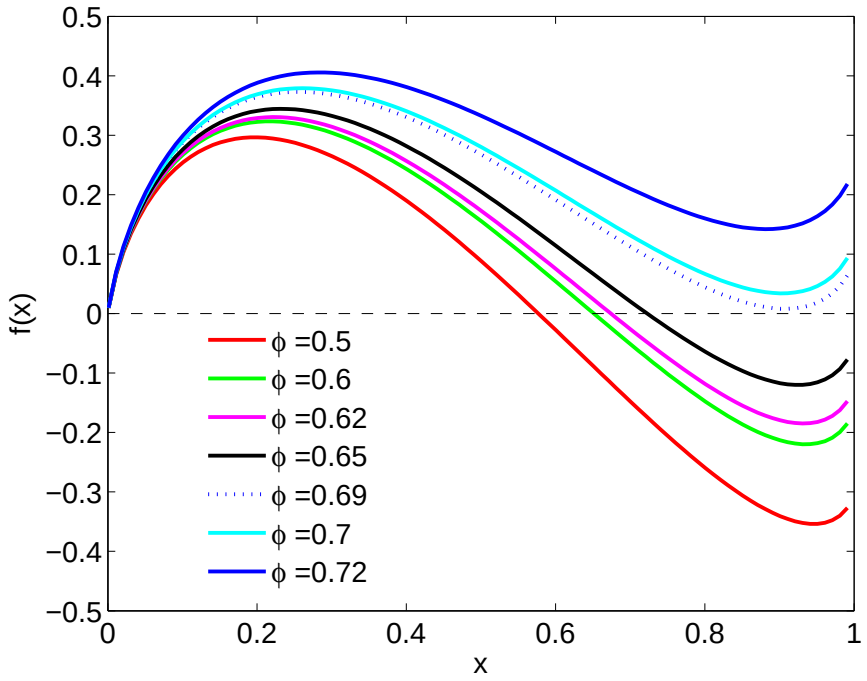

Figure 4.9: Normalized free energy f(x) vs x for various values of filling fraction, ϕ.

fraction of each particle type and the combined fraction x vary smoothly with the filling fraction (see Fig. 4.6) with no observed discontinuity, suggesting a continuous transition. Olafsen & Urbach (2005) have shown that a horizontal monolayer of spheres confined between two vibrating plates exhibits a continuous transition from a hexagonally ordered solid phase to a disordered liquid that is well described by the KTHNY theory. This finding is consistent with recent computer simulations on the melting transition of hard disk systems in two dimensions (Jaster 1999, Sengupta, Nielaba & Binder 2000, Watanabe, Yukawa, Ozeki & Ito 2004). Thus the current geometrical model framework for $2D$ melting of hard disks needs to be suitably modified or adapted to explain the observed continuous phase transition.

4.7 Discussion

In summary, we have presented a novel geometrical mechanism for solid-fluid phase transition in a quasi-2D granular fluid. The packing constraints in our quasi-2D granular fluid give rise to a geometrical structure resembling plane tilings composed of closed packed squares and triangles (ST Tilings). The square-triangular tiling construction contains geometrical information (information about the bond lengths and bond angles) as well as topological information (information about the connectivity of the nearest-neighbor bond network) and so gives a more detailed picture of the underlying structure than the Voronoi construction (which contains primarily topological information). Our experimental results are also consistent with $2D$ melting models based on ST tilings (Collins 1964, Kawamura 1979). We have succeeded in making an experimental observations of the square-triangular tilings in macroscopic quasi-2D granular fluids. Our experimental observation strongly suggest that $2D$ melting may occur through the proliferation of geometrical defects i.e regions of local "square" particle arrangement. Further, we find excellent agreement between some of the theoretical predictions of the ST tiling model and our experimental results. The ST tiling model can possibly explain the observed phase transition in granular systems from fluid to solid state based on entropiclike arguments. This would be an important step towards advancing our understanding of non-equilibrium phase transition phenomena which requires further investigation. Nevertheless, our current results present a direct evidence and methodology for developing a entropylike formalism to explain nonequilibrium phase transitions.

Chapter 5

Velocity distributions in uniformly heated granular fluid

In this chapter we present experimental results on the velocity statistics of a granular fluid in a uniformly heated quasi-two-dimensional configuration (Reis, Ingale & Shattuck 2007*b*). We measure the steady state velocity distribution as a function of various experimental parameters. The velocity distributions show marked deviation from the equilibrium behavior (Maxwell-Boltzmann distribution). We quantify these deviations from equilibrium and find that the kinetic theory framework is appropriate and extremely useful in characterizing the behavior in our system.

5.1 Introduction

As discussed in detail in Chapter 1, granular systems are out of equilibrium systems and intrinsically dissipative in nature. Therefore such systems are not expected to behave similarly to the equilibrium counter-parts of classical fluids (Kadanoff 1999). However, we have shown in Chapter 3, that the structure of a uniformly heated quasi-2D granular fluid is identical to that found in simulations of equilibrium hard disks (Reis et al. 2006). Further, we have shown in a recent investigation that the mean-squared displacement of grains shows diffusive behavior at low density and caging behavior as the density is increased until particles are completely confined

above the freezing point, just as in ordinary molecular fluids (Reis, Ingale & Shattuck 2007*a*). These surprising results provide a partial experimental justification for the theoretical treatment of granular flow by analogy with molecular fluids using standard statistical mechanics and kinetic theory. A large number of kinetic theories of granular flows (Savage & Jeffery 1981, Lun et al. 1983, Jenkins & Richman 1985, Jenkins & Richman 1988, Lun 1991, Goldshtein & Shapiro 1995, Sela, Goldhirsch & Noskowicz 1996, Brey, Moreno & Dufty 1996, Santos, Montanero, Dufty & Brey 1998, van Noije, Ernst & Brito 1998, Garzó & Dufty 1999, Dufty & Brey 2003, Brey & Ruiz-Montero 2004, Dufty, Baskaran & Zogaib 2004, Kumaran 2005, Brey & Dufty 2005, Lutsko 2006) have been produced starting in 1980's. The results of these theories are balance equation analogous to the Navier-Stokes equations for the density, n, the average velocity, $\mathbf{v}_o$, and the average kinetic energy per particle or temperature, T, as well as, equations of state and transport coefficients, which are functions of n, $\mathbf{v}_0$, and T. The heart of these formulations is the single particle distribution function $f^{(1)}(\mathbf{r}, \mathbf{v}, t)$, which measures the probability of a particle at position $\mathbf{r}$ having velocity $\mathbf{v}$. The field equations are derived from moments of $f^{(1)}(\mathbf{r}, \mathbf{v}, t)$. For example, the density, n, is the 0th moment, the average velocity, $\mathbf{v}_o$, is the 1st moment, and the temperature, T, is the 2nd moment. The transport coefficients are determined from non-equilibrium perturbations of $f^{(1)}(\mathbf{r}, \mathbf{v}, t)$. Generally the equilibrium or steady-state distribution is assumed to be independent of space and to have Maxwell-Boltzmann form $f^{(1)} = f_{MB} = A \exp\left(-\frac{|\mathbf{v}-\mathbf{v}_0|^2}{2T}\right)$, although, recent work has explored the use of other base states or steady-state distributions (Dufty et al. 2004, Brey & Dufty 2005, Lutsko 2006).

Two important questions one may ask are: 1) What is the base state $f^{(1)}$ for a driven granular fluid? and 2) Does it have a universal form? If it was to be characterized by a small number of parameters such as the moments of the $f^{(1)}$ distribution as in the case for ideal fluids, one would be able to advance a great deal

in developing predictive continuum models for granular flows since the theoretical machinery from kinetic theory could be readily applied. The careful experimental study and characterization of this base state is therefore important in order to develop a theory for granular media, similar to that of regular molecular liquids.

5.2 Previous Investigations

There has been a substantial amount of experimental, numerical, and theoretical work to address these issues in configurations where the energy input perfectly balances the dissipation such that the system reaches a steady state, albeit far from equilibrium. These *non-equilibrium steady states* are simplified realizations of granular flows more amenable to analysis, but the insight gained from their study should be helpful in the tackling of other more complex scenarios. One feature that has been consistently established in experiments is that single particle velocity distribution functions deviate from the Maxwell-Boltzmann distribution (Losert et al. 1999, Olafsen & Urbach 1999, Rouyer & Menon 2000, Blair & Kudrolli 2001, Prevost, Egolf & Urbach 2002, Aranson & Olafsen 2002, Blair & Kudrolli 2003). In particular, the tails (i.e. large velocities) of the experimental distributions exhibit a considerable overpopulation and have been shown to scale as $f^{(1)}(v_i) \sim \exp[(v_i/\sqrt{T_i})^{3/2}]$ where v_i is a velocity component and $T_i = \langle v_i^2 \rangle$ is the *granular temperature*. This behavior is in good agreement with both numerical (Moon, Shattuck & Swift 2001) and theoretical (van Noije & Ernst 1998) predictions. Even though these tails correspond to events with extremely low probabilities, they increase the variance of the distribution. The variance of the distribution is T, the average kinetic energy of the particles. Using a Gaussian to represent this type of distribution leads to major discrepancy in the region of high probability at the central part of the distribution (low velocities) (Blair & Kudrolli 2003) which have, thus far, been greatly overlooked in experimental work. Note that requiring the variance of $f^{(1)}(v_i)$ to be the granular

temperature greatly constrains the functional form that the distribution can take.

A model system that has been introduced to study this question is the case of a homogeneous granular gas heated by a stochastic thermostat, i.e. an ensemble of inelastic particles randomly driven by a white noise energy source (Williams & MacKintosh 1996). Recently, there have been many theoretical and numerical studies on this model system (van Noije & Ernst 1998, van Noije, Ernst, Trizac & Pagonabarraga 1999, Montanero & Santos 2000, Moon et al. 2001, Brilliantov & Poschel 2006, Pöschel, Brilliantov & Formella 2006) where the steady state velocity distribution have been found to deviate from the Maxwell-Boltzmann distribution. van Noije & Ernst (1998) studied these velocity distributions based on approximate solutions to the inelastic hard sphere Enskog-Boltzmann equation by an expansion in Sonine polynomials. The results of their theoretical analysis has been validated by numerical studies using both molecular dynamics (Moon et al. 2001) simulations and direct simulation Monte Carlo (Montanero & Santos 2000, Pöschel et al. 2006). The use of Sonine corrections is particular attractive since it leaves the variance of the resulting velocity distribution unchanged but leads to a non-Gaussian fourth moment or kurtosis, $K \neq 3$.

5.3 Our Approach

We have addressed the above issues in a well controlled experiment in which we are able to perform precision measurements of the velocity distributions of a uniformly heated granular fluid. The experimental apparatus is discussed in detail in Chapter 3, Section 3.2. A novel feature of our experimental technique is that we are able to generate macroscopic random walkers over a wide range of filling fractions and thermalize the granular particles in a way analogous to a stochastic thermostat. Even though our experimental thermostat is not perfectly Gaussian, we are able to reproduce many of the features observed in the numerical and theoretical work

mentioned above. It is, therefore an ideal experimental realization in which to test the applicability of some of the kinetic theory ideas. In chapter 3, we focused on the *structural configurations* of this granular fluid and revealed striking similarity to those adopted by a fluid of equilibrium hard disks. Here we concentrate on the *dynamical aspects* of this same experimental system, as measured by the single particle velocity distribution, $P(c)$, and observe a marked departure from the equilibrium behavior, i.e. from the Maxwell-Boltzmann distribution. We quantify these deviations from equilibrium and find that the kinetic theory framework is appropriate and extremely useful in characterizing the behavior in our system.

In particular, we find a consistent overpopulation in the distribution's high energy tails, which scale as stretched exponentials with an exponent 3/2. In addition, we experimentally determine the deviations from a Gaussian of the full distributions following a Sonine expansion method and find them to be well described by a second order Sonine polynomial correction. We establish that the central high probability regions of the velocity distributions are well described by

$$P(c) = f_{MB}\{1 + a_2(1/2c^4 - 3/2^2 + 3/8)\} \tag{5.1}$$

where a_2 is the non-gaussianity parameter that can be related to the kurtosis of the distribution and the forth-order polynomial is the Sonine polynomial of order 2. This functional form of $P(c)$ was found to be valid over a wide range of the system parameters. The parameter a_2 strongly depends on filling fraction and is independent of the frequency and dimensionless acceleration of the driving over a wide range. To our knowledge, this is the first time that the Sonine corrections of the velocity distributions have been measured in an experimental system. Even though the way we inject energy into the granular fluid is specific we expect that many of the features we report should also be observed in other driven granular systems.

This chapter is organized as follows. In Sec. 5.4 we briefly review the theoretical framework of kinetic theory along with the steady state solution to the Enskog-Boltzmann equation using the Sonine polynomial expansion method. In Sec. 5.5, we discuss the experimental control parameters. In Sec. 5.6, using the concept of granular temperature, we then quantify the dynamics of the experimentally obtained non-equilibrium steady states, for a number of parameters, namely: the filling fraction, the driving parameters (frequency and acceleration) and the vertical gap of the cell. In Sec. 5.7 we turn to a detailed investigation of the Probability Distribution Functions of velocities as a function of the system parameters. In particular, we quantify the deviations from Maxwell-Boltzmann behavior at large velocities (tails of the distributions) – Sec. 5.7.1. In Sec. 5.7.2 we extend the deviation analysis to the full range of the distribution using an expansion method that highlights deviations at low velocities and allows us to make a connection with Sonine polynomials. We finish in Sec. 5.8 with some concluding remarks.

5.4 Brief Review of Theory

We briefly review the key features of the kinetic theory for granular media pertinent to our study. The number of particles in a volume element, $d\mathbf{r}$, and velocity element, $d\mathbf{v}$, centered at position $\mathbf{r}$ and velocity $\mathbf{v}$ is given by $f^1(\mathbf{r},\mathbf{v},t)d\mathbf{r}d\mathbf{v}$, where $f^1(\mathbf{r},\mathbf{v},t)$ is the single particle distribution function. Continuum fields are given as averages over $f^1(\mathbf{r},\mathbf{v},t)$. For instance, the number density, n, average velocity, v_o, and granular temperature, T, are given respectively by,

$$n(\mathbf{r},t) \equiv \int f^1(\mathbf{r},\mathbf{v},t)d\mathbf{v}, \tag{5.2}$$

$$\mathbf{v}_o(\mathbf{r},t) \equiv \frac{1}{n}\int f^1(\mathbf{r},\mathbf{v},t)\mathbf{v}d\mathbf{v}, \tag{5.3}$$

$$T(\mathbf{r},t) \equiv \frac{1}{nd}\int f^1(\mathbf{r},\mathbf{v},t)(\mathbf{v}-\mathbf{v}_o)^2 d\mathbf{v}, \tag{5.4}$$

where d is the number of dimensions. It is important to note that the granular temperature T is not the thermodynamic temperature but, by analogy, the kinetic energy per macroscopic particle (explained in detail in Sec. 5.6). For the spatially homogeneous and isotropic case, we refer to the single particle distribution function as $f^1(\mathbf{v}, t)$ and consider only a single component of the velocity, i.e. $f^{(1)}(v_i, t)$. From now on we drop the index i. It is also convenient to introduce a scaled distribution function $f^1(c, t)$ where the velocity is scaled by a characteristic velocity such that, $c = v/\sqrt{2T(t)}$, where $T(t)$ is the granular temperature and equal to the variance of $f^1(c, t)$.

The stochastically heated single particle distribution function $f(c, t)$ satisfies the *Enskog-Boltzmann* equation,

$$\frac{\partial f}{\partial t} = \mathcal{Q}(f, f) + \mathcal{F}_{FP} f, \tag{5.5}$$

where, $\mathcal{Q}$, is the collision operator, which accounts for the inelastic particle interactions and the Fokker-Plank operator, $\mathcal{F}_{FP}$, accounts for the stochastic forcing (van Noije & Ernst 1998, van Noije et al. 1998). We are interested in a stationary solution of Eqn. (5.5) where the heating exactly balances the loss of energy due to collisions and the temperature becomes time independent. van Noije and Ernst (van Noije & Ernst 1998) obtained steady state solutions to Eqn. (5.5) by taking the series expansion of $f(c)$ away from a Maxwell-Boltzmann, f_{MB}, i.e.

$$f(c) = f_{MB}(c) \left\{ 1 + \sum_{p=1}^{\infty} a_p S_p(c^2) \right\}, \tag{5.6}$$

in terms of the Sonine polynomials $S_p(c^2)$ where a_p is a numerical coefficient for the p^{th}-order. The deviations from the MB distribution are thus expressed in terms of an expansion on Sonine polynomials. The Sonine polynomials, which are knows as associated Laguerre polynomials in different contexts, are defined as,

$$S_p(c^2) = \sum_{n=0}^{p} \frac{(-1)^n (p + 1/2)!}{(n + 1/2)!(p - n)! n!} (c^2)^n. \tag{5.7}$$

These are orthogonal accordingly to the relationship,

$$\int_0^\infty c^2 e^{-c^2} S_p(c^2) S_m(c^2) dc = \frac{1}{2}\delta_{pm} \frac{(\frac{1}{2}+n)!}{n!}. \tag{5.8}$$

To further simply the calculation, terms higher than $\mathcal{O}(2)$ are typically neglected, such that,

$$f(c) = f_{MB}(c) \left\{1 + a_2 S_2(c^2)\right\}, \tag{5.9}$$

where,

$$f_{MB}(c) = \frac{1}{\sqrt{\pi}} exp(-c^2), \tag{5.10}$$

is the Maxwell-Boltzmann distribution and

$$S_2(c^2) = \frac{1}{2}c^4 - \frac{3}{2}c^2 + \frac{3}{8} \tag{5.11}$$

is the $\mathcal{O}(2)$ Sonine polynomial for 2D. The first Sonine coefficient, a_1, is zero according to the definition of temperature (Goldshtein & Shapiro 1995). The second Sonine coefficient, a_2 is the first non-trivial Sonine coefficient and hence the first non-vanishing correction to the MB distribution and can be related to the kurtosis $K = 3(a_2 + 1)$ of the distribution.

5.5 Our experiments and control parameters

The experimental apparatus has been described in detail in Chapter 3, Section 3.2. Here we briefly illustrate the experimental control parameters.

The first *control* parameter was the filling fraction of the steel spheres in the cell defined as,

$$\phi = \frac{N\pi(D/2)^2}{\pi R^2}, \tag{5.12}$$

where N is the number of spheres (with diameter $D = 1.19mm$) in the cell of radius $R = 50.8mm$. The filling fraction ϕ is therefore defined in the projection of the cell onto the horizontal plane. The second control parameter was the height, h, of the experimental cell which we varied from $1.3D < h < 2.3D$.

The granular cell was set horizontal in order to minimize compaction effects, inhomogeneities and density gradients which otherwise would be induced by gravity. This way, a wide range of filling fractions, $0 < \phi \leq 0.8$, could be accurately explored by varying the number of spheres in the cell, N, down to a resolution of single particle increments. Moreover, as we shall show in Sec. 5.6, we were able to attain spatially uniform driving of the spheres in the cell due to the use of the rough glass bottom plate.

The *forcing* parameters of the system were the frequency, f, and amplitude, A, of the sinusoidal oscillations. From these, it is common practice to construct a non-dimensional acceleration parameter,

$$\Gamma = \frac{A(2\pi f)^2}{g}, \tag{5.13}$$

where g is the gravitational acceleration. We worked within the experimental ranges $(10 < f < 100)Hz$ and $1 < \Gamma < 6$.

5.6 Driven monolayers: granular temperature

We now focus on the study of granular monolayers. In our study we first systematically vary the filling fraction, ϕ, i.e., the density of the particles. In Fig. 5.1 we present typical configurations, at three values of ϕ, for a granular layer driven at $f = 50Hz$ and $\Gamma = 4$ with a rough bottom plate. The snap-shot in Fig. 5.1(a), for $\phi = 0.34$, corresponds to a dilute state in which the particles perform large excursions in between collisions as they randomly diffuse across the cell. If the filling fraction is increased, as in the example of the frame shown in Fig. 5.1(b) for $\phi = 0.67$, one observes a higher collision rate characteristic of a dense gaseous regime. For even higher values of filling fraction the spheres ordered into an hexagonally packed arrangement and became locked into the *cage* formed by its six neighbors. The system is then said to be *crystallized* as shown in the typical frame presented in Fig.

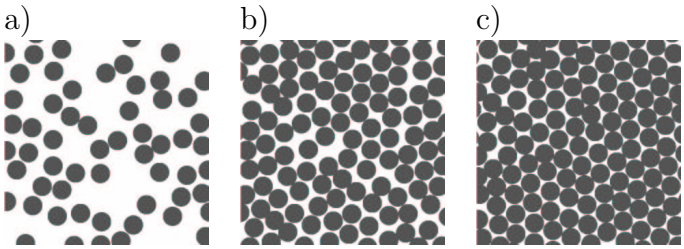

Figure 5.1: Snapshots of typical configurations of the granular layer at various values of the filling fraction: (a) dilute gas, $\phi = 0.34$, (b) dense fluid, $\phi = 0.67$ and (c) thermalized crystal, $\phi = 0.80$. Driving parameters: $f = 50Hz$, $\Gamma = 4.0$.

5.1(c) for $\phi = 0.80$. The structural configurations associated with the crystallization transition, as a function of filling fraction, were studied in detail in Chapter 3, and the *caging* dynamics, as crystallization is approached in (Reis et al. 2007*a*).

The granular temperature (T) is the average kinetic energy per particle given by,

$$T = T_x + T_y = \frac{1}{2}\left(\langle v_x^2\rangle + \langle v_y^2\rangle\right), \tag{5.14}$$

where v_x and v_y are the two orthogonal components of the velocity in the 2D horizontal plane and the brackets $\langle . \rangle$ denote both time and ensemble averages for all the spheres found within the imaging window. Moreover, one can define $T_x = 1/2\langle v_x^2\rangle$ and $T_y = 1/2\langle v_y^2\rangle$, with $T = T_x + T_y$, as the temperature projections onto the x and y directions of the horizontal plane.

In Fig. 5.2 the temperature components, T_x and T_y, are plotted as a function of filling fraction. For both cases of using a rough and a flat bottom plate, the respective T_x and T_y are identical. This shows that the effective forcing of the granular particles provided by the oscillating plates was isotropic in the horizontal plane. In agreement with the case of a single particle, the dynamics of the granular layer using a flat or a rough bottom plate is remarkably different. As discussed previously in Chapter 3, the rough bottom plate effectively randomizes the single particle trajectories. If the rough bottom plate is used, the granular temperature

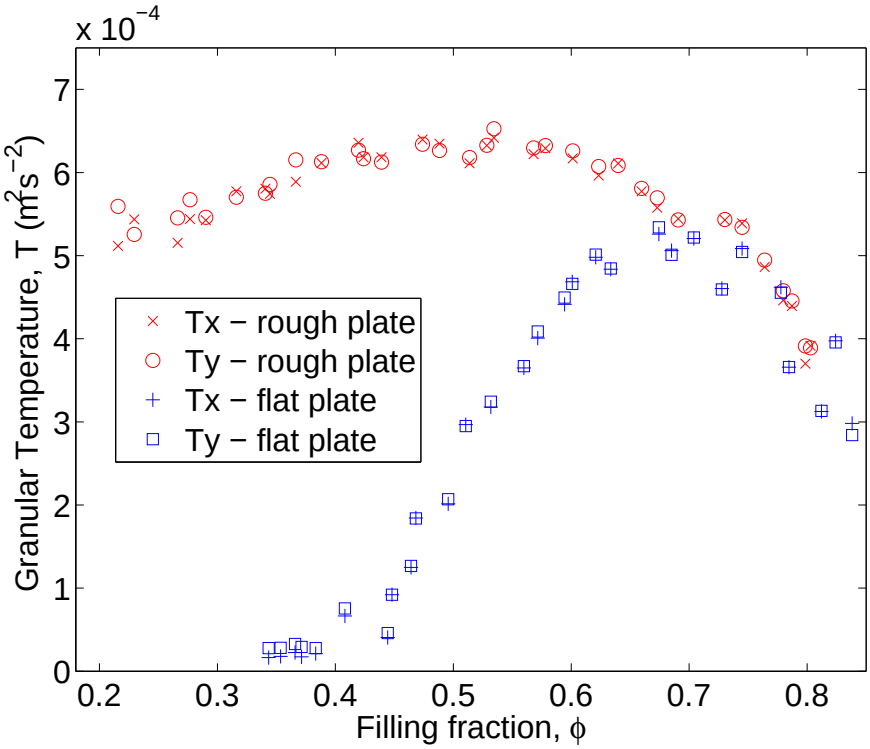

Figure 5.2: Filling fraction dependence of the granular temperature (T_x and T_y are the x and y components, respectively), for both cases of using a flat and rough bottom glass plates. Driving parameters: $f = 50Hz$ and $\Gamma = 4.0$.

depends almost monotonically on the filling fraction. At low ϕ, T is approximately constant as the layer simply feels the *thermal bath* and shows little increase in T until $\phi \sim 0.5$ is reached. As the filling fraction is increased past $\phi \sim 0.5$, the granular temperature rapidly decreases due to energy loss in the increasing number of collisions and due to a decreasing available volume.

For the case of using a flat bottom plate, the non-monotonic dependence of T on ϕ is more dramatic and it is difficult to attain homogeneous states below $\phi < 0.4$. This is due to the fact that at those filling fractions (the limiting case being the single particle investigated in the previous section) the particles perform small excursions and interact with their neighbors only sporadically. Hence, little momentum is transferred onto the horizontal plane. For $\phi > 0.5$, there is an increase of tem-

perature with increasing filling fraction as interaction between neighbors becomes increasingly more common, up to $\phi \sim 0.7$ after which the curve for the flat bottom plate coincides with the curve for the rough bottom plate. It is interesting to note that the value at which this matching occurs is close to the point of crystallization of disks in 2D, $\phi_c = 0.716$ (Alder & Wainwright 1962, Mitus et al. 1997, Reis et al. 2006). At this point, the large number of collisions between neighboring particles thermalizes the particles, independently of the details of the *heating*, i.e. of whether a flat or rough plate is used.

The behavior of the layer was therefore more robust by using a rough bottom plate. Moreover, this allowed for a wider range of filling fractions to be explored, in particular in the low ϕ limit. Hence, all results presented in the remainder of this chapter correspond to experiments for which a rough glass plate was used for the bottom plate of the experimental cell.

In Fig. 5.3 we present the dependence of the granular temperature of the layer on the forcing parameters for a fixed value of filling fraction, $\phi = 0.59$. There is a monotonic increase of T with both f and Γ.

The final control parameter that we investigated was the height of the experimental cell which we varied by changing the thickness of the inter-plate annulus by using precision spacers. The range explored was $1.3D < h < 2.3D$. Note that for $h = D$ there would be no clearance between the spheres and the glass plates and no energy would be injected into the system. On the other hand for $h > 2D$, spheres could overlap over each other and the system ceases to be quasi-2D. The dependence of the granular temperature on cell gap is plotted in Fig. 5.4. It is interesting to note that T appears to depend linearly on the gap height.

One can therefore regard changing h, f and Γ as a way of varying the temperature of the granular fluid, which can this way be tuned up to a factor of eight.

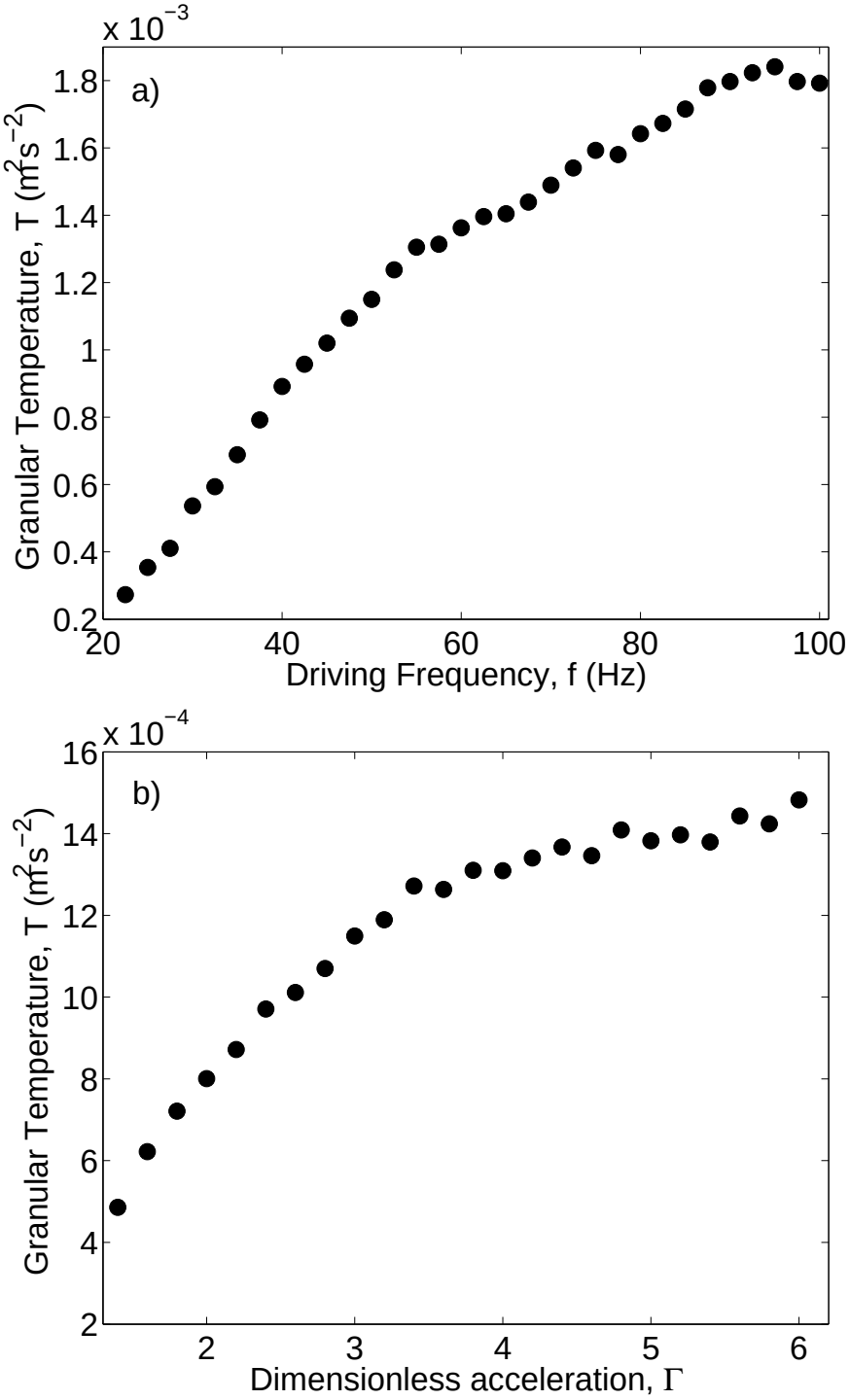

Figure 5.3: Dependence of the granular temperature, T, on driving parameters: (a) frequency, f and (b) dimensionless acceleration Γ. The filling fraction is kept constant at $\phi = 0.59$.

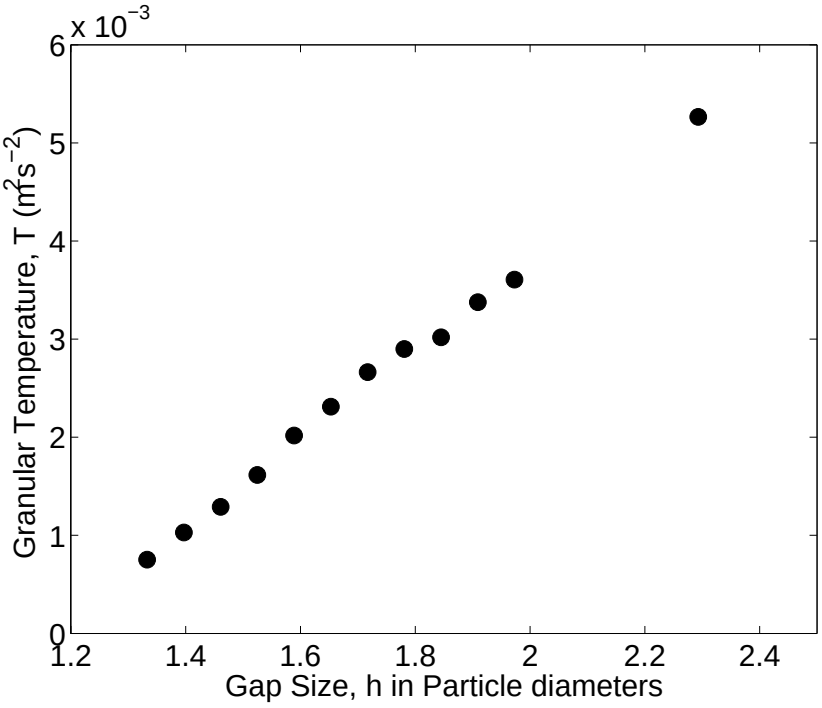

Figure 5.4: Dependence of the granular temperature, T, on cell gap, h, which was varied by changing the thickness of the inter-plate annulus. Filling fraction was kept constant at ϕ=0.59 and the dimensionless acceleration Γ was fixed to 4.

5.7 Probability density functions of velocities

We now turn to the distribution functions of particle velocities under various conditions of filling fraction, frequency, dimensionless acceleration and gap height. In Fig. 5.5 we plot the probability density function of a velocity component, $P(v_i)$, where the index i represents the component x or y, for specific values of ϕ, f and Γ. From now on we drop the index in v_i since we showed in the previous section that the dynamics of the system is isotropic in x and y (horizontal plane). Moreover, when we refer to *velocity* we shall mean *velocity component, i*. The width of the observed $P(v)$ differs for various values of the parameters. This is analogous to the fact that the temperature (i.e. the variance of the distribution) is different for various states set by ϕ, f and Γ, as discussed in the previous Section. It is remarkable, however,

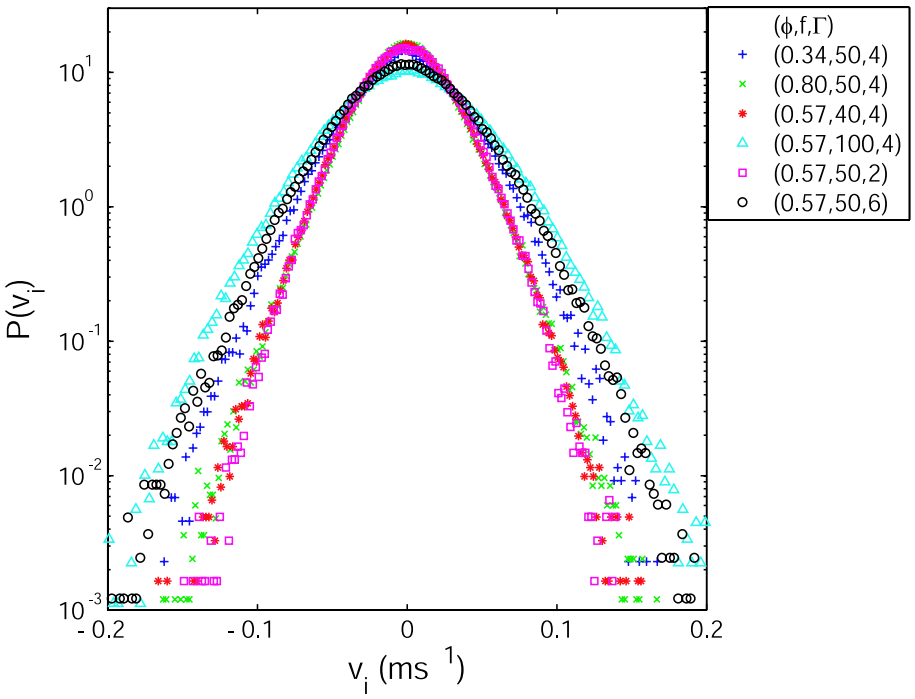

Figure 5.5: (a) Probability distribution function (PDF) of velocities, $P(v)$, for specific values of filling fraction (ϕ), frequency (f) and dimensionless acceleration (Γ). See legend for specific values.

that all the $P(v)$ distributions can be collapsed if the velocities are normalized by the characteristic velocity,

$$v_o = \sqrt{2\langle v^2 \rangle} = \sqrt{2T} \tag{5.15}$$

where the brackets $\langle . \rangle$ represent time and ensemble averaging over all the particles in the field of view of the imaging window. This collapse is shown in Figs. 5.6(a) and (b) and was accomplished not only for various filling fractions but also for a range of frequencies and dimensionless accelerations.

To highlight the quality of the collapse we have separately plotted $P(c)$ for the four lowest values of filling fraction ($\phi = 0.27, 0.32, 0.34, 0.39$) along with the $P(c)$ for a single particle in Fig. 5.6(a) and all other data in the ranges $0.44 < \phi < 0.8$, $40Hz < f < 100Hz$ and $1.4 < \Gamma < 6$ in Fig. 5.6(b). At low values of the filling fraction ($\phi < 0.44$) the collapse is satisfactory but deviations are seen at low c.

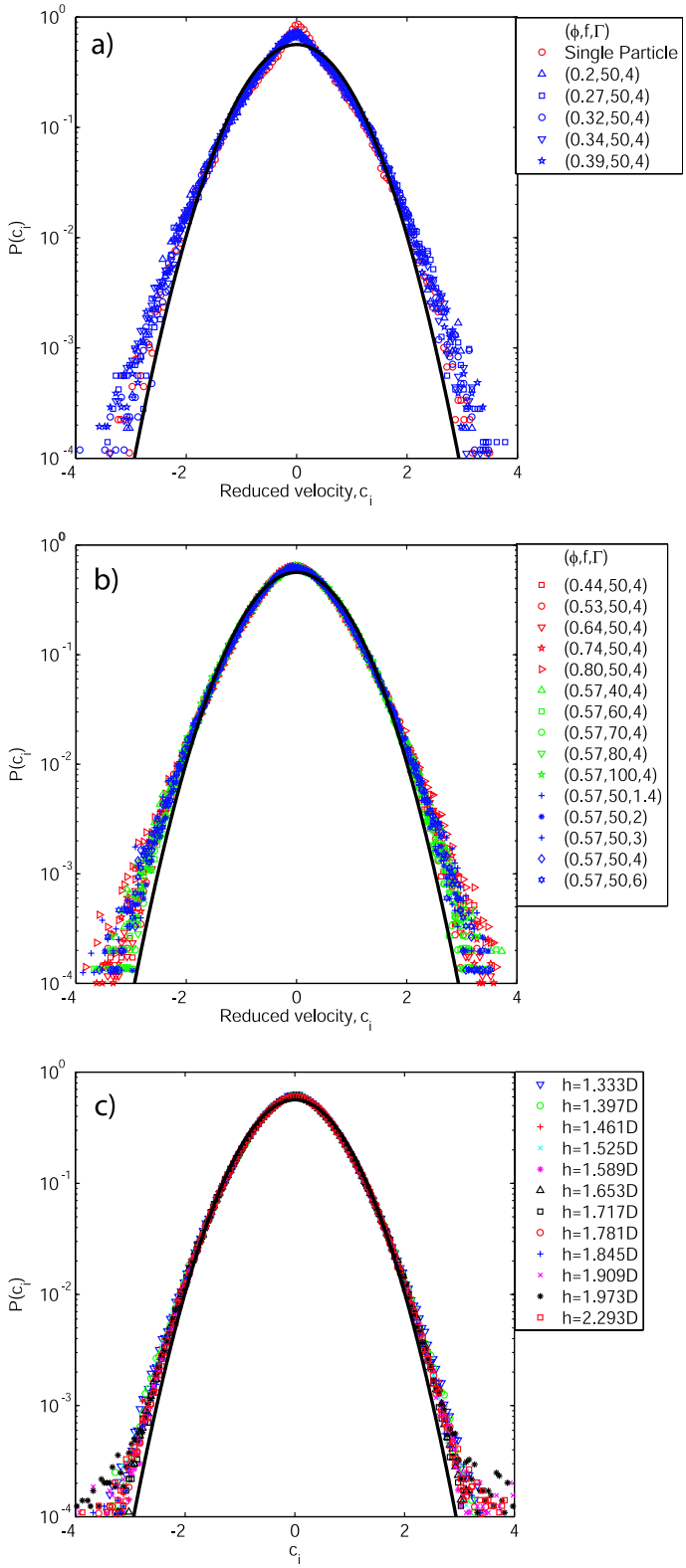

Figure 5.6: (a)-(b)PDF of velocities, $P(c)$, in which all velocities for each distribution were normalized by its standard deviation. Data for a range of ϕ, f and Γ. (c) PDF of velocities for range of values of cell gap, h. Other parameters set to $\phi = 0.59$, $f = 50Hz$ and $\Gamma = 4.0$. (a-c) See legend for specific values of the experimental parameters. The solid line in each plot is a Gaussian with unit standard deviation.

In particular, near $c = 0$ the distributions exhibit a sharp peak with a clearly discontinuous first derivative which reflects the fact that for these value of low ϕ the resulting gases are not collisionally driven but are influenced instead by the underlying thermostat. However, this sharp peak becomes increasingly smoother as the filling fraction is increased, presumably due to the increasing number of particle collisions, and by $\phi \sim 0.44$, it has practically disappeared. On the other hand, for $\phi > 0.44$ the collapse onto a universal curve is remarkable for such a wide range of ϕ, f and Γ. The choice of the lower bounds for frequency and acceleration, $f = 40Hz$ and $\Gamma = 1.4$, in the data plotted will be addressed in Sec. 5.7.2. Moreover, this collapse of $P(v)$ is also attained for various values of the gap height ($1.3D < h < 2.3D$), as shown in Fig. 5.6(c). From now onwards, we shall perform our analysis in terms of the reduced velocity, $c = v/v_o$.

We stress the universal collapse of the experimental velocity distribution functions for a wide range of parameters and the clear deviation from the Maxwell-Boltzmann (Gaussian) distributions of Eqn. (5.10) – solid curves in Fig. 5.6(a-c). This is particularly visible at high velocities where there is a significant overpopulation of the distribution tails in agreement with previous theoretical (van Noije & Ernst 1998), numerical (Moon et al. 2001) and other experimental work (Rouyer & Menon 2000, Aranson & Olafsen 2002, van Zon, Kreft, Goldman, Miracle, Swift & Swinney 2004). To quantify these deviations from Gaussian behavior, our analysis will be twofold. First we shall analyze the non-Gaussian tails of the velocity distributions (Sec. 5.7.1). Even though these tails correspond to events associated with large velocity, the probability of them happening is extremely low. However, this overpopulation at the tails implies that, if the distribution is to remain normalized with a standard deviation given by the average kinetic energy per particle, clear deviations from Gaussian at the central regions of low c (high probability) of the distribution must necessarily also be observed. In Sec. 5.7.2 we study this deviations

in the context of the Sonine corrections introduced in Sec. 5.4.

5.7.1 Deviation at large velocities – The tails

Recently, van Noije and Ernst (van Noije & Ernst 1998) have made the theoretical prediction that the high energy tails of the velocity distributions of a granular gas *heated* by a stochastic thermostat should scale as stretched exponentials of the form,

$$P(c) \sim \exp\left(-Ac^{3/2}\right), \tag{5.16}$$

where A is a fitting parameter. Note that the theoretical argument of van Noije and Ernst involves a high c limit and hence one does not expect this stretched exponential form to be valid across the whole range of the distribution.

To check the applicability of Eqn. (5.16) to describe our data, we have calculated the quantity $q(c) = -\ln\left(-\ln(P(c))\right)$, which we plot in Fig. 5.7(a) for a variety of filling fractions, frequencies and dimensionless accelerations. Indeed, within the ranges considered and, in the limit of large c, $q(c)$ tends to a straight line with slope -3/2 for all values of the control parameters, in excellent agreement with the scaling of Eqn. (5.16). In Fig. 5.7(a) we have excluded filling fractions $\phi < 0.44$, since as discussed in the previous Section, the gases obtained in this range are dominated by the thermostat rather than collisions and the main ingredient for the prediction of Eqn. (5.16) is the role of inelastic collisions. This behavior of the tails of the velocity distribution is also observed for various values of the gap height, h, of the experimental cell, as shows in Fig. 5.7(b). Note the crossover from Gaussian-like (dashed line with slope -2) to the stretched exponential (solid line with slope -3/2) at $c \sim 1$, which is particularly clear at the larger values of ϕ. For low ϕ the tails of the distribution tend to be closer to the stretched exponential throughout the range $-1.1 < \log(c) < 1.1$. We stress that Eqn. (5.16) has been derived in the limit of large c and is therefore only expected to be valid at the large c end of the tails. This theoretical work says however nothing about the value of velocity, c_o, above

which such tails should be observed. There is, at present, no theory that predicts the value of the crossover, c_o.

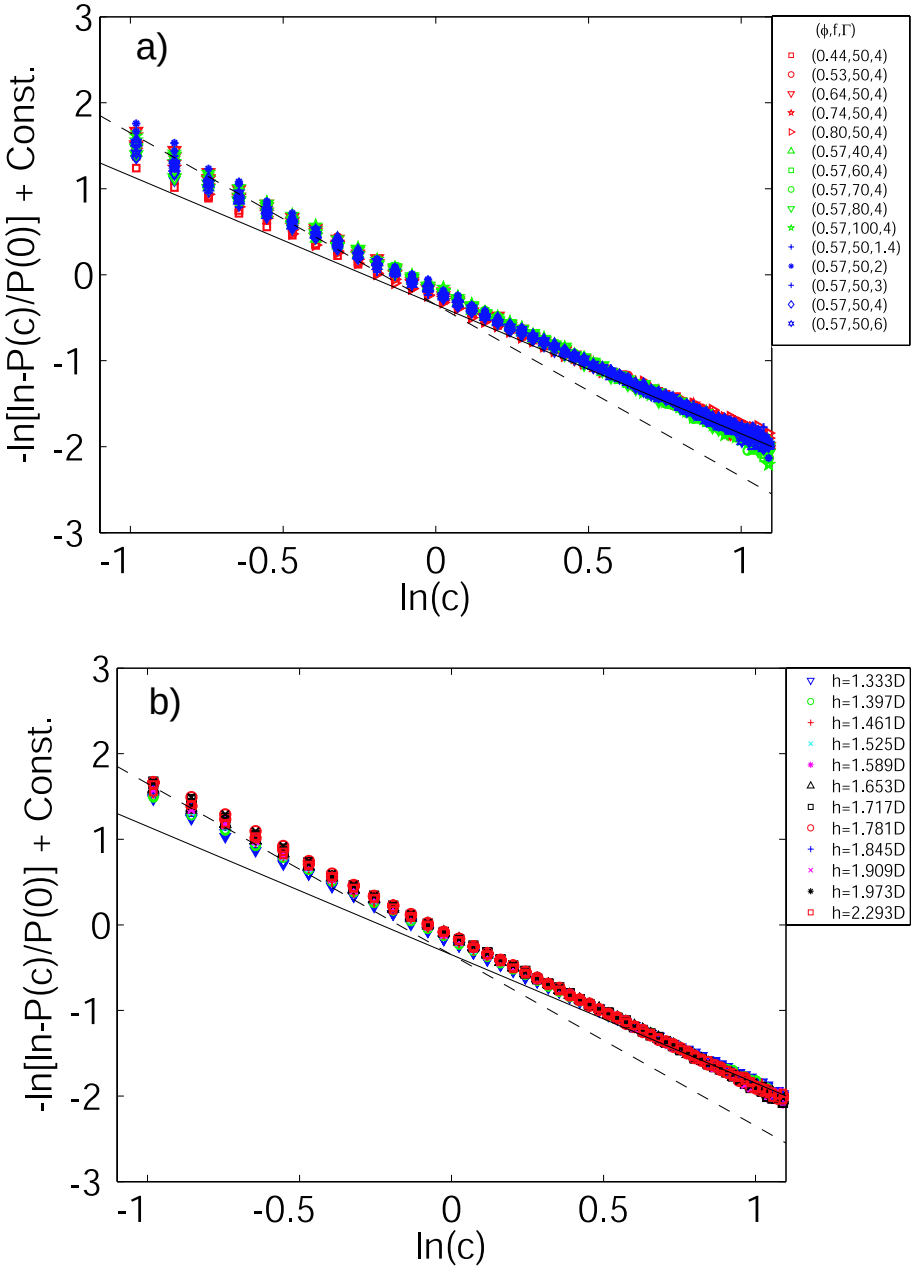

Figure 5.7: (a) Tails of $P(c)$ for specific values of filling fraction (ϕ), frequency (f) and dimensionless acceleration (Γ) and (b) gap height (h).The solid lines correspond to stretched exponentials of the form $\sim \exp(-Ac^{3/2})$ whereas the dashed lines correspond to the Gaussian behavior of the form $\sim \exp(-Ac^2)$.

The c_o that we observe in our experiments ($c_o^{exp} \sim 1$ which corresponds to probabilities of occurrence of the order of $P(c)/P(0) \sim 10^{-1}$) is systematically higher than that found in molecular dynamics simulations of inelastic hard spheres, *e.g.* that of Moon *et. al.* (Moon et al. 2001). Our results are, however, in agreement with other experimental work (Rouyer & Menon 2000). In the previously mentioned numerical work by Moon *el. al.* the cross-over occurs at the slightly higher values of $0.5 < \ln c_o^{sim} \sim 1.5$ which correspond to probabilities of the order of $10^{-3} < P(c_o)/P(o) < 10^{-2}$. It is interesting to note that the cross-over for both experiments and molecular simulations is, however, occurring at probabilities 3 to 5 orders of magnitude larger than the value of $P(c_o)/P(o) \sim 10^{-6}$ proposed by Barrat *et. al.* (Barrat & Trizac 2003, Barrat, Trizac & Ernst 2005) using the Direct Simulation Monte Carlo (DSMC) method. Even though experiments, molecular dynamics and DSMC simulation are all in agreement with van Noije and Ernst stretched exponential tail result (i.e. such tails exists), there is a clear inconsistency regarding its range of validity, i.e. the location of the crossover which cannot be accounted for by any existing theory.

We expect the location of c_o to be a function of the strength and frequency of the forcing as well as the inter-particle coefficient of restitution. The dependence on the first two parameters (frequency and strength of forcing) should be related to the q-parameter recently introduced by van Zon & MacKintosh (2004). The dependence on the coefficient of restitution, ϵ, was shown to be relevant by Moon *et. al.*). There is therefore a need for new theoretical work that takes q and ϵ into account to predict the location of c_o in experiments. We hope that our experimental results will be motivating in this direction.

5.7.2 Sonine corrections to the distribution

Having looked at the tails of the distributions, i.e. at large c, we now extend our deviation analysis based on an expansion method to the full c range of the distributions. In particular, this highlights the deviations from Gaussian behavior in the central high probability regions of $P(c)$ near $c = 0$. In Sec. 5.4 we discussed that in the solution of the Enskog-Boltzmann equation for inelastic particles in a stochastic thermostat, a Sonine expansion is usually performed such that the deviations from Gaussian are described by a Sonine Polynomial (i.e. a 4th order polynomial with well defined coefficients) multiplied by a numerical coefficient a_2.

To check the validity of this assumption of the Kinetic Theory, we shall follow a procedure analogous to that employed in the numerical study of Ref. (Moon et al. 2001). We calculate the deviation, $\Delta(c)$, of the experimental velocity distributions, $P(c)$, from the equilibrium Maxwell-Boltzmann, f_{MB}, such that,

$$P(c) = f_{MB}\left(1 + \Delta(c)\right), \tag{5.17}$$

where f_{MB} is given by Eqn. (5.10). By comparing Eqn. (5.17) to Eqn. (5.9) for the theoretical case of inelastic particles under a stochastic thermostat, we expect that

$$P(c) = f_{MB}(1 + a_2 S_2(c^2)), \tag{5.18}$$

such that the experimental deviations from equilibrium take the form of the Sonine polynomial of order-two, $S_2(c^2)$, i.e.

$$\Delta(c) = a_2\left(1/2c^4 - 3/2c^2 + 3/8\right), \tag{5.19}$$

where the parameter a_2 can be directly related to the kurtosis K of the distribution as $a_2 = K/3 - 1$. However, because of sampling noise at high c, we have taken a_2 as a fitting parameter rather than determining it directly from K, although in most cases there is little difference. Note that the fitting of the experimental data

to Eqn. (5.18) was done over the whole range of the distribution, which gives an intrinsic weighting proportional to the probability. In Fig. 5.8(a–d) we plot these experimental deviation from equilibrium, $\Delta(c)$, for four representative values of filling fraction, along with the order-2 Sonine polynomial (solid curve) as given by

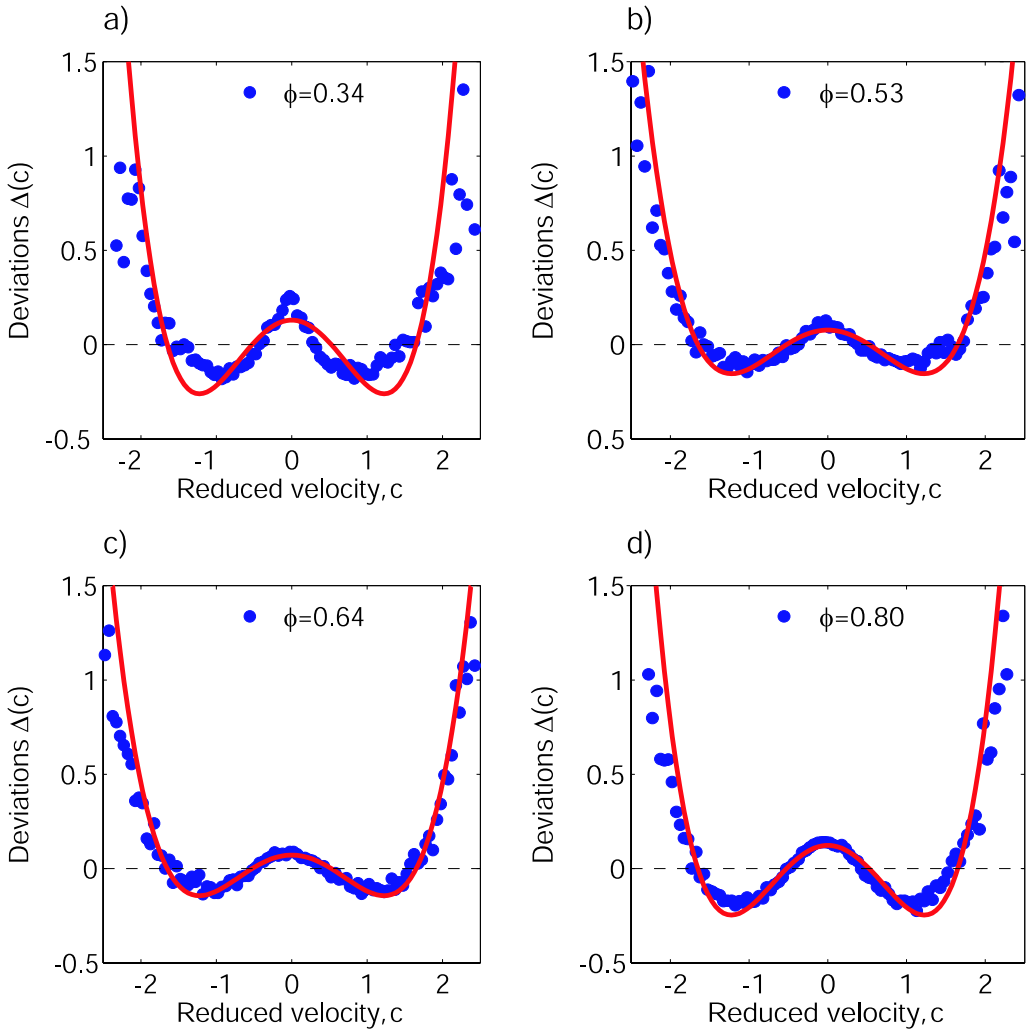

Figure 5.8: Experimental deviation function from Gaussian behavior, $\Delta(c)$ for (a) $\phi = 0.34$, (b) $\phi = 0.53$, (c) $\phi = 0.64$ and (d) $\phi = 0.80$. The solid line is the order-two Sonine polynomial of the form $a_2(1/2c^4 - 3/2c^2 + 3/8)$ where a_2, the second Sonine coefficient, is the only adjustable parameter .

Eqn. (5.19) and fitting for a_2. At low filling fractions, for example $\phi = 0.34$ – Fig. 5.8(a) – the second order Sonine fit is approximate but unsatisfactory for small c

where a sharp cusped peak is present. This cusp is reminiscent of the underlying dynamics of the rough plate thermal bath. On the other hand, for larger values of the filling fraction (in particular for $\phi > 0.44$) the experimental data is accurately described by the second order Sonine polynomial.

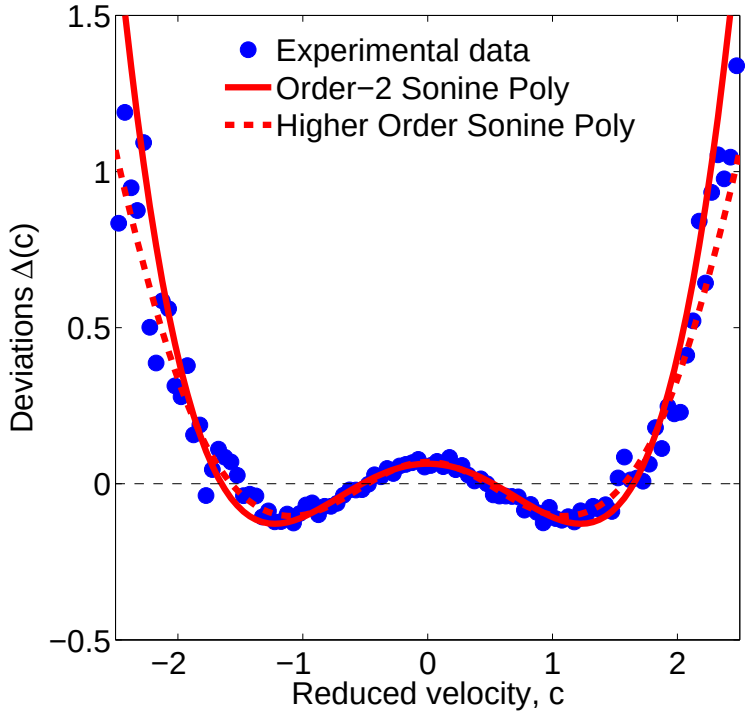

Figure 5.9: Experimental deviation function from Gaussian behavior, $\Delta(c)$ for $\phi = 0.66$. The solid line is the Sonine polynomial $a_2(1/2c^4 - 3/2c^2 + 3/8)$ with one single fitting parameter: $a_2 = 0.171$. The dashed line is the higher order Sonine polynomial description of the form $\sum_{p=2}^{6} a_p S_p(c^2)$ with the following (five fitting parameters) Sonine coefficients; $a_2 = 0.1578$, $a_3 = -0.0656$, $a_4 = 0.1934$, $a_5 = -0.1637$ and $a_6 = 0.0832$.

To further evaluate the relevance of the Sonine polynomials to describe the experimental deviation from Maxwell-Boltzmann, in Fig. 5.9 we plot the experimental $\Delta(c)$ along with both the order-two ($p = 2$) Sonine polynomial and the higher order Sonine expansion of the form $\sum_{p=2}^{6} a_p S_p(c^2)$. The second order Sonine polynomial alone is responsible for the largest gain in accuracy of the corrections from MB (hor-

izontal dashed line). The higher order Sonine expansion indeed provide a better fit but the overall improvement is only marginal (see Fig. 5.12.)

In Fig. 5.10(a) we present the dependence of the second Sonine coefficient a_2, the single fitting parameter in Eqn. (5.19), as a function of filling fraction. The

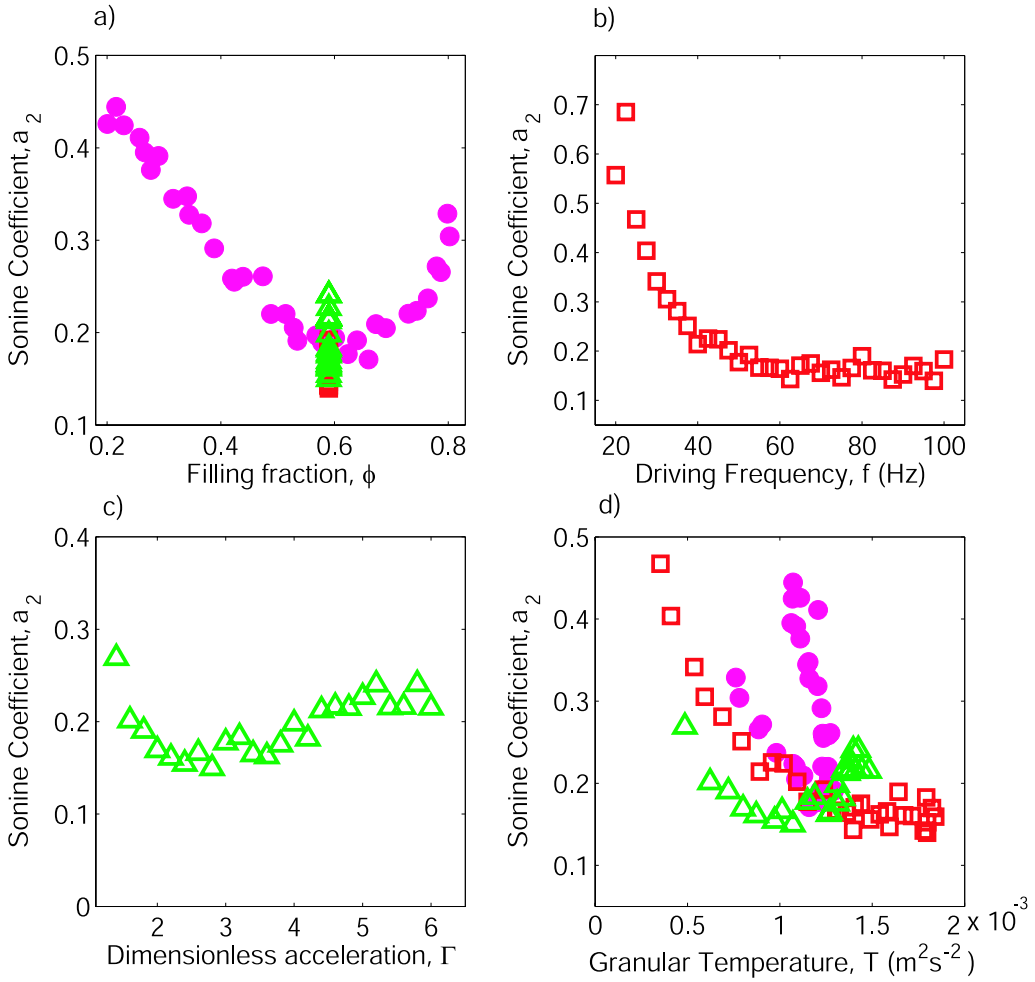

Figure 5.10: Experimentally determined order-two Sonine coefficient a_2 as a function of (a) filling fraction (●), (b) driving frequency (□), (c) dimensionless acceleration (△) and (d) granular temperature. The filling fraction is kept constant at $\phi = 0.59$ while exploring the dependence of a_2 on f and Γ.

coefficient a_2 initially decreases with increasing filling fraction up to $\phi = 0.65$, after which it shows a rapid rise. We also study the dependence of a_2 on the driving frequency (f) and dimensionless acceleration (Γ) for a single value of the filling fraction

$\phi = 0.59$, which we present in Figs. 5.10(b) and (c), respectively. For lower values of frequency (20-40Hz) we get a monotonic drop in a_2 with increasing frequency. For $f > 40Hz$, the coefficient a_2 then levels off and remains approximately constant at $a_2 = 0.171 \pm 0.023$. For $\Gamma > 2.0$, the coefficient a_2 remains approximately constant at $a_2 = 0.193 \pm 0.029$. We have plotted these two datasets at fixed ϕ and varying f and Γ back in Fig. 5.10(a) and the behavior of a_2 is found to be consistent with the previous dataset with varying ϕ at fixed $(f, \Gamma) = (50Hz, 4.0)$. It is interesting to note that a scatter of points is obtained if a_2 for the three previous datasets is plotted as a function of the corresponding granular temperatures. Moreover, for the data-set for varying ϕ the dependence is clearly not single valued, i.e. one can find two distinct values of a_2 for a single value of temperature. All this suggests that the temperature does not set a_2. Instead, a_2 is a strong function of ϕ and is only weakly dependent on f and Γ, provided that $f > 40Hz$ and $\Gamma > 2$. This is in agreement with inelastic hard-sphere behavior where the only two relevant parameters are thought to be the filling fraction and the coefficient of restitution (not investigated in the present study).

Next, in Fig. 5.11 we present the dependence on filling fraction of the experimentally determined five non-zero Sonine coefficients in the sixth order expansion of $\Delta(c) \sim \sum_{p=2}^{6} a_p S_p(c^2)$. In the theoretical analysis, the higher order terms (order 3 and above) in the Sonine polynomial expansion are typically neglected to simplify the calculations, the claim being that this results in no significant loss of accuracy. In our experimentally generated fluids the higher order Sonine coefficients assume values less than 1 for filling fractions above $\phi = 0.5$. From this it is clear that it is unnecessary to consider orders higher than two for intermediate and high filling fractions. For $\phi < 0.5$, however, they are significant and the finite values of a_3,..., a_6 are required to fit the increasingly larger regions of stretching exponential tails which become progressively more wider and propagate towards smaller velocities.

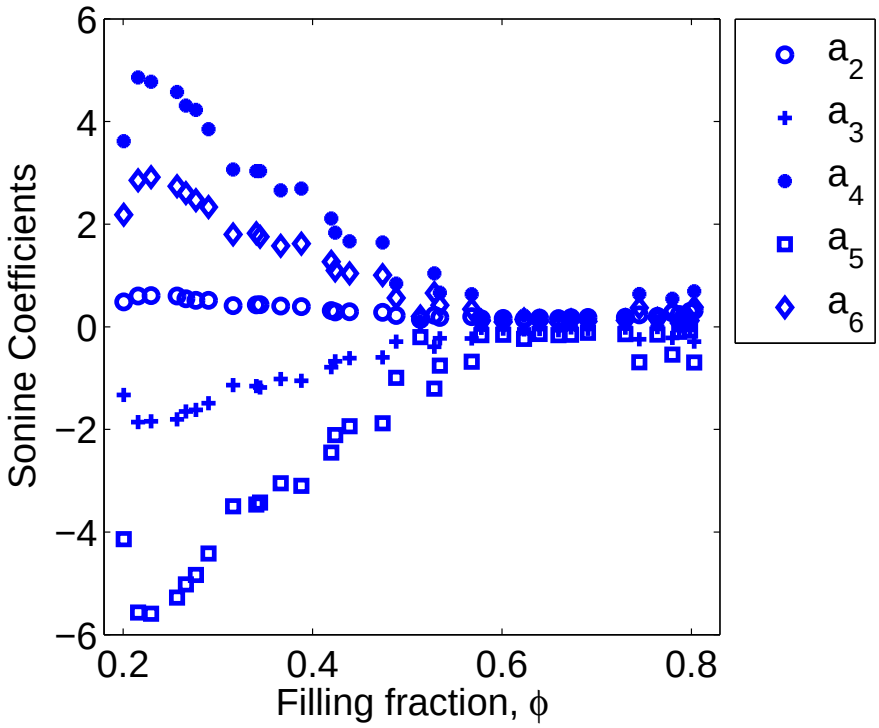

Figure 5.11: Dependence of higher order coefficients of the Sonine expansion (a_2 to a_6) on filling fraction.

As we mentioned in the discussion of Fig. 5.7(a) in the previous Sec., when the filling fraction decreases, the dynamics of the layer starts resembling that of the underlying thermal bath set by the rough plate. There the distribution, becomes increasingly more like a stretched exponential throughout the full c range, rather than only in its tails as is the case at larger values of ϕ. This finding is analogous to a result from Brilliantov and Pöschel (Brilliantov & Poschel 2006) who found both theoretically and numerically that the magnitude of the higher-order Sonine coefficients can grow due to the an increasing impact of the overpopulated high-energy tails of the distribution function, just like in our system at low ϕ. Their analysis was however performed as a function of the coefficient of restitution, ϵ, rather than filling fraction. In their study a single second order Sonine polynomial becomes insufficient to represent the deviation from Gaussian at low values of ϵ.

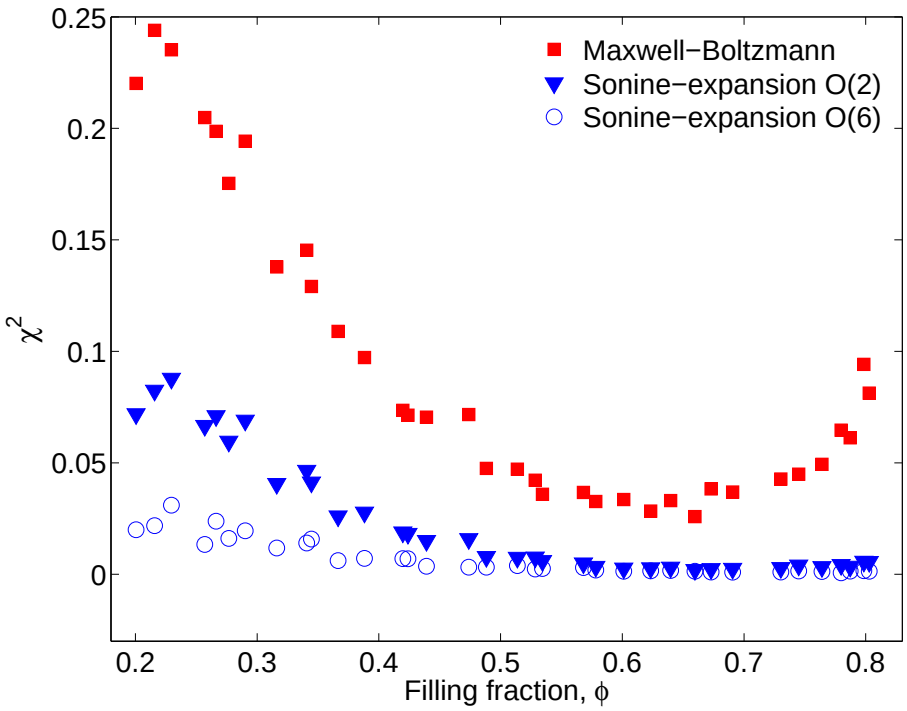

Figure 5.12: Deviations (quantified by χ^2), as a function of filling fraction, of the experimental velocity distributions from Maxwell-Boltzmann distribution ($\square$), from the velocity distribution function with a order-two Sonine polynomial correction ($\triangledown$) and from the velocity distribution function with a order-six Sonine polynomial expansion correction ($\circ$) .

Moreover, they worked on the Homogeneous Cooling State (HCS), but they suggest that their results should also apply to granular gases with a thermostat, like in our case. A more direct comparison with this theoretical analysis is open to further investigation.

We stress that a finite value of the higher order coefficients does not necessarily imply a large correction to the deviations $\Delta(c)$. To explore further this point we now quantify the deviations of our experimental velocity distribution from all the three models we have considered: 1) the equilibrium Maxwell-Boltzmann distribution, 2) the velocity distribution function with order-2 Sonine polynomial expansion and, 3) the velocity distribution function with higher order Sonine polynomial terms. In

Fig. 5.12 we plot these deviation of experiments from the models as quantified by $\chi^2 = \sum_{i=1}^{N}(P(c_i)_{exp} - P(c_i)_{model})^2$, for the full range of filling fractions. We clearly see significant deviation of the experimental data from Maxwell-Boltzmann distribution for all ϕ, whereas the velocity distributions with the order-2 Sonine polynomial term shows a considerably better agreement with the experimental data across the whole range of ϕ. Even though the higher order Sonine polynomial expansion characterizes the experimental data more closely, these higher order contributions are modest compared with the large gain in accuracy from the order-2 Sonine polynomial alone, and in the range of $\phi > 0.44$ provide no significant improvement. Thus the order-2 description obtained by neglecting the higher order Sonine terms is a reasonably good approximation to describe the experimental data.

It may seem counter-intuitive that the Sonine-like deviation appear to work better at higher values of filling fractions ($\phi > 0.45$), whereas one might expect this formalism to be more effective at low filling fractions. To address this issue we now comment on the issue of energy injection into the granular fluid. For finite filling fractions the dynamics, and hence the temperature, of the granular fluid is set by a balance between the energy flow into the system (through the effective thermostat) and the inelastic inter-particle collisions. At low filling fractions we expect the dynamics to be thermostat dominated and at high filling fractions for it to be collision dominated. At these higher values of ϕ there are a large number of inelastic collisions (higher collision rate) which is the main ingredient for the theoretical model presented and reviewed in Sec. 5.4. Hence, the Sonine formalism works well in that region. For $\phi < 0.45$, the dynamics is mostly thermostat dominate (over the inter-particle inelastic collisions) and hence, since we don't have a perfect Gaussian thermostat, we expect more deviations from Gaussian.

van Zon & MacKintosh (2004) have recently introduced a method for quantifying this relative importance between particle-substrate interaction (heating) and

particle-particle interactions (collisions). They introduced a new parameter $q = N_H/N_C$, where N_H and N_C are the average number of heating and collision events, respectively. For $q > 1$ heating dominates the dissipative collisions and vice versa for $q < 1$. Whereas we can easily estimate N_C from our particle tracking data, measuring N_H is considerably more challenging as it would require information along the z-direction on the vertical motion of the particles along with the knowledge of the collisions with the rough bottom plate. At present, with our current experimental technique, we are unable to measure N_H but it would be of great interest to address this question in future work. Being able to measure q for the various system parameters would allow one to establish what features of the dynamics are thermostat or inelastic collisionally driven. In particular, it would be of interest to measure the Sonine coefficient a_2 as a function of q for the various experimental parameters. We hope that our work will drive further research in that direction.

5.8 Conclusion

In conclusion, we have developed an experimental model system for a quasi-2D granular layer, under homogeneous stochastic driving. Our experimental technique has allowed us to randomly thermalize a granular fluid over a wide range of filling fractions. Our study was centered on the dynamics of the system, in particular the statistics of velocities. The temperature of the experimental granular fluid could be adjusted by varying the system's control parameters, namely the filling fraction, the frequency and acceleration of the driving and the gap height, with no significant change in the nature of the velocity probability distribution functions. We have found an excellent collapse of the distribution functions if the particle velocities are scaled by a characteristic velocity v_o (the standard deviation of the distributions).

However, the obtained distribution are non-Gaussian. We have analyzed the deviations from Gaussian behavior in two distinct regimes. Firstly, we looked at

the shape of the distribution tails which scaled as stretched exponentials with exponent 3/2. Secondly, we have performed an expansion method that highlights the deviations from a Gaussian at low velocities (near $c = 0$) and found them to be Sonine-like, i.e. polynomial of order four with fixed coefficients. It is surprising that this formalism seems applicable at filling fractions as high as $\phi = 0.80$, whereas Kinetic Theory is usually thought to breakdown at much lower values of ϕ. Finally, we have looked at the Sonine polynomial expansion with higher order terms and concluded that it is sufficient to retain only the leading order (first non-vanishing) term to maintain reasonable accuracy. Therefore, we can accurately characterize the single particle velocity distribution function by introducing a single extra coefficient a_2, in addition to the 0th, 1st and 2nd moments used for fluids at equilibrium. The coefficient a_2 has universal character in the sense that it is a strong function of filling fraction and only depends weakly on the other experimental parameters such as the driving frequency and acceleration.

To our knowledge, this is the first time that the Sonine corrections of the central high probability regions of the velocity distributions have been measured in an experimental system, in agreement with analytical predictions. This should open way to further theoretical developments, crucial if we are to develop much desired predictive models for granular flows with practical relevance.

Chapter 6

Conclusions and Future Work

6.1 General concluding remarks

We have presented a detailed investigation of the solid-fluid transition in vibrated granular matter under constant pressure and constant volume conditions.

For the isobaric case and integer number of rows, both our 2D and 3D granular system exhibit a first order freezing/melting phase transition. The phase transition is characterized by discontinuous changes in density and temperature and shows hysteretic effect. The hysteresis disappears for sufficiently slow heating rate and is analogous to the superheating or supercooling phenomena established for ordinary fluids. We also proposed a phenomenological model to explain the observed phase transition which shows good agreement with the experimental results. The model behavior is analogous to the Ginzburg-Landau free energy formalism commonly used to explain phase transition phenomena in equilibrium systems (Gracheva et al. 2000).

For the isochoric granular system, we primarily focussed on investigating and quantifying the structural changes in the quasi-2D uniformly heated granular fluid near the crystallization phase transition. Olafsen & Urbach (2005) have studied the melting of a horizontal monolayer of spheres confined between two vibrating plates and found a continuous transition from a hexagonally ordered solid phase

to a disordered liquid. Our experimental results for the Lindemann criterion for melting, the radial distribution function, the bond order parameter and the statistics of topological changes at the particle level show remarkably good agreement with the behavior of equilibrium hard disks. Further, the observed phase transition can possibly be explained using the geometrical mechanism of square-triangular tiling which forms the basis for models describing the 2D equilibrium melting transition (Kawamura 1983). The velocity statistics study of uniformly heated system supports the kinetic theory treatment of granular fluids based on analogy with molecular fluids using statistical mechanics approach.

These findings suggest that granular systems may not be entirely different from ordinary equilibrium systems. In fact, we can effectively use the fundamental framework established for equilibrium systems to study non-equilibrium granular systems. However, we need to suitably incorporate the non-equilibrium effects like energy injection and dissipation in the new modified formalism for granular systems. Thus our results open many interesting new avenues for advancing the physics of granular matter.

6.2 Future work

Specific thoughts about directions for future work are discussed below.

1. In the present study we investigated in great detail an ideal monodisperse granular system. One natural extension of the current work would be to introduce bidispersity or polydispersity in the system and study its effect on the phase transition characteristics, both in 2D and 3D. This study would be more relevant to real world granular systems where particle size distribution is a common occurrence.

2. Secondly, it would be interesting to use two types of particles of the same

material and size, the only difference being the roughness of the particles. This difference would lead to differential energy injection at the particle level and may lead to interesting phenomena. For smooth monodisperse systems, crystallization occurs as one changes (increases) the filling fraction. However, we would like to see the effect of surface roughness on the phase transition phenomena. This result would be of special relevance to granular systems where friction plays an important role in determining the dynamics of the system.

3. Another direction is the exploration of particle shape and particle type on the phase transition behavior. We currently use high precision stainless steel spherical particles. It would be interesting to use various other materials like glass beads, acrylic, ceramic or teflon particles for the phase transition studies. The particle-particle interactions play an important role in granular systems. By changing the particle shape or particle type, we can alter the particle-particle interactions. We thus believe that particle shape/type would play a crucial role in determining the phase transition characteristics of the granular system.

4. In future studies we would also like to focus on the issue of control parameter for phase transition. The non-dimensionless acceleration (Γ) is the most commonly used system parameter to quantify the onset of phase transition in granular systems. However, we find that the first-order phase transition for identical systems occurs at different Γ if the driving frequency is changed (Section 2.8). The data collapse when plotted against the maximum driving velocity. This suggests that Γ may not be a satisfactory control parameter and we need to explore other possibilities like the velocity or the energy flux as an improved measure for the control parameter.

Appendix A

Voronoi tessellation

Voronoi construction, also know as Wigner-Seitz cells, are a standard tool for the study of spacial configurations of particle ensembles and is widely used in condensed matter physics (Okabe, Boots, Sugihara & Chiu 2000). The Voronoi construction or tessellation for a given set of points is a numerical method which enables estimates of the area density associated with individual spheres to be made. The method may be defined as follows and is illustrated in the schematic diagram of Fig. A.1, for the case of a central particle labelled C_1, surrounded by six neighbors. Consider a set P of coplanar particles ($P = C_1; C_2; C_3; C_4; C_5; C_6; C_7$) for the example in Fig. A.1. Lines are drawn from the center of a particle to each of its nearest neighbors (lines $\overrightarrow{C_1C_i}$ for each pair of particles 1 and i = 2 to 7) and halved to yield the mid points, H_{1i}. The lines h_i are then defined to be perpendicular to the joining vectors $\overrightarrow{C_1C_i}$ and passing through H_1i. The intersect between each pair of the lines h_i gives the vertices V_{lm} (with $m = l + 1$) which defines a polygonal cell, centered at C_1. This cell encloses a region (shown in pink in Fig.) in which any point is closer to C_1 than to any other particle - this is the Voronoi cell of particle 1. We have used the Voronoi(x,y) routine in the numerical package MATLAB 7.0.1 to implement this procedure.

Using the Voronoi construction we can estimate properties such as, local Voronoi area density and shape factor. The local Voronoi area density of the i^{th} particle can

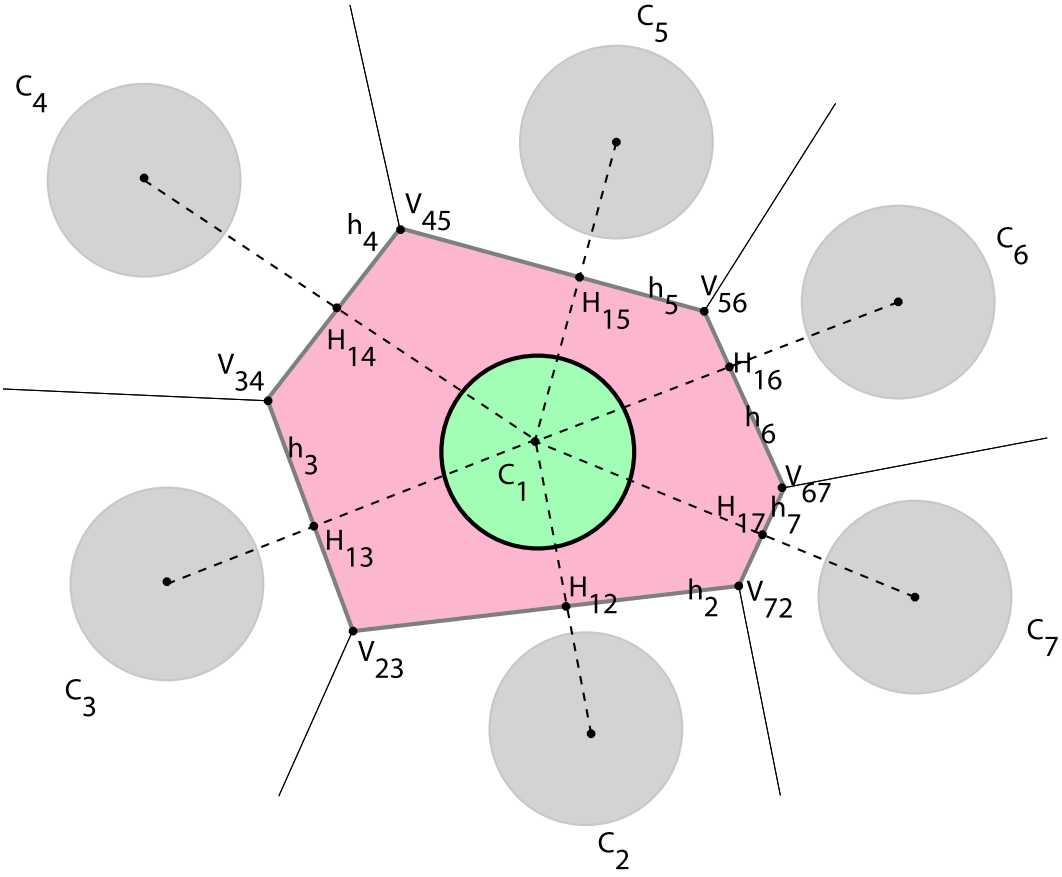

Figure A.1: Definition of the Voronoi cell of particle positioned at C_1 (shown in green) with six neighbors (shown in grey with indices $i = 2$ to 7). The polygon in pink is the Voronoi cell associated with the particle in green and is enclosed by the vertices V_{ij} . The boundaries of the Voronoi cell are the segments of the lines h_i. Each of the points H_{1i} is the mid point between C_1 and the respective particle i.

be defined as the ratio,

$$\rho^i = \frac{A_{particle}}{S} \tag{A.1}$$

where $A_{particle} = \pi/4D^2$ is the two dimensional projected area of the imaged sphere with diameter D and S is the area of its Voronoi polygon. To characterize the Voronoi cells we define the shape factor as

$$\zeta = \frac{C^2}{4\pi S} \tag{A.2}$$

where C is the circumference of the Voronoi cell, i.e., total length of its edges, and S is the surface area of the Voronoi cell.

Bibliography

Alder, B. J. & Wainwright, T. E. (1962), 'Phase transition in elastic disks', *Phys. Rev.* **127**, 359.

Alder, B. J., Hoover, W. G. & Young, D. A. (1968), 'Studies in molecular dynamics. v. high-density equation of state and entropy for hard disks and spheres', *J. Chem. Phys.* **49**, 3688.

Aranson, I. S. & Olafsen, J. S. (2002), 'Velocity fluctuations in electrostatically driven granular media', *Phys. Rev. E* **66**, 061302.

Augenstein, D. A. & Hogg, R. (1978), 'An experimental study of the flow of dry powders over inclined surfaces', *Powder Technol.* **19**, 205.

Bagnold, R. A. (1941), *The Physics of Blown Sand and Sand Dunes*, Chapman and Hall, London, U.K.

Bagnold, R. A. (1954), *Proc. R. Soc. London A* **225**, 49.

Bagnold, R. A. (1966), *Proc. R. Soc. London A* **295**, 219.

Barrat, A. & Trizac, E. (2003), 'Random inelasticity and velocity fluctuations in a driven granular gas', *Euro. Phys. J. E* **11**, 99.

Barrat, A., Loreto, J. K. V. & Sellitto, M. (2001), 'Edwards' measures: A thermodynamic construction for dense granular media and glasses', *Phys. Rev. E* **63**, 051301.

Barrat, A., Trizac, E. & Ernst, M. H. (2005), 'Granular gases: dynamics and collective effects', *J. of Phys: Condens. Matt.* **17**, S2429.

Bell, T. (2005), 'Challenges in the scale-up of particulate processesan industrial perspective', *Powder Technol.* **150**, 60.

Bernal, B. (1964), 'The bakerian lecture, 1962: the structure of liquids', *Proc. Roy. Soc.* **A 280**, 299–322.

Blair, D. L. & Kudrolli, A. (2001), 'Velocity correlations in dense granular gases', *Phys. Rev. E* **64**, 050301(R).

Blair, D. L. & Kudrolli, A. (2003), 'Collision statistics of driven granular materials', *Phys. Rev. E* **67**, 041301.

Bocquet, L., Losert, W., Schalk, D., Lubensky, T. C. & Gollub, J. P. (2001*a*), 'Granular shear flow dynamics and forces: Experiment and continuum theory', *Phys. Rev. E* **65**, 011307.

Bocquet, L., Losert, W., Schalk, D., Lubensky, T. C. & Gollub, J. P. (2001*b*), 'Granular shear flow dynamics and forces: Experiment and continuum theory', *Phys. Rev. E* **65**, 011307.

Brey, J. J. & Dufty, J. W. (2005), 'Hydrodynamic modes for a granular gas from kinetic theory', *Phys. Rev. E* **72**(1), 011303.

Brey, J. J. & Ruiz-Montero, M. J. (2004), 'Simulation study of the green-kubo relations for dilute granular gases', *Phys. Rev. E* **70**(5), 051301.

Brey, J. J., Moreno, F. & Dufty, J. W. (1996), 'Model kinetic equation for low-density granular flow', *Phys. Rev. E* **54**(1), 445.

Brilliantov, N. V. & Poschel, T. (2006), 'Breakdown of the sonine expansion for the velocity distribution of granular gases', *Europhys. Lett.* **74**, 424.

Campbell, C. S. (1990), 'Rapid granular flows', *Annu. Rev. Fluid Mech* **22**, 57.

Carnahan, N. F. & Starling, K. E. (1969), 'Equation of state for nonattracting rigid spheres', *J. Chem. Phys.* **51**(2), 635–636.

Chaikin, P. M. (1995), *Principles of Condensed Matter Physics*, Cambridge University Press, U.K.

Chapman, S. & Cowling, T. G. (1952), *The mathematical theory of non-uniform gases*, Cambridge Mathematical Library, Cambridge University Press.

Chen, W., Hou, M., k. Lu, Jiang, Z. & Lam, L. (2001), 'Granular flows through vertical pipes controlled by an electric field', *Phys. Rev E* **64**, 061305.

Chladni, E. F. (1787), 'Entdeckungen uber die theorie des klanges'.

Choo, K., Molteno, T. & Morris, S. (1997), 'Traveling granular segregation patterns in a long drum mixer', *Phys. Rev. Lett.* **79**, 2975.

Collins, R. (1964), 'Statistics of a simplified two-dimensional bernal liquid', *Proc. Phys. Soc.* **83**, 553.

Coulomb, C. A. (1773), 'Memoires de mathematiques et de physique presentes a l'academie royal des sciences par divers sacans et lus dans les assemblees', *L'imprimerie Royale* p. 343.

Daerr, A., Lee, P., Lanuza, J. & Clment, . (2003), 'Erosion patterns in a sediment layer', *Phys. Rev E* **67**, 065201.

Daniels, K. E. & Behringer, R. P. (2005), 'Hysteresis and competition between disorder and crystallization in sheared and vibrated granular flow', *Phys. Rev. Lett.* **94**, 168001.

D'Anna, G. & Gremaud, G. (2001), 'The jamming route to the glass state in weakly perturbed granular media', *Nature (London)* **413**, 407.

deGennes, P. G. (1999), 'Granular matter: a tentative view', *Rev. Mod. Phys.* **71**, S374.

Douady, S., Fauve, S. & Laroche, C. (1989), 'Subharmonic instabilities and defects in a granular layer under vertical vibrations', *Europhys. Lett.* **8**, 621.

Drahun, J. A. & Bridgewater, J. (1983), 'The mechanics of free surface segregation', *Powder Technol.* **36**, 39–53.

Dufty, J. W. & Brey, J. J. (2003), 'Hydrodynamic modes for granular gases', *Phys. Rev. E* **68**(3), 030302(R).

Dufty, J. W., Baskaran, A. & Zogaib, L. (2004), 'Gaussian kinetic model for granular gases', *Phys. Rev. E* **69**(5), 051301.

Egolf, D. A. (2000), 'Equilibrium regained: From nonequilibrium chaos to statistical mechanics', *Science* **287**, 101.

Ennis, B. J., Green, J. & Davies, R. (1994), *Part. Technol* **90**, 32.

Faraday, M. (1831), 'On a peculiar class of acoustical figures; and on certain forms assumed by groups of particles upon vibrating elastic surfaces', *Phil. Trans. R. Soc.* **131**, 299.

Fiodor, S. & Ottino, J. (2003), 'Dynamics of axial segregation and coarsening of dry granular materials and slurries in circular and square tubes', *Phys. Rev. Lett.* **91**, 244301.

Forterre, Y. & Pouliquen, O. (2001), 'Longitudinal vortices in granular flows', *Phys. Rev. Lett.* **86**, 5886.

Forterre, Y. & Pouliquen, O. (2003), 'Long-surface-wave instability in dense granular flows', *J. Fluid Mech* **486**, 21–50.

Fraser, D. P., Zuckerman, M. J. & Mouritzen, O. G. (1990), 'Definition of voronoi cell', *Phys. Rev. E* **42**, 3186.

Garzó, V. & Dufty, J. (1999), 'Homogeneous cooling state for a granular mixture', *Phys. Rev. E* **60**(5), 5706.

Ginzburg, V. L. & Landau, L. D. (1950), 'Theory of granular gases: some recent results and some open problems', *Zh. Eksp. Teor. Fiz.* **20**, 1064.

Glaser, M. A. & Clark, N. A. (1990), 'Statistical geometry of simple liquids in two dimensions', *Phys. Rev. A* **41**, 4585.

Goldhirsch, I. (2003), 'Rapid granular flows', *Annu. Rev. Fluid Mech* **35**, 267–293.

Goldhirsch, I., Noskowicz1, S. H. & Bar-Lev, O. (2005), 'Theory of granular gases: some recent results and some open problems', *J. Phys.: Condens. Matter* **17**, S2591–S2608.

Goldshtein, A. & Shapiro, M. (1995), 'Mechanics of collisional motion of granular materials. Part 1. Gene ral hydrodynamic equations', *J. Fluid Mech.* **282**, 75–114.

Gracheva, M. E., Rickman, J. M. & Gunton, J. D. (2000), 'Coarse-grained ginzburg-glandau free energy for lennard-jones systems', *J. Chem. Phys.* **113**, 3525.

Gtzendorfer, A., Tai, C., Kruelle, C. A., Rehberg, I. & Hsiau, S. S. (2006), 'Fluidization of a vertically vibrated two-dimensional hard sphere packing: A granular meltdown', *Phys. Rev. E* **74**, 011304.

Hill, K. & Kakalios, J. (1994), 'Reversible axial segregation of binary mixtures of granular materials', *Phys. Rev. E* **49**, 3610.

Hill, K. & Kakalios, J. (1995), 'Reversible axial segregation of rotating granular media', *Phys. Rev. E* **52**, 4393.

Hoover, W. G. & Ree, F. H. (1968), 'Melting transition and communal entropy for hard spheres', *J. Chem. Phys.* **49**, 3609.

Iverson, R. M. (1997), 'The physics of debris flows', *Rev. Geophys.* **35**, 245–296.

Jackson, R. (1986), 'Some features of the flow of granular materials and aerated granular materials', *J. Rheol.* **30**, 907.

Jaeger, H. & Nagel, S. (1992), 'Physics of the granular state', *Science* **255**, 1523.

Jaeger, H. M., Shrinbot, T. & Umbanhowar, P. B. (2000), 'Does the granular matter?', *Proc. Natl. Acad. sci.USA* **97**, 12959.

Jaeger, H., Nagel, S. & Behringer, R. (1996), 'The physics of granular materials', *Physics Today* **74**, 32.

Jaster, A. (1999), 'Computer simulations of the two-dimensional melting transition using hard disks', *Phys. Rev. E* **59**, 2594.

Jaster, A. (2004), 'Hysteresis and competition between disorder and crystallization in sheared and vibrated granular flow', *Phys. Lett. A* **330**, 120.

Jenkins, J. & Richman, M. (1985), 'Kinetic theory for plane flows of a dense gas of identical, rough, inelastic, circular disks', *Phys. Fluids* **28**, 3485.

Jenkins, J. T. & Richman, M. W. (1984), 'Grad's 13-moment system for a dense gas of inelastic spheres', *Archive of Rational Mechanics and Analysis* **87**, 355–377.

Jenkins, J. T. & Richman, M. W. (1988), 'Plane simple shear of smooth inelastic circular disks: the anisotropy of the second moment in the dilute and dense limits', *J. Fluid Mech.* **192**, 313–328.

Jenkins, J. T. & Satake, M. (1983), *Mechanics of Granular Materials: New Models and Constitutive Relations*, Elsevier Science Publishers B.V.

Kadanoff, L. P. (1999), 'Built upon sand: Theoretical ideas inspired by granular flows', *Rev. Mod. Phys.* **71**, 435.

Kawamura, H. (1979), 'A simple thoery of hard disk transition', *Prog. Theor. Phys* **61**, 1584.

Kawamura, H. (1983), 'Statistics of two-dimensional amorphous lattice', *Prog. Theor. Phys* **70**, 352.

Khakhar, D., McCarthy, J. & Ottino, J. (1997), *Phys. Fluids* **9**, 3600.

Kumaran, V. (2005), 'Kinetic model for sheared granular flows in the high knudsen number limit', *Phys. Rev. Lett.* **95**(10), 108001.

Kurchan, J. (2000), 'Emergence of macroscopic temperatures in systems that are not thermodynamical microscopically: towards a thermodynamic description of slow granular rheology', *J. Phys. Condens. Matter* **12**, 6611.

Lindemann, F. A. (1910), *Phys. Z.* **11**, 609.

Losert, W., Bocquet, L., Lubensky, T. C. & Gollub, J. P. (2000), 'Particle dynamics in sheared granular matter', *Phys. Rev. Lett.* **85**, 1428.

Losert, W., Cooper, D. G. W. & Gollub, J. P. (1999), 'Propagating front in an excited granular layer', *Phys. Rev. E* **59**, 5855.

Lun, C. K. K. (1991), 'Kinetic theory for granular flow of dense, slightly inelastic, slightly rough spheres', *J. Fluid Mech.* **233**, 539–559.

Lun, C., Savage, S., Jeffery, D. & Chepurniy, N. (1983), 'Kinetic theories for granular flow: inelastic particles in couette flow and slightly inelastic particles in a general flow field', *J. Fluid. Mech.* **140**, 223.

Lutsko, J. F. (2006), 'Chapman-enskog expansion about nonequilibrium states with application to the sheared granular fluid', *Phys. Rev. E* **73**(2), 021302.

Makse, H. A., Havlin, S., King, P. R. & Stanley, H. E. (1997), 'Spontaneous stratification in granular mixtures', *Nature* **386**, 379.

Melo, F., Umbanhowar, P. B. & Swinney, H. L. (1994), 'Transition to parametric wave patterns in a vertically oscillated granular layer', *Phys. Rev. Lett.* **72**, 172.

Melo, F., Umbanhowar, P. B. & Swinney, H. L. (1995), 'Hexagons, kinks, and disorder in oscillated granular layers', *Phys. Rev. Lett.* **75**, 3838.

Merrow, E. W. (1985), 'Linking research and d to problems experienced in solids processing', *Chem. Eng. Prog.* **May**, 14.

Metcalfe, G., Shinbrot, T., McCarthy, J. & Ottino, J. (1995), *Nature (London)* **374**, 39.

Metcalfe, G., Tennakoon, S. K., Kondic, L., D.G.Schaeffer & Behringer, R. P. (2002), 'Granular friction, coulomb failure, and the fluid-solid transition for horizontally shaken granular materials', *Phys. Rev. E* **65**, 031302.

Mitus, A. C., Weber, H. & Marx, D. (1997), 'Local structure analysis of the hard-disk fluid near melting', *Phys. Rev. E* **55**, 6855.

Montanero, J. & Santos, A. (2000), 'Computer simulation of uniformly heated granular fluids', *Granular Matter* **2**(2), 53–64.

Moon, S. J., Shattuck, M. D. & Swift, J. B. (2001), 'Velocity distributions and correlations in homogeneously heated granular media', *Phys. Rev. E* **64**, 031303.

Moucka, F. & Nezbeda, I. (2005), 'Detection and characterization of structural changes in the hard-disk fluid under freezing and melting conditions', *Phys. Rev. Lett* **94**, 040601.

Mueth, D. M., Debregeas, G. F., Karczmar, G. S., Eng, P. J., Nagel, S. R. & Jaeger, H. M. (2000), 'Signatures of granular microstructure in dense shear flows', *Nature (London)* **406**, 385.

Nedderman, R. M. (1992), *Statics and Kinematics of Granular Materials*, Cambridge University Press, U.K.

Nelson, D. R. & Halperin, B. I. (1979), 'Dislocation-mediated melting in two dimensions', *Phys. Rev. B* **19**, 2457.

Ojha, R. P., Lemieux, P. A., Dixon, P. K., Liu, A. J. & Durian, D. J. (2004), 'Statistical mechanics of a gas-fluidized particle', *Nature* **427**, 521.

Okabe, A., Boots, B., Sugihara, K. & Chiu, S. N. (2000), *Spacial Tesselations: Concepts and Applications of Voronoi Diagrams*, Wiley, New York, USA.

Olafsen, J. S. & Urbach, J. S. (1998), 'Clustering, order, and collapse in a driven granular monolayer', *Phys. Rev. Lett.* **81**, 4369.

Olafsen, J. S. & Urbach, J. S. (1999), 'Clustering, order, and collapse in a driven granular monolayer', *Phys. Rev. E* **60**, R2468.

Olafsen, J. S. & Urbach, J. S. (2005), 'Two-dimensional melting far from equilibrium in a granular monolayer', *Phys. Rev. Lett.* **95**, 098002.

Ottino, J. & Khakhar, D. (2000), *Annu. Rev. Fluid Mech.* **32**, 55.

Pak, H. K. & Behringer, R. P. (1995), 'Effects of ambient gases on granular materials under vertical vibration', *Phys. Rev. Lett.* **74**, 4643.

Pöschel, T., Brilliantov, N. V. & Formella, A. (2006), 'Impact of high-energy tails on granular gas properties', *Phys. Rev. E* **74**, 041302.

Pouliquen, O., Delour, J. & Savage, S. B. (1997), 'Fingering in granular flows', *Nature (London)* **386**, 816.

Prevost, A., Egolf, D. A. & Urbach, J. S. (1996), 'Stress fluctuations for continuously sheared granular materials', *Phys. Rev. Lett.* **77**, 3110.

Prevost, A., Egolf, D. A. & Urbach, J. S. (2002), 'Forcing and velocity correlations in a vibrated granular monolayer', *Phys. Rev. Lett.* **89**, 084301.

Prevost, A., Melby, P., Egolf, D. A. & Urbach, J. S. (2004), 'Nonequilibrium two-phase coexistence in a confined granular layer', *Phys. Rev. E* **70**, 050301.

Rajchenbach, J. (1990), 'Flow in powders: From discrete avalanches to continuous regime', *Phys. Rev. Lett.* **65**, 2221.

Reis, P. M., Ingale, R. A. & Shattuck, M. D. (2006), 'Crystallization of a quasi-two-dimensional granular fluid', *Phys. Rev. Lett.* **96**, 258001.

Reis, P. M., Ingale, R. A. & Shattuck, M. D. (2007*a*), 'Caging dynamics in a granular fluid', *Phys. Rev. Lett.* **98**, 188301.

Reis, P. M., Ingale, R. A. & Shattuck, M. D. (2007*b*), 'Forcing independent velocity distributions in an experimental granular fluid', *Phys. Rev. E* **75**, 051311.

Reynolds, O. (1885), *Phil. Mag.* **20**, 469.

Rouyer, F. & Menon, N. (2000), 'Velocity fluctuations in a homogeneous 2d granular gas in steady state', *Phys. Rev. Lett.* **85**(17), 3676.

Rutgers, M. A., Dunsmuir, J. H., Xue, J. Z., Russel, W. B. & Chaikin, P. M. (1996), 'Measurement of the hard-sphere equation of state using screened charged polystyrene colloids', *Phys. Rev B* **53**, 5043.

Santos, A., Montanero, J. M., Dufty, J. W. & Brey, J. J. (1998), 'Kinetic model for the hard-sphere fluid and solid', *Phys. Rev. E* **57**(2), 1644.

Savage, S. (1979), 'Gravity flow of cohesionless granular materials in chutes and channels', *J. Fluid Mech* **92**, 53–96.

Savage, S. & Jeffery, D. (1981), 'The stress tensor in a granular flow at high shear rates', *J. Fluid Mech* **110**, 255.

Savage, S. B. & Lun, C. K. K. (1988), 'Particle size segregation in inclined chute flow of cohesionless granular slids', *J. Fluid Mech.* **189**, 311–335.

Schllmann, S. (1999), 'Simulation of a two-dimensional shear cell', *Phys. Rev. E* **59**, 889.

Sela, N., Goldhirsch, I. & Noskowicz, S. H. (1996), 'Kinetic theoretical study of a simply sheared two-dimensional granular gas to Burnett order', *Phys. Fluids* **8**(9), 2337–2353.

Sengupta, S., Nielaba, P. & Binder, K. (2000), 'Elastic moduli, dislocation core energy, and melting of hard disks in two dimensions', *Phys. Rev. E* **61**, 6294.

Shinbrot, T. & Muzzio, F. (2000), 'Nonequilibrium patterns in granular mixing and segregation', *Physics Today* **53**, 25.

Silbert, L. E., Ertas, D., Grest, G. S., Halsey, T. C., Levine, D. & Plimpton, S. J. (2001), 'Granular flow down an inclined plane: Bagnold scaling and rheology', *Phys. Rev E* **64**, 051302.

Tegzes, P., Vicsek, T. & Schiffer, P. (2002), 'Avalanche dynamics in wet granular materials', *Phys. Rev. Lett.* **89**, 094301.

Tegzes, P., Vicsek, T. & Schiffer, P. (2003), 'Development of correlations in the dynamics of wet granular avalanches', *Phys. Rev. E* **67**, 051303.

Thomas, B., Mason, M. O., Liu, Y. A. & Squires, A. M. (1989), 'Identifying states in shallow vibrated beds', *Powder Technol.* **57**, 267.

Umbanhowar, P. B., Melo, F. & Swinney, H. L. (1996), 'Localized excitations in a vertically vibrated granular layer', *Nature (London)* **382**, 793.

van Noije, T. & Ernst, M. (1998), 'Velocity distributions in homogeneous granular fluids: the free and heated case', *Granular Matter* **1**, 57–64.

van Noije, T., Ernst, M. & Brito, R. (1998), 'Ring kinetic theory for an idealized granular gas', *Physica A* **251**, 266.

van Noije, T. P. C., Ernst, M. H., Trizac, E. & Pagonabarraga, I. (1999), 'Randomly driven granular fluids: Large-scale structure', *Phys. Rev. E* **59**(4), 4326–4341.

van Zon, J. & MacKintosh, F. (2004), 'Velocity distributions in dissipative granular gases', *Phys. Rev. Lett.* **93**(3), 038001.

van Zon, J. S., Kreft, J., Goldman, D. I., Miracle, D., Swift, J. B. & Swinney, H. L. (2004), 'Crucial role of sidewalls in velocity distributions in quasi-two-dimensional granular gases', *Phys. Rev. E* **70**, 040301(R).

Watanabe, H., Yukawa, S., Ozeki, Y. & Ito, N. (2004), 'Elastic moduli, dislocation core energy, and melting of hard disks in two dimensions', *Phys. Rev. E* **69**, 045103(R).

Williams, D. R. M. & MacKintosh, F. C. (1996), 'Driven granular media in one dimension: Correlations and equation of state', *Phys. Rev. E* **54**, R9.